

1 **Physical and biological processes driving seasonal variability of Nitrate**
2 **budget and biological productivity in the Gabon-Congo upwelling system**

3 **Landry Junior Mbang Essome^{14,23}, Gaël Alory¹³, Casimir Yelognissé Da-**
4 **Allada^{21,34,5}, Isabelle Dadou¹³, Roy Dorgeless Ngakala^{31,42}, Guillaume**
5 **Morvan¹³**

6 ¹Université de Toulouse, LEGOS (CNES/CNRS/IRD/UT), Toulouse, France ~~Department of~~
7 ~~Oceanography and Applications, International Chair in Mathematical Physics and Applications,~~
8 ~~University of Abomey-Calavi, Cotonou, Benin.~~

9 ²Laboratoire de Géosciences, de l'Environnement et Applications, Université Nationale des
10 Sciences Technologies, Ingénierie et Mathématiques, Abomey, Benin. ~~Department of~~
11 ~~Oceanography and Environment, Institut National de Recherche en Sciences Exactes et~~
12 ~~Naturelles, Pointe-Noire, Congo.~~

13 ³ Department of Oceanography and Applications, International Chair in Mathematical Physics
14 and Applications, University of Abomey-Calavi, Cotonou, Benin. ~~Université de Toulouse,~~
15 ~~LEGOS (CNES/CNRS/IRD/UT), Toulouse, France.~~

16 ⁴ Department of Oceanography and Environment, Institut National de Recherche en Sciences
17 Exactes et Naturelles, Pointe-Noire, Congo. ~~Laboratoire de Géosciences, de l'Environnement et~~
18 ~~Applications, Université Nationale des Sciences Technologies, Ingénierie et Mathématiques,~~
19 ~~Abomey, Benin.~~

20 ⁵**Laboratoire d'Hydrologie Marine et Côtière, Institut de Recherches Halieutiques et**
21 **Océanologiques du Bénin, Cotonou, Bénin.**

22 **Corresponding author : L.J. Mbang Essome (landrymbangessome@gmail.com)**

23
24
25
26
27
28
29
30
31
32

33 |

34 |

35 |

36 |

37 |

38 |

39 |

40 |

41 |

42 |

43 |

44 |

45 |

46 |

47 |

48 |

49 |

50 | **Acronyms:**

51 | **CTW: Coastally trapped waves**

52 | **CoUS: Congolese Upwelling System**

53 | **EKW: Equatorial Kelvin Waves**

54 | **GG: Gulf of Guinea**

55 | **MLD: Mixed Layer Depth**

56 | **SST: Sea Surface Temperature**

57 | **SLA: Sea Level Anomaly**

58 | **CHLa: Chlorophyll-a**

59 | **EBUS: Eastern Boundary Upwelling System**

60 | **TAUS: Tropical Angolan Upwelling System**

61 |

62 |

63 |

64 |

65 |

66 |

67 |
68 |
69 |
70 |
71 |
72 |
73 |
74 |
75 |
76 |
77 |
78 |
79 |
80 |
81 |
82 |
83 |
84 |
85 |
86 |
87 |
88 |
89 |
90 |

91 | **Abstract**

92 | **The Congolese upwelling system, located in the southeastern Gulf of Guinea, is a highly productive**
93 | **marine ecosystem influenced by both local and remote physical forcing. This study investigates the**
94 | **seasonal variability of the nitrate budget and biological productivity in this region using a high-**
95 | **resolution (1/36°) coupled physical-biogeochemical simulation with the NEMO-PISCES model.**
96 | **The analysis highlights the relative contributions of physical and biological processes in**
97 | **modulating nitrate concentrations in both the mixed layer and the euphotic zone. Results reveal a**
98 | **semi-annual cycle of nitrate, with two upwelling periods (May–August and December) and two**
99 | **downwelling periods (January–April and October–November). These cycles are primarily driven**

100 | **by the passage of coastal trapped waves (CTWs) forced by equatorial Kelvin waves, inducing**
101 | **vertical thermocline displacements and regulating nitrate availability in the euphotic zone.**

102 | **The nitrate budget analysis shows that the vertical diffusion linked to internal tide and local wind**
103 | **advection, and vertical advection linked to the coastal trapped waves (CTWs), areis the dominant**
104 | **process supplying nitrate to the mixed layer during the main upwelling season. However, near the**
105 | **Congo River mouth (5.5°S–6°S), the horizontal advection plays a key role, supplying significant**
106 | **amounts of nitrate through the river plume. In the lower euphotic layer, the vertical mixing**
107 | **contributes to the nitrate loss during the upwelling but becomes a source of nitrate during the**
108 | **downwelling periods. The seasonal cycle of the chlorophyll-a (CHLa) concentration follows that of**
109 | **nitrate, confirming that the primary production in this region is mainly driven by nitrate**
110 | **availability. The study also highlights the role of the Angola Current in transporting low-nitrate**
111 | **waters from the Equatorial Undercurrent, which influences the nitrate and CHLa balance in the**
112 | **Congolese upwelling system.**

113 | **These findings provide new insights into the mechanisms governing nutrient dynamics and**
114 | **biological productivity in the Congolese upwelling system. Understanding these processes is**
115 | **crucial for assessing the impact of climate variability on the regional marine ecosystems and**
116 | **fisheries.**

117 | **Keywords: Nitrate Budget, Congolese Upwelling System, NEMO-PISCES Model,**
118 | **Physical-Biogeochemical Interactions, Seasonal Variability, Coastal Trapped Waves**

119 |

120 |

121 |

122 |

123 |

124 |

125 |

126 |

127 |

128 |

129 |

130 |

131 |

132 |

133 |

134

135

136 | 1 Introduction

137 | **The Eastern Boundary Upwelling Systems (EBUS) are the most productive areas in the global**
138 | **ocean in terms of biological resources, hosting almost 20% of the world's fisheries (Chavez and**
139 | Messie, 2009, 2015), even though they only represent around 1% of the world's ocean surface (Freon et
140 | al., 2009). They are therefore an important economic support for the countries bordering these areas
141 | (Carr et al., 2002). EBUS are controlled by wind stress blowing parallel to the coast, generating an
142 | offshore Ekman transport leading to coastal upwelling of cold and nutrient-rich waters, which trigger
143 | primary production in the euphotic layer, with increased surface chlorophyll-a (CHLa) concentration
144 | visible on satellite images (e.g. Gutknecht et al., 2013). Besides their ecological richness, EBUS act as
145 | active interfaces for greenhouse gases. They are recognized as significant sources of N₂O, primarily due
146 | to the oxygen minimum zone (OMZ) that favors subsurface production (Gutknecht et al., 2013;
147 | Resplandy et al., 2024). Regarding CO₂, while cold surface waters enhance gas solubility, the vigorous
148 | upwelling of deep waters rich in Dissolved Inorganic Carbon (DIC) generally dominates this thermal
149 | effect, driving net CO₂ outgassing near the coast (Resplandy et al., 2024).

150 | Beyond these EBUS, recent studies (Bachèlery et al., 2016; Kopte et al., 2017; Awo et al., 2022) **have**
151 | **shown** that the variability of **Sea Surface Temperature (SST, a key upwelling indicator)** at the eastern
152 | boundary of the **South** Atlantic **was** not only impacted by local wind forcing, but also by remote forcing
153 | initiated by the equatorial dynamics. Indeed, the equatorial Kelvin waves (EKW) propagating along the
154 | equator and later poleward along the coast as coastal trapped waves (CTW) **have been shown to lead to**
155 | the establishment of seasonal upwelling systems.

156 | This **is** the case for the Congolese and Angolan tropical upwelling systems, located in the south-east of
157 | the Gulf of Guinea (GG), which are highly productive marine ecosystems (Ostrowski et al., 2009).
158 | Fishing provides around 25% of the Angolan population's total animal protein intake and is essential for
159 | economic security (Hutchings et al., 2009; Sowman and Cardoso, 2010; FAO, 2022). The seasonal
160 | variability of SST along the Angolan **coast has shown** an evolution that **was** similar to that observed in
161 | the Congo (Bachèlery et al., 2015, 2016; Kopte et al., 2017; Awo et al., 2022; Brandt et al., 2023). It **was**
162 | characterized by a semi-annual pattern with an initial warming in February-April followed by a first
163 | upwelling-induced cooling in May-August. Then there **was** a second warming, less significant than the
164 | first, in September-November, followed by a second, less significant cooling in December-January.
165 | Following to Radenac et al. (2020) and Brandt et al. (2023), in the tropical Atlantic ocean, the
166 | thermocline and nitracline **were** often found at the same depth, which **meant** that an upward movement
167 | of the thermocline **was** associated with upward advection of nitrate, fueling biological productivity.
168 | Brandt et al. (2023) also **pointed** out that in the Angolan tropical upwelling system, the seasonal cycle of
169 | nitrate **was** in phase with that of CHLa derived from ocean color satellites (Fig. 1). Given that the wind
170 | stress along the coast **was** low for most of the year and out of phase with the upwelling period, the
171 | upwelling **was rather shown to be** induced by the passage of waves trapped at the coast, **which**

172 | signature **was** visible on the seasonal cycle of the sea level anomaly (Bachelery et al., 2016; Awo et al.,
173 | 2022; Brandt et al., 2023).

174 | The cross-shore extension of the zone covered by upwelling **was** modulated by the zone's ocean
175 | circulation (Fig. 1), dominated by the southward coastal Angola Current and Congo-Gabonese
176 | Undercurrent (Kopte et al., 2017; Bachelery et al., 2016; Awo et al., 2022). Bachelery et al. (2016), based
177 | on a coupled physical-biogeochemical model, **showed** that equatorial remote forcing **was** dominant for
178 | the interannual variability of nutrients and primary production, whereas the local wind stress forcing **was**
179 | dominant for the sub-seasonal variability. Some studies also **highlighted** the important role played by
180 | turbulent mixing, locally enhanced in shallow waters near the coast (Körner et al., 2023, 2024;
181 | Tchupalanga et al., 2018a; Rouault, 2012), in the seasonal modulation of SST and nutrients in Angolan
182 | coastal waters.

183 | The Gabon-Congo upwelling zone (from 0°N to 6°S) is poorly documented. In a recent study using a
184 | high resolution (1/36°) simulation of the NEMO model over the GG, Ngakala et al. (2025) **assessed** the
185 | seasonal mixed layer heat budget in the Congolese upwelling system. They **found** that the mixed layer
186 | heat budget in the Congolese coastal area **was** driven by two major processes: warming by heat fluxes,
187 | dominated all year long by the solar flux, and cooling by vertical mixing at the base of the mixed layer.
188 | **The** total advection contribution **was** less important and **played** a secondary role in the mixed layer heat
189 | budget. They **also mentioned** that the relative contribution of vertical advection and diffusion in the
190 | mixed layer heat budget **was** sensitive to the criterion used to define the mixed layer.

191 | These results **were** in agreement with the conclusion of Körner (2023) in the northern Angolan
192 | upwelling south of the Congo River mouth. This **latter** study **found** that the net surface heat flux
193 | **warmed** the coastal water further, whereas turbulent mixing across the base of the mixed layer **was** an
194 | important cooling term. Also, Scannell and McPhaden (2018), using data from a PIRATA mooring
195 | located off the Congo River at [8°E; 6°S], **found** that the seasonal evolution of mixed layer properties
196 | **had** two main phases: a warm fresh phase (December-April) when solar heating **was** very efficient in
197 | warming SST in a thin mixed layer, and a cold-salty phase (May-September) driven by the
198 | intensification of southeasterly trades in response to the onset of the West African Monsoon and
199 | northward displacement of the ITCZ. They also **pointed** out the necessity to take into account
200 | precipitation influence in the mixed layer heat budget.

201 | Little information **has been** available at the seasonal scale for biogeochemistry in the GG. In the
202 | equatorial upwelling system, the respective contributions of physical and biological processes on the
203 | seasonality of nitrate and biological productivity, in the mixed layer and euphotic layer, **have been**
204 | quantified by Radenac et al. (2020). Along the coast, most studies of biogeochemical dynamics **have**
205 | **been** either limited to the section between 6°S and the Angola Benguela frontal zone (Brandt et al.,

206 2023), or **have focused** on the interannual variability of biogeochemical tracers (Bachelery et al., 2016).
207 The seasonal variability of biogeochemical tracers and biological productivity between 0°N and 6°S is
208 likely influenced by three major processes: coastal upwelling, input of nutrients by the Congo River
209 discharge (which is the second largest river discharge in the world; Hopkins et al., 2013), and the
210 stratification linked to the Congo River freshwater. The aim of this paper **is to** investigate the respective
211 roles of physical and biological processes in the seasonal cycle of nitrate and CHLa concentration, and
212 the respective contributions of coastal upwelling and Congo River discharge to the biological
213 productivity in the Congolese upwelling system. **The paper is organized as follows: Section 2**
214 **describes the numerical model and datasets; Section 3 presents the model validation and the**
215 **nitrate budget analysis; Section 4 discusses the physical-biological interactions, and Section 5**
216 **provides the conclusions.**

217 ~~The Eastern Boundary Upwelling Systems (EBUS) are the most productive areas in the global ocean in~~
218 ~~terms of biological resources, hosting almost 20% of the world's fisheries (Chavez and Messie, 2009,~~
219 ~~2014), even though they only represent around 1% of the world's ocean surface (Freon et al., 2009). They~~
220 ~~are therefore an important economic support for the countries bordering these areas. EBUS are~~
221 ~~controlled by wind stress blowing parallel to the coast, generating an offshore Ekman transport leading~~
222 ~~to coastal upwelling of cold and nutrient-rich waters, which trigger primary production in the euphotic~~
223 ~~layer, with increased surface chlorophyll-a (CHLa) concentration visible on satellite images (e.g.~~
224 ~~Gutknecht et al., 2013). Besides their ecological richness, EBUS have been recognized as significant~~
225 ~~sources of greenhouse gases (CO₂, N₂O, CH₄), due to the oxygen minimum zone developed in such~~
226 ~~productive areas (Gutknecht et al., 2013; Bachelery et al., 2016), which are key drivers of climate~~
227 ~~variability, hence studying these areas is a priority for climate evolution.~~

228 ~~A part from these EBUS, recent studies (Bachelery et al., 2016, Kopte et al., 2017, Awo et al., 2022)~~
229 ~~have shown that the variability of SST (Sea Surface Temperature, a key upwelling indicator) at the~~
230 ~~eastern boundary of the Atlantic is not only impacted by local wind forcing, but also by remote forcing~~
231 ~~initiated by the equatorial dynamics. Indeed, the equatorial Kelvin waves (EKW) propagating along the~~
232 ~~equator and later poleward along the coast as coastal trapped waves (CTW), can lead to the establishment~~
233 ~~of seasonal upwelling systems.~~

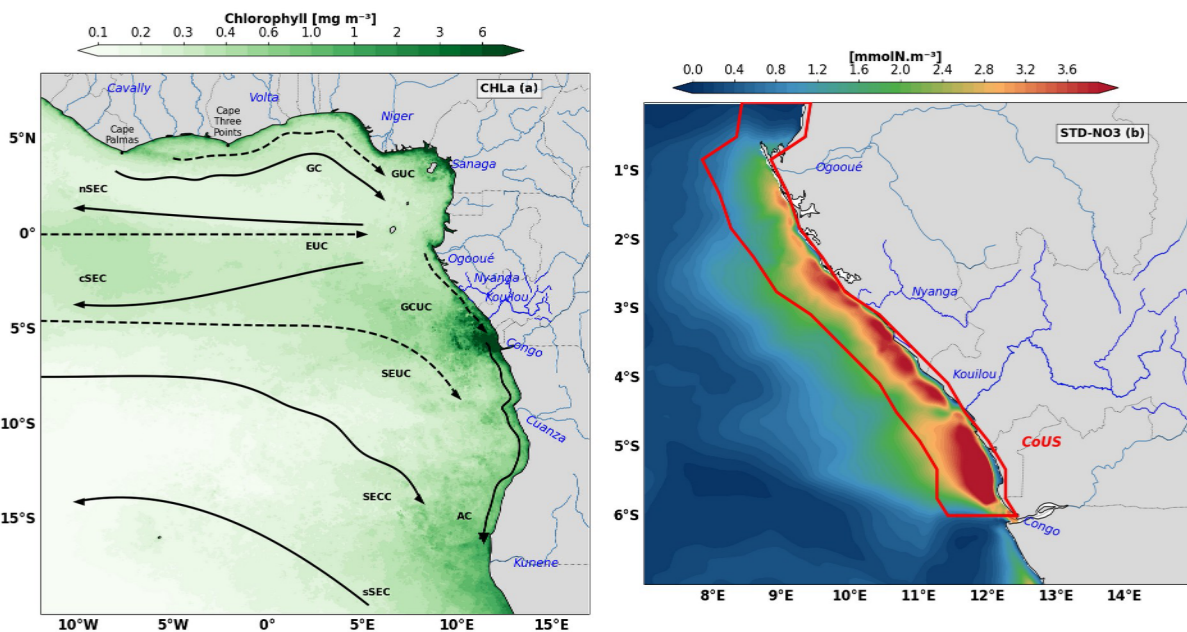
234 **This is the case for the Congolese and Angolan tropical upwelling systems, located in the south-east**
235 **of the Gulf of Guinea (GG), which are highly productive marine ecosystems (Ostrowski et al.,**
236 **2009). Fishing provides around 25% of the Angolan population's total animal protein intake and is**
237 **essential for economic security (Hutchings et al., 2009; Sowman and Cardoso, 2010; FAO, 2022).**
238 **The seasonal variability of SST along the Angolan coasts shows an evolution that is similar to that**
239 **observed in the Congo (Bachelery et al., 2015, 2016; Kopte et al., 2017; Awo et al., 2022; Brandt et**
240 **al., 2023). It is characterized by a semi-annual pattern with an initial warming in February-April**

241 followed by a first upwelling-induced cooling in May–August. Then there is a second warming, less
242 significant than the first, in September–November, followed by a second, less significant cooling in
243 December–January. According to Radenac et al. (2020) and Brandt et al. (2023), in the tropical
244 Atlantic ocean, the thermocline and nitracline are often found at the same depth, which means that an
245 upward movement of the thermocline is associated with upward advection of nitrate, fueling biological
246 productivity. Brandt et al. (2023) also points out that in the Angolan tropical upwelling system, the
247 seasonal cycle of nitrate is in phase with that of CHL_a derived from ocean color satellites (Fig.1). Given
248 that the wind stress along the coast is low for most of the year and out of phase with the upwelling period,
249 the upwelling would rather be induced by the passage of waves trapped at the coast, twhich signature is
250 visible on the seasonal cycle of the sea level anomaly (Bachelery et al., 2016; Awo et al., 2022; Brandt et
251 al., 2023). The cross-shore extension of the zone covered by upwelling is modulated by the zone's ocean
252 circulation (Fig.1), dominated by the southward coastal Angola Current and Congo–Gabonese
253 Undercurrent (Kopte et al., 2017; Bachelery et al., 2016, Awo et al., 2022). Bachelery et al. (2016), based
254 on a coupled physical–biogeochemical model, shows that equatorial remote forcing is dominant for the
255 interannual variability of nutrients and primary production, whereas the local wind stress forcing is
256 dominant for the sub-seasonal variability. Some studies also highlight the important role played by
257 turbulent mixing, locally enhanced in shallow waters near the coast (Körner et al., 2023; 2024;
258 Tchupalanga et al., 2018a; Rouault., 2012), in the seasonal modulation of SST and nutrients in Angolan
259 coastal waters.

260 The Gabon–Congo upwelling zone (from 0°N to 6°S) is poorly documented. In a recent study, using a
261 high-resolution (1/36°) simulation of NEMO model over the GG, Ngakala et al. (2025) assess the
262 seasonal mixed layer heat budget in the Congolese upwelling system. They found that the mixed layer
263 heat budget in the Congolese coastal area was driven by two major processes, warming by the heat
264 fluxes, dominated all year long by the solar flux, and cooling by the vertical mixing at the base of
265 the mixed layer. Whereas the total advection contribution is less important and plays a secondary
266 role in the mixed layer heat budget. They have also mentioned that the relative contribution of
267 vertical advection and diffusion in the mixed layer heat budget is sensitive to the criterion used to
268 define the mixed layer. These results are in agreement with the conclusion of Körner (2023) in the
269 northern Angolan upwelling south of the Congo river mouth. This later study found that the net
270 surface heat flux warms the coastal water further, whereas turbulent mixing across the base of the
271 mixed layer is an important cooling term. Also Scannell and McPhaden (2018), using data from a
272 PIRATA mooring located off the Congo River at [8°E; 6°S], found that the seasonal evolution of
273 mixed layer properties has two main phases: a warm-fresh phase (December–April) when solar
274 heating is very efficient in warming SST in a thin mixed layer. A cold-salty phase (May–
275 September) driven by intensification of southeasterly trades in response to the onset of the west

276 african Monsoon and northward displacement of ITCZ. They also point out the necessity to take
277 into account precipitation influence in the mixed layer heat budget.

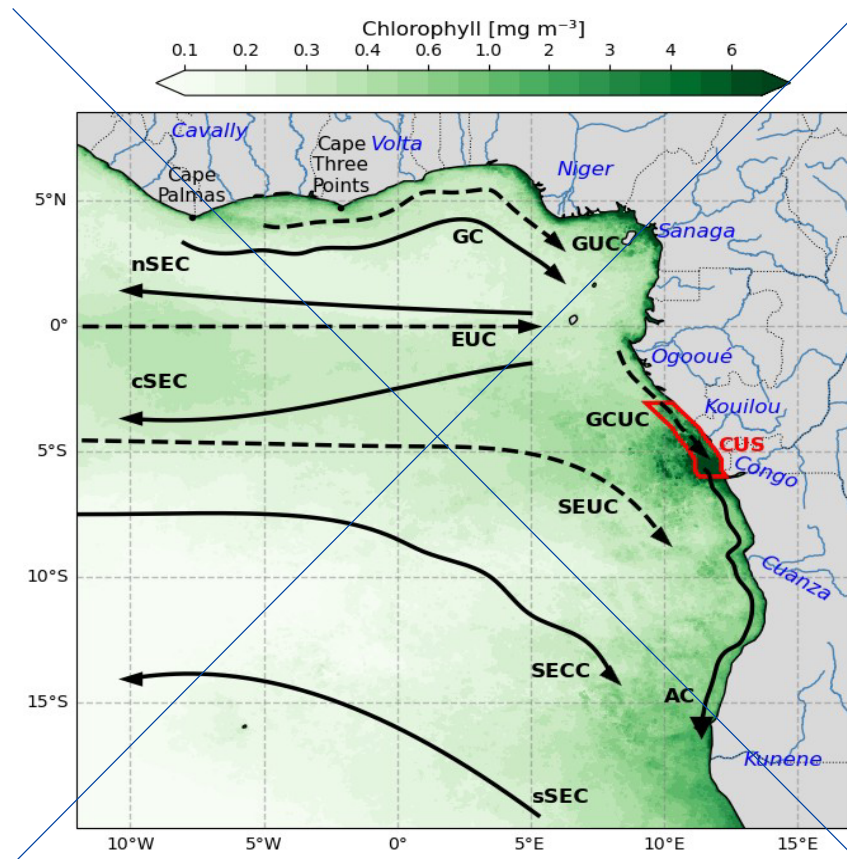
278 ~~Little information is available at seasonal scale for biogeochemistry in the GG. In the equatorial~~
279 ~~upwelling system, the respective contributions of physical and biological processes on the~~
280 ~~seasonality of nitrate and biological productivity, in the mixed layer and euphotic layer, have been~~
281 ~~quantified by Radenac et al (2020). Along the coast, most studies of biogeochemical dynamics are~~
282 ~~either limited to the section between 6°S and the Angola Benguela frontal zone (Brandt et al, 2023), or~~
283 ~~focus on the interannual variability of biogeochemical tracers (Bachelery et al, 2016). The seasonal~~
284 ~~variability of biogeochemical tracers and biological productivity between 0°N and 6°S is likely~~
285 ~~influenced by three major processes: coastal upwelling, input of nutrients by the Congo River discharge~~
286 ~~which is the second largest river discharge in the world (Hopkins et al, 2013), and the stratification linked~~
287 ~~to the Congo River freshwater. The aim of this paper is to highlight the respective roles of physical~~
288 ~~and biological processes in the seasonal cycle of nitrate and CHLa concentration and the~~
289 ~~respective contributions of coastal upwelling and Congo River discharge to the biological~~
290 ~~productivity in the Congolese upwelling system.~~



291
292 **Figure 1:** Regional ocean circulation and spatial distribution of biological and nutrient tracers.
293 (a) Annual mean surface Chlorophyll-a concentration (CHLa, $[\text{mg m}^{-3}]$). The map illustrates the spatial
294 distribution of biological productivity across the Gulf of Guinea and the South Atlantic African margin. Black
295 arrows and dashed lines indicate the major surface and subsurface currents: North South Equatorial Current
296 (nSEC), Central South Equatorial Current (cSEC), South South Equatorial Current (sSEC), Equatorial
297 Undercurrent (EUC), Guinea Current (GC), Guinea Undercurrent (GUC), Gabon-Congo Undercurrent (GCUC),
298 South Equatorial Undercurrent (SEUC), South Equatorial Counter Current (SECC), and Angola Current (AC). (b)
299 Standard deviation of Nitrate concentration (**STD-NO3**, $[\text{mmolN m}^{-3}]$). The color scale represents the variability
300 of nitrates in the upper ocean. The red polygon delimits the coastal domain defined as the Congolese Upwelling

301 | [System \(CoUS\), extending from the Congo River mouth \(~6°S\) to Cape Lopez \(~1°S\), which serves as the primary](#)
302 | [study area for the nutrient budget analysis. Blue labels highlight the discharge points of the Ogooué, Nyanga,](#)
303 | [Kouilou, and Congo rivers.](#)

304 |



305 |
306 | **Figure 1:** Average CHLa concentration in Gulf of Guinea with superimposed circulation pattern. The surface
307 | current (solid arrows) and thermocline current (dashed arrows) branches shown are the the Guinea Undercurrent
308 | (GUC); the Guinea Current (GC); the Equatorial Undercurrent (EUC); the northern, central and southern
309 | branches of the South Equatorial Current (nSEC, cSEC and sSEC); the South Equatorial Counter Current (SEUC); the South
310 | Equatorial Counter Current (SECC); the Gabon-Congo Undersea Current (GCUC) and the Angola Current (AC).
311 | Also shown are Niger, Congo, Kouilou, Sanaga, Cavally, Volta, Ogooué, Cuanza and Kunene rivers. The red box
312 | indicate the coastal extent of the Congolese Upwelling System (CUS; 3–6° S, 1° wide coastal strip). CHLa
313 | concentrations data are derived from the CCI product for 2011.

314 | 2 Data and methods

315 | 2.1 Numerical model

316 | To understand the dynamics in the Congolese upwelling system, we have used the NEMO (Nucleus
317 | for European Modelling of the Ocean) ocean general circulation model based on the primitive
318 | equations discretized on an Arakawa-C grid (Madec et al., 2024). The vertical mixing is computed
319 | from a turbulent closure scheme using the GLS (Generic Length Scale) formulation.

320 **In this work, the NEMO model was coupled with PISCES (Pelagic Interactions Scheme for**
321 **Carbon and Ecosystem Studies), a biogeochemical model developed by Aumont et al. (1998+998)**
322 **and subsequently improved. Here, the version used is PISCES-2 (Aumont et al., 2015). This model**
323 **has three main compartments: the first represents nutrients, including nitrogen compounds**
324 **(nitrate and ammonium), iron, phosphate and silicates; the second represents phytoplankton and**
325 **includes two classes, nano-phytoplankton and diatoms; the third compartment represents**
326 **zooplankton, made up of two classes, microzooplankton and meso-zooplankton. We used the**
327 **PISCES (cell quotas) model with constant Redfield ratios (Aumont and Bopp, 2006; Aumont et al.,**
328 **[2015](#)Aumont et al., 2015).**

329 A regional configuration of the GG (11°S - 6°N; 10°W - 14°E) with an horizontal resolution of
330 1/36° and 50 vertical levels is used. The atmospheric forcing is derived from the JRA-55 reanalysis of
331 the Japanese meteorological agency (Kobayashi et al. 2015), except for the wind forcing is based on
332 daily ASCAT (Advanced SCATterometer) satellite data at 1/4° spatial resolution. Lateral boundaries
333 conditions are from Mercator GLORYS12V1 reanalysis data at 1/12° spatial resolution for physics and
334 NEMO-PISCES reanalysis at 1/4° of Radenac et al (2020) for biogeochemistry. Continental freshwater
335 inputs for this configuration are derived from the ISBA-CTRIP model, and in situ data from the
336 HYBAM network for the Congo River. The NEMO configuration, ran over the period 2007-2017 (after
337 a two-year spin-up), was validated by Ngakala et al. (2025) in our region of study. This simulation has
338 also been validated and used in the Northern Gulf of Guinea for the coastal upwelling in summer and its
339 interaction with mesoscale dynamics (Thiam et al., 2024). The reference simulation of the coupled
340 biogeochemical physical model (NEMO-PISCES) was produced over the period 2007-2011, with a
341 spin-up of 4 years for the biogeochemical part (2007-2010). We analysed monthly and daily outputs for
342 the year 2011 monthly and daily outputs.

343 **2.2 Satellite and in-situ data**

344 **Several observational products were used to assess the model's ability to reproduce the physical**
345 **and biogeochemical characteristics of the area for the year 2011. We used the MUR product**
346 **(Multi-scale Ultra-high Resolution; Chin et al., 2017) with 1/4° spatial resolution and daily**
347 **temporal resolution to assess the regional distribution and the seasonal cycle of SST. The vertical**
348 **temperature distribution was assessed using the World Ocean Atlas (WOA; Locarnini et al., 2018;**
349 **Zweng et al., 2019) climatology. The CHLa data used came from the Globcolour product**
350 **(https://www.globecolour.info/CDR_Docs/GlobCOLOUR_PUG.pdf)—distributed by Copernicus**
351 **Marine Environment Monitoring Service (<http://marine.copernicus.eu/>), which combines data**
352 **from four ocean color satellites, with very high spatial resolution (1 km) and daily temporal**
353 **resolution.**

354 The nutrient fields were assessed using the CSIRO Atlas of Regional Seas climatology
 355 (~~Dunn~~Ridgway and ~~Dunn~~Ridgway, 2002) which merges several in situ databases (Argo buoys,
 356 WOD2005, WOCE3, Global Hydrographic Program, CTD and CMAR4 hydrology archives,
 357 NIWA5 hydrographic data, and CRC6 hydrographic data). It provides physical variables
 358 (Temperature, Salinity) and biogeochemical variables (NO₃, PO₄, O₂, Si) both at the surface and at
 359 depth with a horizontal resolution of 1/2 °, 79 vertical levels from the surface to 5500 m depth, with
 360 a step of 5 m near the surface then increasing with depth, and a daily temporal resolution. This
 361 product was built from 2009 and contains data from 1940 until 2011 which was the date when the
 362 last revision of the product was made. Near surface currents from the Ocean Surface Current
 363 Analysis Real-time (OSCAR, Johnson et al. 2007) dataset are based on satellite and in situ
 364 measurements of sea surface height, surface vector wind and SST. Dataset They are derived from
 365 quasi-linear and steady flow momentum equations thus combine geostrophic, Ekman and
 366 Stommel shear dynamics. Based on satellite and in situ measurements of sea surface height,
 367 surface vector wind and SST. OSCAR product is available on a 1/3°×1/3° grid with a 5-day
 368 ~~temporal resolution~~ temporal resolution of 5 days for year 2011, and we use it to validate the near
 369 surface currents (first 30 meters) of the model outputs. Sea Level Anomaly (SLA) was computed
 370 from the salto/duacs gridded product of Absolute Dynamic Topography for 2011. This product is
 371 based on sea surface height measurement of multimission altimeters since 1992, optimally
 372 interpolated onto 0.25° x 0.25° longitude/latitude grid (Ducet et al., 2000).

373 2.3 Methods

374 The variability of nutrients and in particular nitrate is driven by several physical and
 375 biogeochemical processes taken into account in our model. As in Radenac et al (2020), the nitrate
 376 budget integrated over the mixed layer depth is represented by the following equation:

$$\begin{aligned}
 377 \quad \frac{\partial \langle NO_3 \rangle}{\partial t} = & - \langle u \frac{\partial NO_3}{\partial x} \rangle - \langle v \frac{\partial NO_3}{\partial y} \rangle - \langle w \frac{\partial NO_3}{\partial z} \rangle + \frac{1}{h} \left(K_z \frac{\partial NO_3}{\partial z} \right)_{z=-h} - \frac{1}{h} \frac{\partial h}{\partial t} (\langle NO_3 \rangle - NO_{3z=-h}) \\
 378 \quad & + SMS(NO_3) \quad (1)
 \end{aligned}$$

379 In Equation (1), the term on the left represents the total nitrate tendency, where the brackets {...} denote
 380 the vertical average within the mixed layer of depth h. This depth h is defined as the level where the
 381 potential density exceeds the reference density at 3 meters by approximately 0.06 kg/m³ (Aroucha et
 382 al., 2025). On the right side of the equation, the first three terms represent the zonal, meridional, and
 383 vertical advectons of nitrate, respectively, with **u**, **v** and w being the components of the velocity field.
 384 The fourth term represents the vertical diffusion (mixing) at the base of the mixed layer (z=-h), where **Kz**
 385 is the vertical diffusion coefficient that varies in space and time. The fifth term corresponds to the
 386 entrainment term, which represents the flux of nitrate into the mixed layer during its deepening.
 387 However, it is not explicitly shown in our budget analysis. Following Radenac et al. (2020) for the

388 tropical Atlantic using a similar NEMO-PISCES configuration, this term is negligible compared to other
 389 term in the budget. Finally, the SMS (Source Minus Sink) term represents the contribution of biological
 390 processes to the spatial and temporal variability of NO₃ concentrations, as detailed in the following
 391 expression**In this equation, the term on the left is the total nitrate tendency, where $\langle \rangle$ represents**
 392 **the vertical average in the mixed layer of depth h , which is defined as the depth where the potential**
 393 **density exceeds the reference density, taken at 10 meters, by 0.03 kg/m³ (de Boyer-Montégut et al.,**
 394 **2004). On the right of the equation, the first 3 terms are respectively the zonal, meridional and**
 395 **vertical advectations of the nitrate, with u , v , and w the zonal, meridional and vertical components of**
 396 **the velocity field. The 4th term is lateral diffusion. The 5th term is the vertical diffusion, where K_z is**
 397 **the vertical diffusion coefficient that varies in space and time in the simulation. The 6th term**
 398 **corresponds to the entrainment at the base of the mixed layer. Adding to these physical processes, the**
 399 **SMS term (last term on the right of the equation 1) is the source minus sink term, which takes into**
 400 **account the influence of biological processes on the spatial and temporal variability of NO₃**
 401 **concentrations. It is made up of several processes and is represented by the expression:**

402
$$SMS(NO_3) = \text{Nitrif} - \mu_{NO_3}^P * P - \mu_{NO_3}^D * D - R_{NH_4} * \lambda_{NH_4} * \Delta(O_2) * NH_4 - R_{NO_3} * \text{Denit} \quad (2)$$

403 **where Nitrif corresponds to nitrification, which is the conversion of ammonium into nitrate by**
 404 **bacterial activity. It is parameterized by:**

405
$$\text{Nitrif} = \lambda_{NH_4} * \frac{NH_4}{1 + \langle PAR \rangle} * (1 - (O_2)) \quad (3)$$

406 **where NH₄ is the ammonium concentration, $\langle PAR \rangle$ is the average fraction of solar radiation**
 407 **available for photosynthesis, λ_{NH_4} is the nitrification rate and (O_2) is the oxygen variation in the**
 408 **mixed layer, which provides information on the oxic and anoxic conditions of the water column :**
 409 The second and third terms on the right of equation (2) are the growth of nanophytoplankton and
 410 diatoms, where μ_{NPK} and μ_{D} are their growth rates, P and D are their concentrations respectively.
 411 λ_{NPK} and λ_{D} are the stoichiometric N/C ratios of ammonification and nitrification respectively.
 412 The second and third terms on the right of equation (2) are the growth of nanophytoplankton and diatoms,
 413 where $\mu_{NO_3}^P$ and $\mu_{NO_3}^D$ are their growth rates, P and D are their concentrations respectively. R_{NH_4} and
 414 R_{NO_3} are the stoichiometric N/C ratios of ammonification and nitrification respectively. Denit
 415 **represents denitrification which occurs when the water becomes anoxic, and so nitrate (instead of**
 416 **oxygen) is consumed by remineralization of organic matter. A detailed description of the terms of**
 417 **these equations is given by Aumont et al (2015). We used the parameter PISCES values modified**
 418 **for the Tropical Atlantic ocean from Radenac et al. (2020). The balance terms in equation (1) have**
 419 **been calculated online for 2011. As the lateral diffusion term is generally negligible compared with**
 420 **the others, it will not be discussed further.**

421 Since the advection in (1) depends on both nitrate gradients and velocities, we investigate which
 422 component primarily controls its contribution. First, we analyze the seasonal evolution of gradient
 423 and velocity following Awo et al. (2022). Second, we evaluate the individual contributions of
 424 seasonal variations in velocity and gradient, as well as their combined effect, following Topé et al.
 425 (2023), according to equation (4).

$$426 \left(\overline{v \frac{\partial N}{\partial x}} \right) - \overline{v} \overline{\frac{\partial N}{\partial x}} - \overline{v' \frac{\partial N'}{\partial x}} \quad (4)$$

427 The total seasonal variation of the advection term is thus decomposed into three distinct contributions:

428 $\overline{v' \frac{\partial N'}{\partial x}}$ (Current variability), this term quantifies the impact of current velocity anomalies acting upon
 429 a mean (steady-state) nitrate distribution. It isolates the effect of current acceleration or intensification
 430 (such as the SEUC or the Angola Current) on nutrient transport. $\overline{v} \overline{\frac{\partial N}{\partial x}}$ (Gradient variability), this
 431 term represents the impact of seasonal changes in the nitrate concentration gradient under a mean
 432 circulation. It highlights the influence of seasonal water mass enrichment, particularly via the Congo
 433 River plume. $\overline{v \frac{\partial N}{\partial x}} - \overline{v} \overline{\frac{\partial N}{\partial x}}$ (Non-linear term), this term accounts for the simultaneous interaction between
 434 current fluctuations and gradient fluctuations. **To determine which of these mechanisms**
 435 **predominantly governs the nitrate budget,** Pearson correlation coefficients were calculated between
 436 **the total advective anomaly and each decomposed component.** **This statistical approach serves a**
 437 **critical physical objective: it allows us to disentangle whether the seasonal nitrate supply is driven**
 438 **primarily by the kinematic modulation of the flow (circulation-driven) or by the pulsing of the**
 439 **nutrient source (supply-driven).** **A high correlation with the current term would identify regional**
 440 **circulation—such as the SEUC or Angola Current—as the primary pump, whereas a dominant**
 441 **correlation with the gradient term would pinpoint the massive periodic enrichment, particularly**
 442 **from the Congo River plume, as the main trigger of nitrate variability.** **By establishing this**
 443 **statistical hierarchy, we can physically characterize the system as being either transport-limited or**
 444 **supply-limited, providing a rigorous diagnostic of the processes regulating primary productivity**
 445 **in the Congolese upwelling.**

446 The Primary production (PP) was calculated from the phytoplankton evolution equation (Aumont
 447 et al 2015):

$$448 PP = \left(\frac{dP}{dt} + \delta^P P \right) \mu^P * P \quad (5)$$

449 In this equation, P is the phytoplankton biomass (diatoms), δ^P represents the exudation of the
 450 phytoplankton (diatoms). μ^P is the specific growth rate of the phytoplankton taking into account
 451 nutrient and light availability. Note that this equation applies to each phytoplankton species
 452 (diatoms or nanophytoplankton), and total NPP is the sum of NPP from both diatoms and
 453 nanophytoplankton. μ^P is the specific growth rate of the phytoplankton taking into account
 454 nutrient and light availability.

455 Net Primary Production (NPP), which represents the organic matter synthesized by phytoplankton after
 456 accounting for autotrophic respiration, is calculated online by the coupled NEMO-PISCES model.
 457 Within the model framework, NPP is partitioned into **New Production (NP)**, fueled by external nutrient

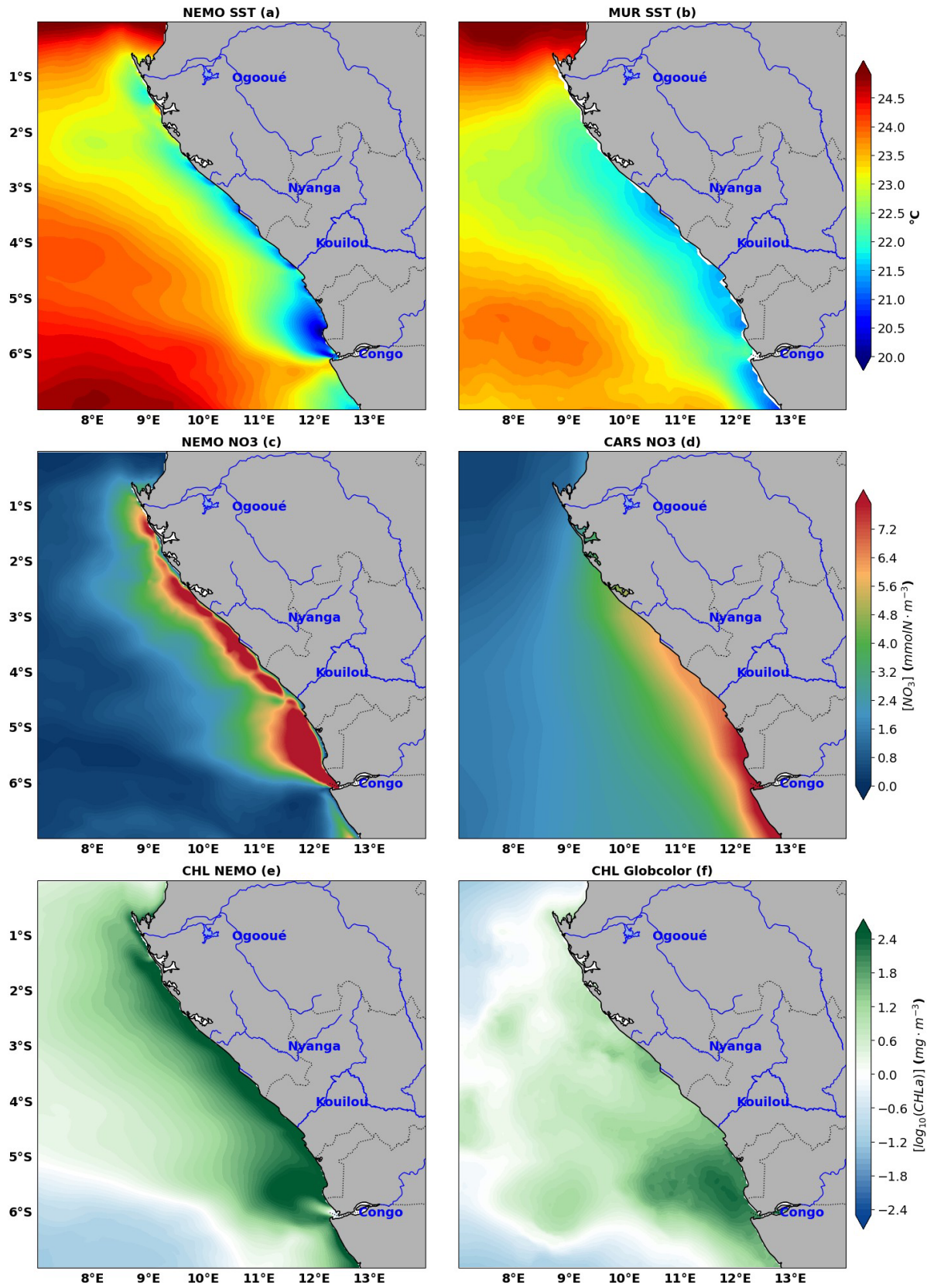
458 | inputs (primarily nitrate) through advection and diffusion, and **Regenerated Production (RP)**,
459 | sustained by nutrients recycled within the euphotic zone (primarily ammonium). Both NP and RP
460 | components are computed online, providing a detailed breakdown of the trophic status and nutrient
461 | utilization efficiency in the Congolese upwelling system. ~~Primary production, based on nutrients actually~~
462 | ~~assimilated by phytoplankton and available light, is calculated online with the coupled NEMO-PISCES~~
463 | ~~model. Primary production is the sum of new primary production (NPP) based on nutrients input by~~
464 | ~~advection and/or diffusion and regenerated production (RPP) based on nutrients regenerated locally.~~
465 | ~~NPP and RPP are also calculated online with the coupled model.~~

466 | **3 RESULTS**

467 | **3.1 Model/data comparison**

468 | **3.1.1 Spatial variations during the upwelling period**

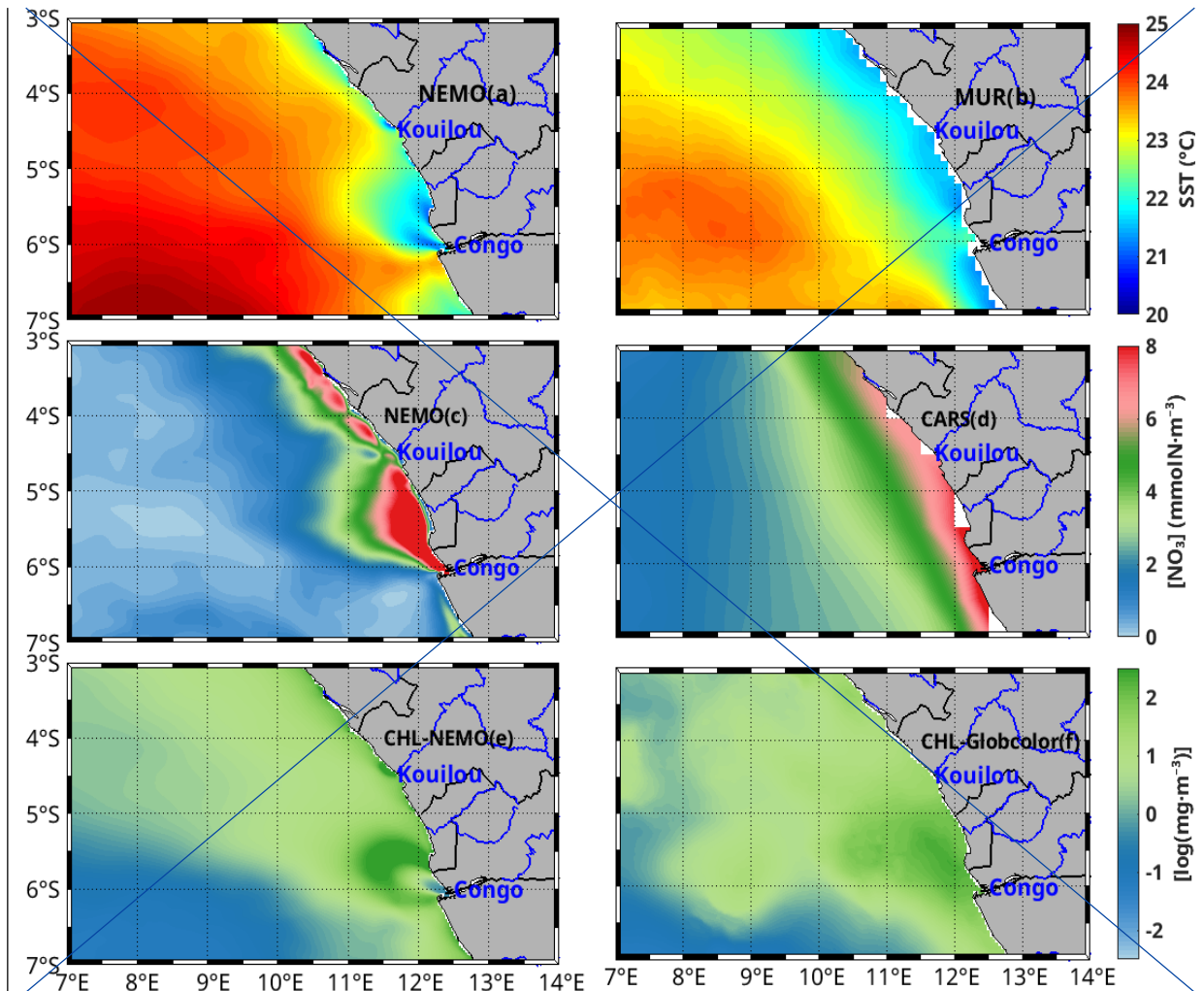
469 | **The assessment of our model simulation has been done using several observation products of**
470 | **physical variables** , including ~~Sea Surface Temperature (SST)~~, Sea Surface Height (SSH), and ocean
471 | ~~currents, as well as biogeochemical tracers such as nitrate (NO₃) and CHLa(SST, SSH and currents) and~~
472 | ~~biogeochemical tracers (NO₃ and CHLa), based on both satellite and in situ data. Figure 2 shows~~
473 | **the regional distribution** ~~from~~ **of observations and model outputs for both SST (Fig.2a-b), nitrate**
474 | **concentration (Fig.2c-d) and CHLa concentration (Fig.2e-f), averaged for austral winter (June-**
475 | **August) which is the main Congolese upwelling period. As can be seen, the upwelling feature is well**
476 | **captured by the model with cooling of surface water at the coast below 23°C in the model and 22°C in the**
477 | **MUR product (Fig. 2a,b). This cooling feature is consistent with high nitrate (Fig. 2c,d) and CHLa (Fig.**
478 | **2e,f) concentrations in both models and observation, particularly north of the Congo estuary (6°S) and**
479 | **nearby Kouilou River mouth (Fig. 2e) at 4.47°S. These cool and enriched nutrient coastal waters are**
480 | **spread offshore displaying a cross-shore gradient, with a greater extension in the observation than the**
481 | **model. The highest nitrate concentration in the coastal waters is greater than 10 mmolN.m⁻³ in the model**
482 | **(8 mmolN.m⁻³ in the observation) located mainly in the Congo River plume area, inducing enhancement**
483 | **of PP resulting in a strong CHLa signature.** ~~winter (June-August) which is the main Congolese upwelling~~
484 | ~~period. As can be seen, the upwelling feature is well captured by the model with cooling of surface water~~
485 | ~~at the coast below 23°C in the model and 22°C in the MUR product. This cooling feature is consistent~~
486 | ~~with high nitrate and CHLa concentrations in both models and observation, particularly north of the~~
487 | ~~Congo estuary (6°S) and nearby Kouilou River mouth at 4.47°S. These cool and enriched nutrient~~
488 | ~~coastal waters are spread offshore displaying a cross-shore gradient, with a greater extension in the~~
489 | ~~observation than the model. The highest nitrate concentration in the coastal waters is greater than 10~~
490 | ~~mmolN.m⁻³ in the model (8 mmolN.m⁻³ in the observation) located mainly in the Congo River plume~~
491 | ~~area, inducing enhancement of PP resulting in a strong CHLa signature.~~



492

493

494



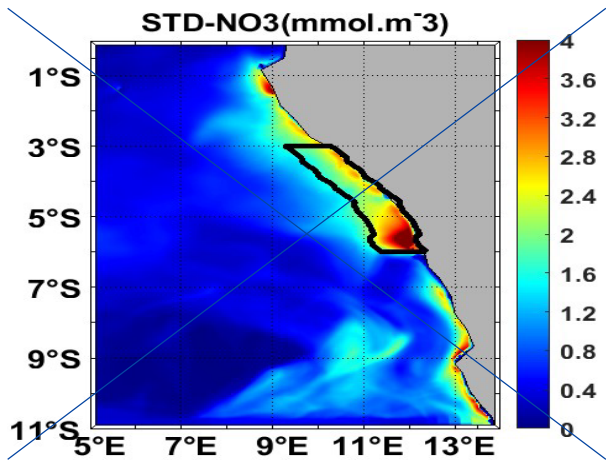
495 Figure 2: Comparison between model (left hand side) and observations (right hand side) with regional
 496 distribution of sea surface temperature (a, b), nitrate concentration (c, d) and CHLa concentration
 497 averaged (e, f) for austral winter (June, July, August)
 498 Figure 2: Comparison between model (left hand
 499 side) and observations (right hand side) with regional distribution of sea surface temperature (a, b), nitrate
 500 concentration (c, d) and CHLa concentration averaged for austral winter (June, July, August).

501 **The offshore area (7°E-10°E) is the oligotrophic zone characterized by relatively warm waters**
 502 **(24.5°C in the model and 23.5°C in the observation), depleted in nitrate and less productive in**
 503 **CHLa concentration. In this offshore area nitrate concentrations are lower than 1.6 mmolN·m⁻³ in**
 504 **the observation and 0.8 mmolN·m⁻³ in the model.**

505 **Although the model captures relatively well the regional distribution of the 3 variables, we can see**
 506 **some differences. For instance, the model is warmer than observations by about 1°C and shows**
 507 **stronger nitrate concentration (by about 2 mmolN·m⁻³) and CHLa concentration (6-10 mg·m⁻³) at**
 508 **the coast. In the offshore area, the model seems to be less enriched in nitrate concentration than**
 509 **the observation by about 0.8 mmolN·m⁻³.**

510 **High variability of nitrate concentration is found in the coastal Congolese area (Fig. 1b3) and in the**
 511 **Congo river plume zone as we can see in model annual standard deviation distribution of NO_3**

512 Therefore, the red/black box (03°S-6°S, 1° width coastal band) in Fig. 1bure-3 is used to analyze the
 513 vertical nitrate profile to assess the model's ability to capture its vertical distribution. This area

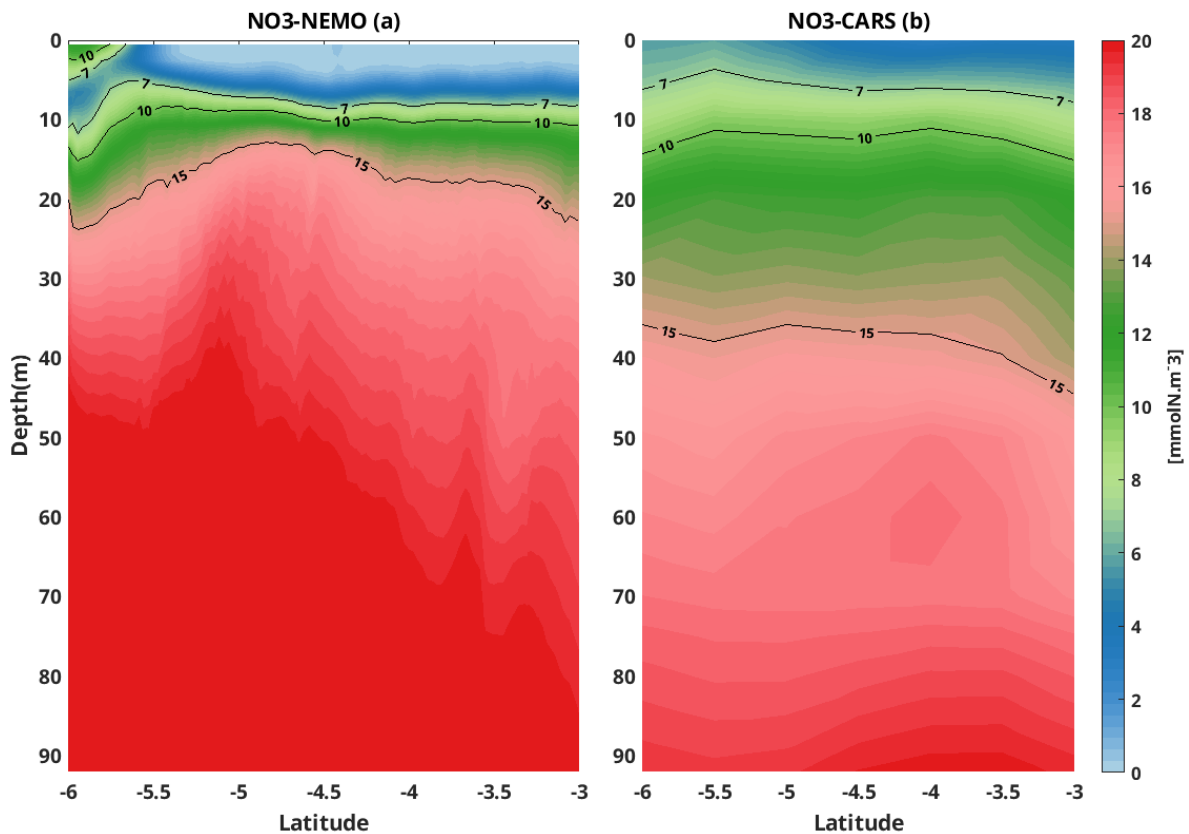


514 corresponds to our studied area in the Congolese
 515 coastal upwelling zone.

516

517

518 **Figure 3:** Regional distribution of standard deviation of nitrate concentration of the model

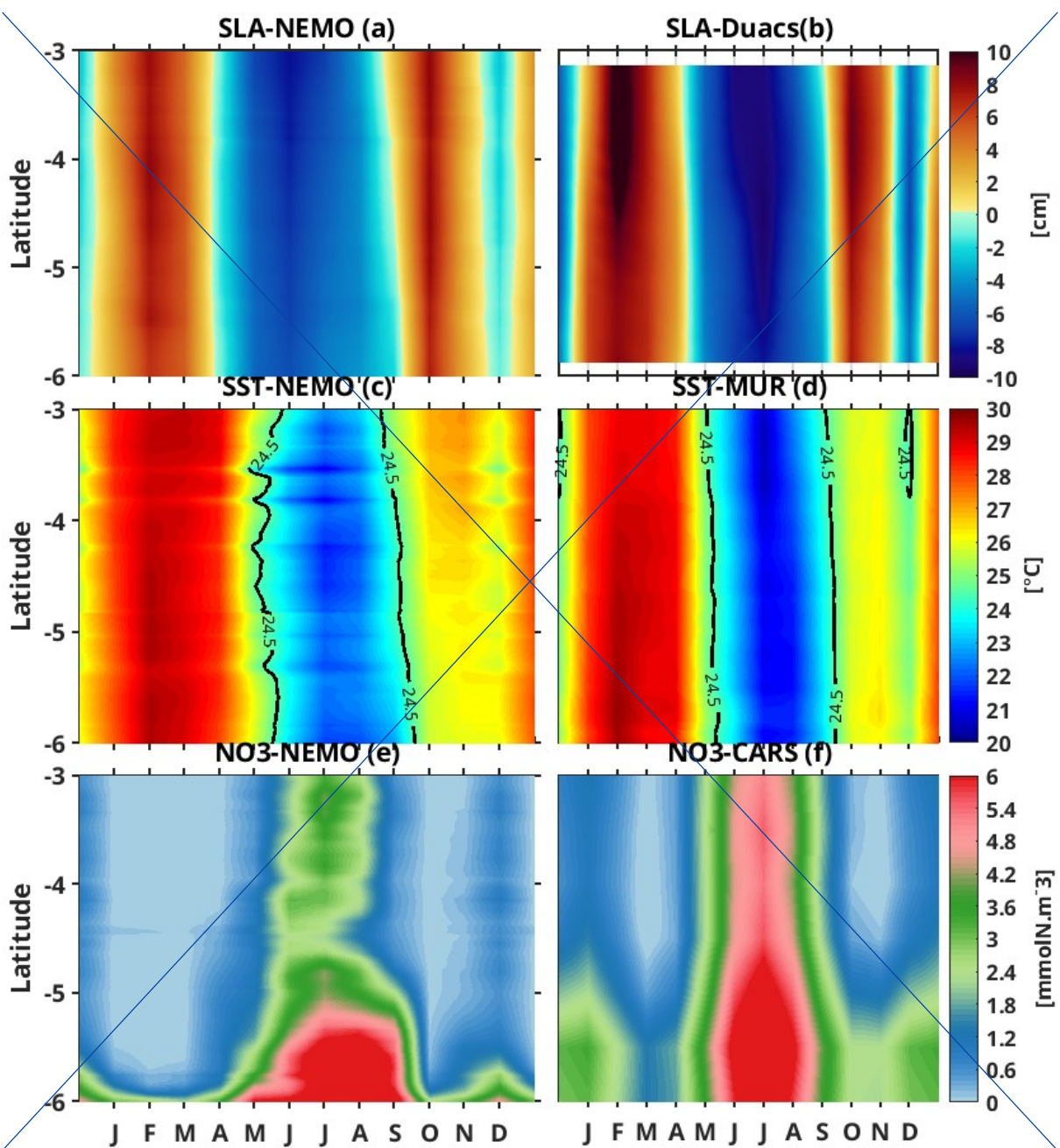


519

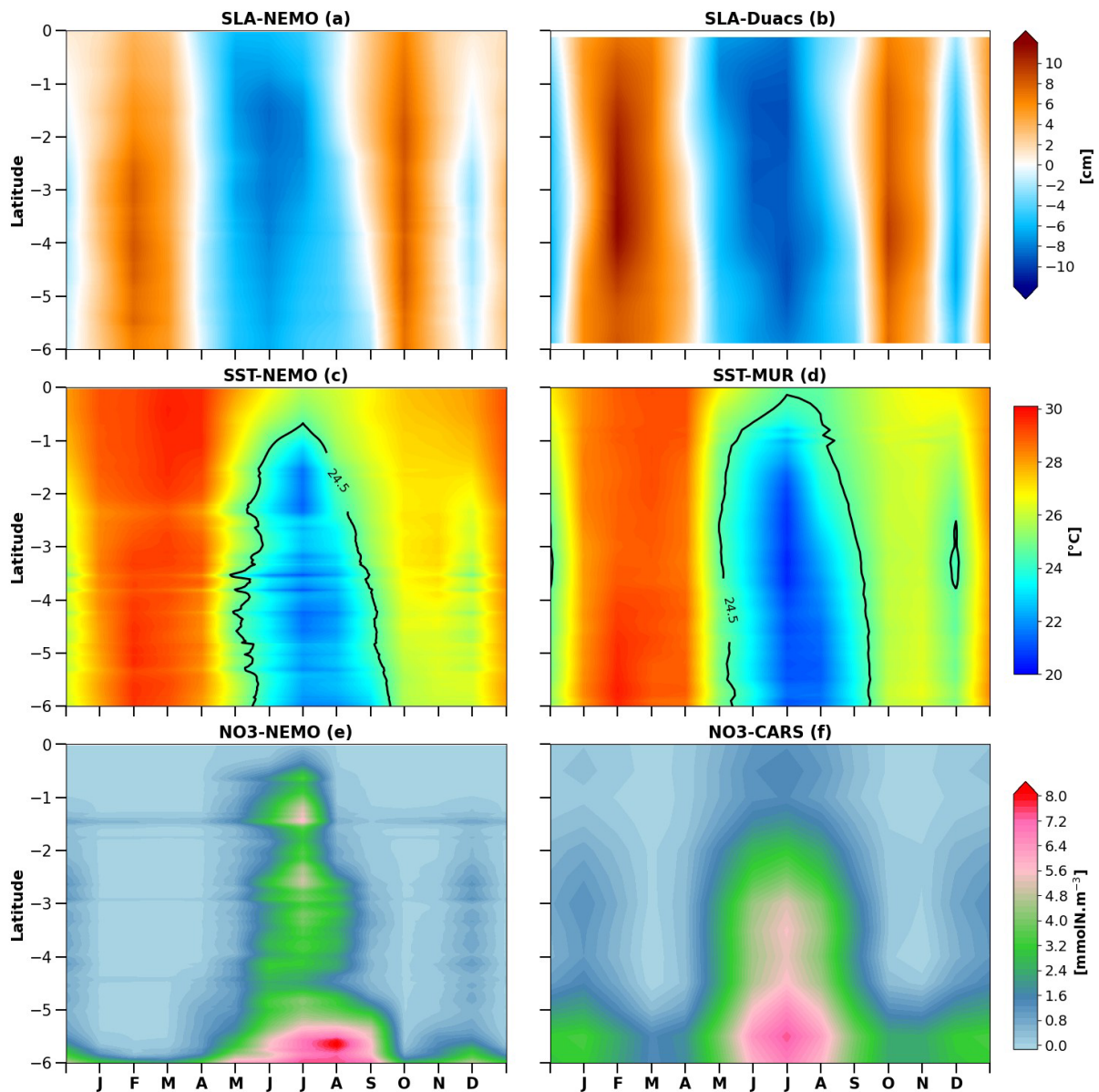
520 **Figure 34:** Comparison between model (a) and observation (b) using vertical distribution of nitrate
 521 concentration in the first 90 m, in the coastal box (03°S-6°S and 1° width band to the coast) in the main
 522 upwelling season (June, July and August). black represents nitrate concentration isolines.

523 Very close to the surface, water masses are nutrient depleted for both model and observation
 524 (Fig.34), likely due to photosynthesis activity of phytoplankton that consumes nitrate in presence
 525 of light, increasing its biomass thus CHLa concentrations. However this depletion is more
 526 pronounced in the model than in the observation. In the subsurface, the high nitrate concentration
 527 is due to the remineralization of organic matter by bacteria and coastal upwelling of deeper
 528 enriched nitrate waters, with the model showing higher concentrations than observed. Although
 529 nitrate isolines are shallower in the model than in observations below about 15 m depth, some
 530 nitrate isolines are relatively well captured by the model, for instance isolines 7 and 10 mmolN.m^{-3} .

531 **3.1.2 Seasonal cycle of SST, nitrate, SLA and current in the Congolese coastal area**



532



533
 534 **Figure 45:** Comparison between modeled (left) and observed (right) seasonal cycles of Sea Level Anomaly (a,
 535 b), nitrate concentration (c, d) and nitrate concentration Sea Level Anomaly (e, f) averaged in the coastal box
 536 (6°S-03°S, 1° width).

537 **Now we use the coastal box defined in Figure 1b4 to evaluate the seasonal cycle of nitrate.**

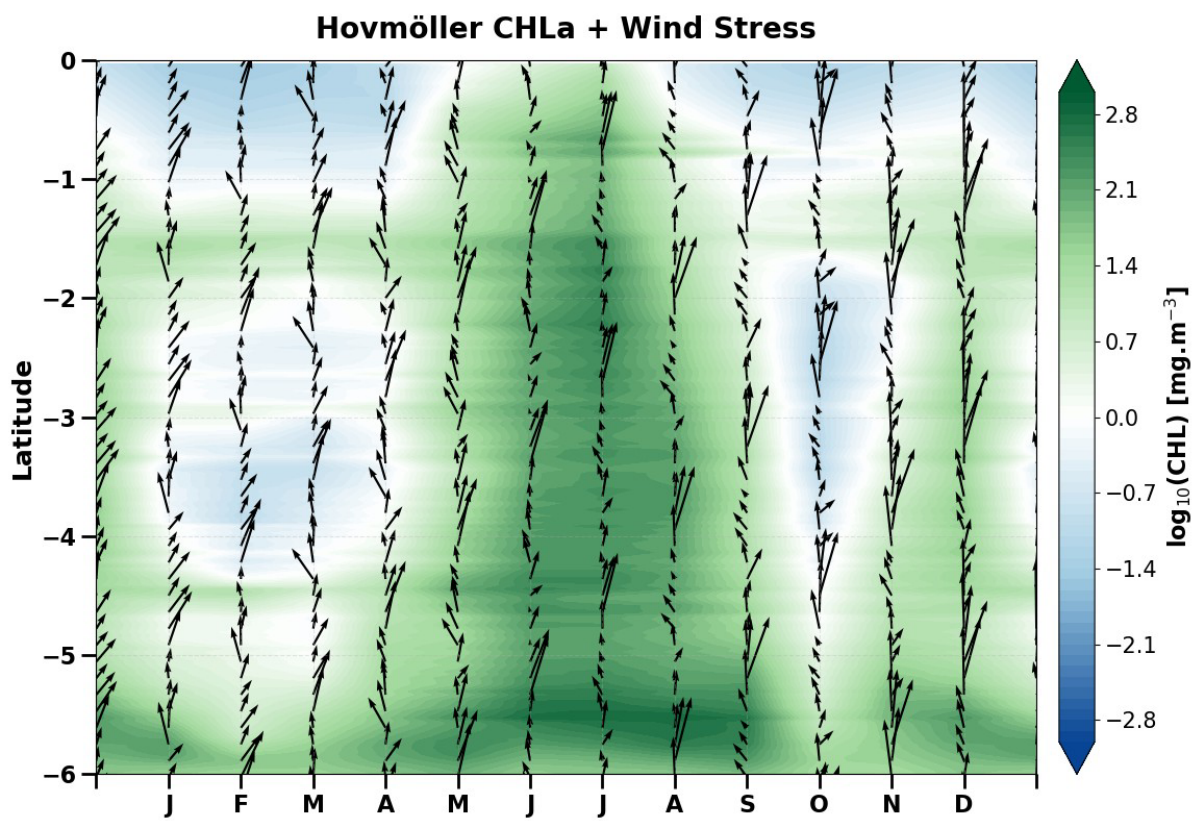
538 The nitrate seasonal variability is characterized by a semi-annual cycle with two maxima and two
 539 minima in the model and the observationsThe nitrate variability is characterized by a semi-annual cycle
 540 with two maxima and two minima in the model and the observations. The main maximum occurs from
 541 May to September when SST reaches its minimum of 20°C in both model and observations
 542 (Fig.45c, Fig.45d) and the secondary maximum occurs in December when SST reaches a
 543 secondary minimum of 25.5°C in the model and 24.5°C in observation. We have a warmer SST
 544 reaching 30°C from January to April and 26°C from October to November in both the model and
 545 the observations. This semi-annual SST cycle is likely due to CTWs propagation since it is
 546 consistent with the SLA seasonal cycle (minimum SST corresponds to negative SLA and

547 maximum SST corresponds to positive SLA) as mentioned earlier by Ngakala et al. (2025) in the
548 same area. Indeed, the propagation of CTWs induce vertical migration of the thermocline
549 resulting thereby in cooling or warming at the surface. At the seasonal scale, the propagation of
550 upwelling CTWs from May to September and in November-December uplifts thermocline,
551 supplying cold waters to the surface and reducing Sea Surface Height (SSH) by steric effect. As
552 downwelling CTWs propagate from January to April and in September-October, they deepen
553 thermocline, warming the surface and increasing SLA. The cold waters upwelled by CTWs (May-
554 September) are highly enriched in nitrate, whereas warm surface waters induced by downwelling
555 CTWs (January-April and September-October) are nitrate depleted. The seasonal variability of
556 SLA due to CTWs (Fig.45a, Fig.45b) is consistent with the seasonal variability of SST (Fig.45ca,
557 Fig.45d) and of nitrate concentration (Fig.45e, Fig.45f) in both the model and observations. The
558 highest nitrate concentration is around 10 mmol.m^{-3} near the Congo River mouth (6°S) and
559 decreasing northward, however the observations seem to be richer in nitrate than the model. In
560 December during the secondary cooling, nitrate concentration in the model is greater by about 1.2
561 mmol.m^{-3} than observed along the coast. In the warming period (January-April and October-
562 November), this coastal area seems to be nitrate depleted.

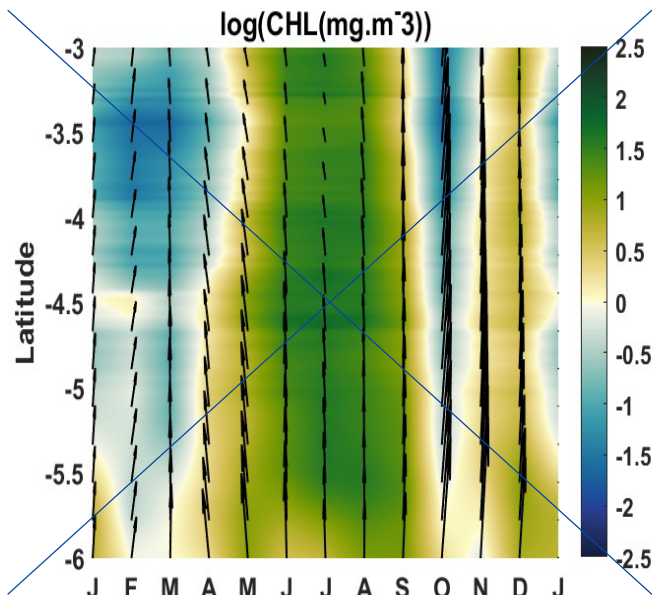
563 Despite the model capturing the SLA signature, the observed seasonal cycle of SLA remains more
564 intense than in the simulation. This feature is driven by the combined effect of remotely forced
565 Equatorial Kelvin Waves (EKW) and poleward-propagating CTWs (Bachelery et al., 2016; Kopte et
566 al., 2017; Awo et al., 2023; Brandt et al., 2023). During cooling periods, upwelling CTWs decrease the
567 SLA and uplift the thermocline. Following Radenac et al. (2020), the thermocline depth in this region
568 acts as a reliable proxy for the nitracline; its upward migration significantly enhances nitrate supply to
569 the surface, fueling biological productivity. Conversely, the downwelling waves observed in the
570 warming periods increase the SLA and deepen the nitracline, leading to the nutrient-depleted conditions
571 described previously. However, despite this well captured SLA signature by the model, the seasonal cycle
572 of SLA is more intense in the observations than in the model. Previous studies (Bachelery et al 2016,
573 Kopte et al 2017, Awo et al 2023, Brandt et al 2023) have shown that this sea level anomaly feature is due
574 to combined effect of Equatorial Kelvin Waves (EKW) remotely forced at the equator and the CTWs
575 propagating poleward along the African coast. In summary, during the cooling period, the CTWs
576 inducing upwelling travel along the coast decreases SLA and raises in the thermoeline which can be
577 taken as nitracline proxy (Radenac et al 2020), thereby enhancing nitrate supply at the surface.

578 **High nitrate concentrations support biological production, therefore correspond to high CHLa**
579 **signals at the surface (Fig.56). On the contrary, during the warming period, the downwelling**
580 **CTWs downwelling propagating along the coast increase SLA, deepen the thermocline**
581 **(Ngakala et al. (2025). This also deepen the nitracline and consequently deplete the nitrate**
582 **concentration at the ocean surface, thus the low CHLa signal (Fig.56).**

583 The variability of simulated near-surface currents between 0 to 15 m depth (Fig.67) was compared
584 to the OSCAR product. Here, we make a latitudinal section at 4°S and look at the seasonal cycle of
585 meridional currents (Fig.67a and 67b) from 7°E to the coast for both the model (Fig.67a) and
586 observations (Fig.67b). We do not restrict to the Congolese box as we have done for other
587 variables, because the OSCAR product is not well resolved at the vicinity of the coast. So we can
588 see that the model reasonably represents the seasonal variability of meridional currents with
589 northward velocities in April, June-September and November-December with the magnitude of
590 around 0.1 m.s⁻¹. In the observations, this structure is more or less similar, but we can see some
591 differences: southward velocities between 8.5°E and 10.2°E in July, and also between 7°E and 9°E
592 during August-September and January, are not found in the model.



593



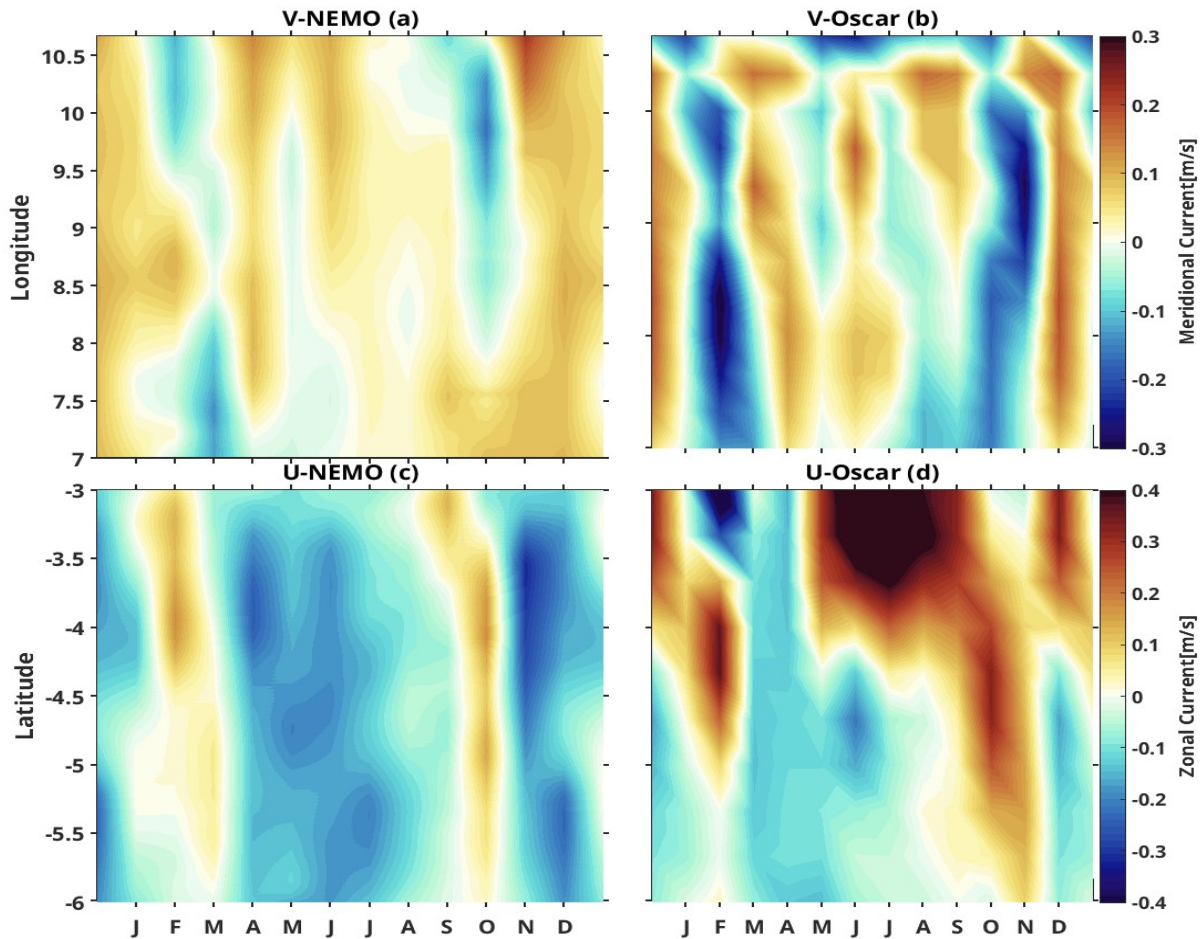
594
 595 **Figure 56:** Seasonal cycle of CHLa concentration (in background) and wind stress (black arrow) along the
 596 **Congolese coastal box (6°S-03°S, 1° width) area in the model.**

597 Nevertheless, we can see in both products southward currents in February-March and October
 598 with a strong magnitude of 0.25 m.s^{-1} in the observations though only 0.15 m.s^{-1} in the model. This
 599 seasonal structure is consistent with the seasonal cycle of meridional currents off Angola, further
 600 south, and the southward flow in February-March and October seems to be the Angola current
 601 (Kopte et al 2017). To assess the zonal current (Fig.67c and 67d), we make a longitudinal section at
 602 10°E and we look at the seasonal cycle of zonal current between 3°S and 7°S . The modeled zonal
 603 structure with westward velocities from April to August and November – December has—a
 604 magnitude of about 0.1 m.s^{-1} along the section (Fig.67c), in agreement with the observations
 605 (Fig.67d), which also show westward velocities from April to August. However there are some
 606 differences with the model from March to August between 3°S and 4.5°S where we can observe
 607 very strong (more than 0.5 m.s^{-1}) eastward flow. In contrast to the model, the flow during
 608 November is eastward in the observation. The noticeable similitude is the eastward flow in
 609 January- February and October with a magnitude of 0.15 m.s^{-1} which seems to be the signature of
 610 the South Equatorial UnderCurrent (SEUC). This eastward current is deeper further offshore
 611 (100 m depth) west of 0°E (Bourles et al., 2004) and rising near the surface near the coast (Nubi et
 612 al., 2016; Assene et al., 2022).

613 3.2 Nitrate budget in the mixed layer

614 Generally, the seasonal variations in CHLa are thought to be primarily related to seasonal
 615 variations of the nitrate input in the equatorial Atlantic ocean (Loukos and Mémer., 1999;
 616 Radenac et al, 2020) and in the tropical Angolan upwelling (Brandt et al., 2023). This is probably
 617 the case also in the Congolese coastal area, where the seasonal cycles of nitrate (Fig.7&a) and
 618 CHLa-a (Fig.56) in our model are very consistent. Corresponding to the semi-annual variability of

619 nitrate, the seasonal change rate of its concentration (Fig. 8b) displays a four-phase cycle: a first
 620 increasing phase Like the seasonal cycle of nitrate, the seasonal change rate of nitrate concentration
 621 (Fig. 8b) has a semi-annual cycle with four phases: a first increasing phase between March and
 622 July/August with a highest amplitude (0.31 mmol.m⁻³.d⁻¹) in June/July, followed by a decreasing phase
 623 in August/September –November with a highest amplitude in October (0.018 mmol.m⁻³.d⁻¹ north of
 624 5°S and about -0.13 to -0.35 mmol.m⁻³.d⁻¹ between 5°S and 6°S all years long).



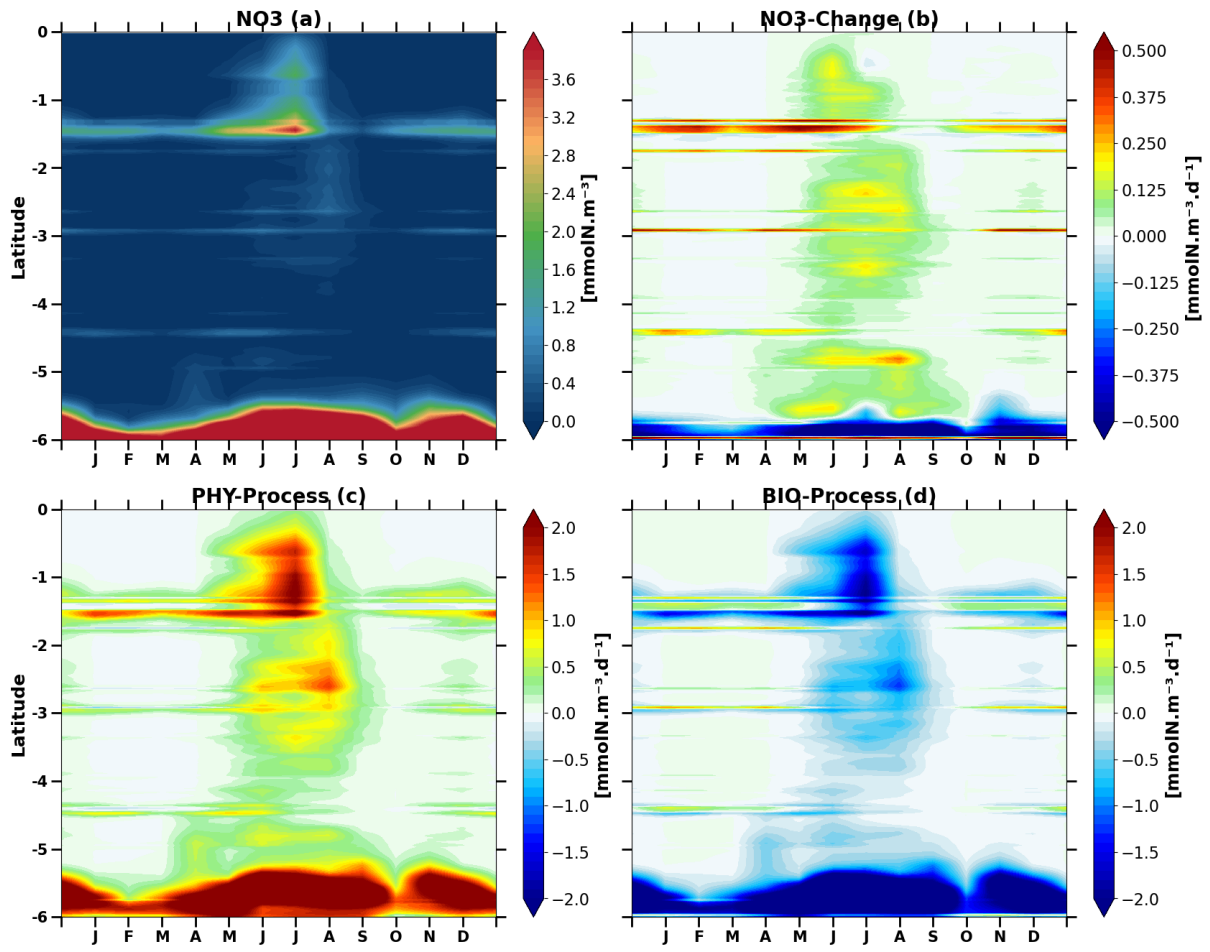
625
 626 **Figure 67:** Seasonal cycle of surface current, zonal current (a, b) at 10°E section and between 3°S and 7°S
 627 and meridional current (c, d) at 4°S section from 7°E to the coast.

628 Then we have a weak second increasing phase in November-December of about 0.103
 629 mmol.m⁻³.d⁻¹ and a weak decreasing phase in January- February (0.01 mmol.m⁻³.d⁻¹). This semi-
 630 annual cycle is due to a balance between nitrate supply by physical processes (Fig. 7&c), maximum
 631 during the main upwelling period, and nitrate consumption by biological processes (Fig. 7&d).

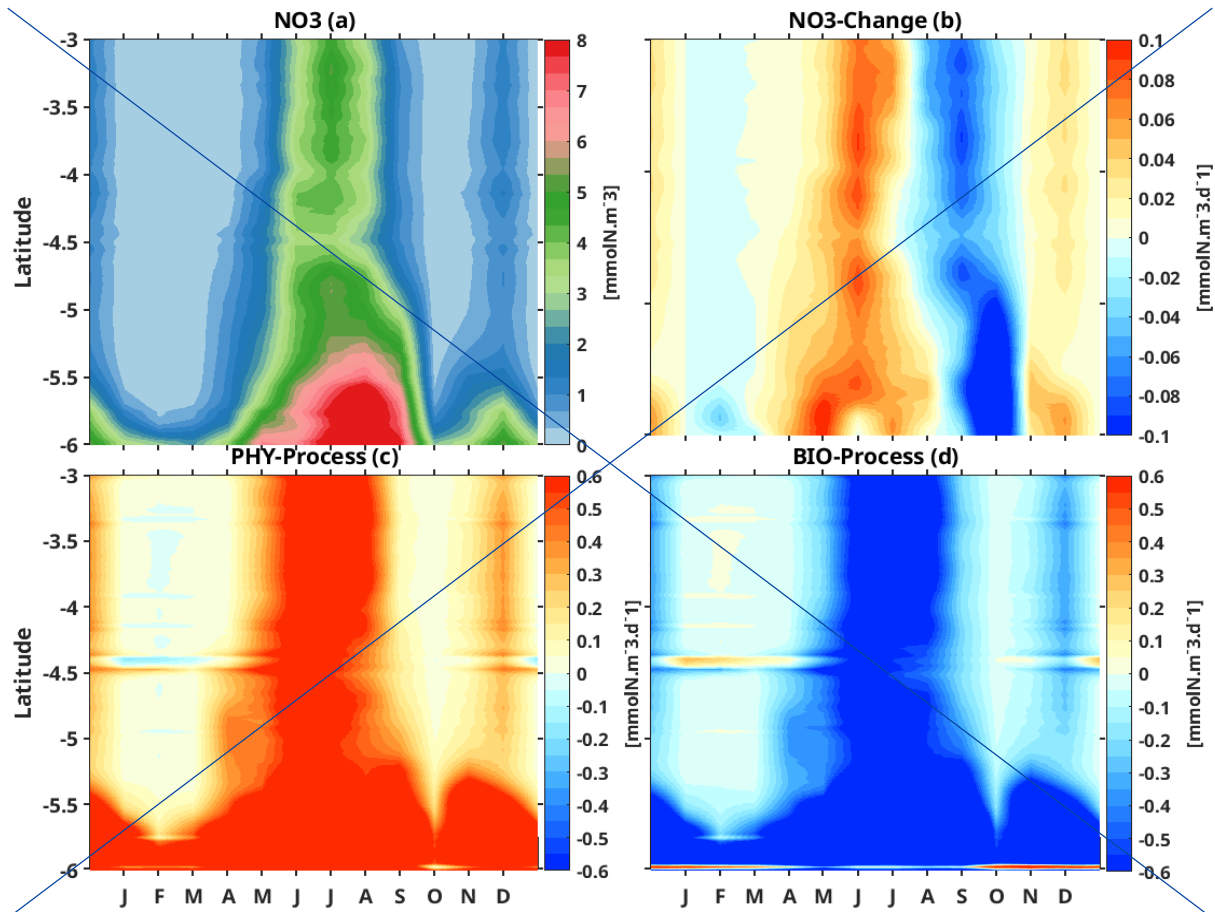
632 3.2.1 Seasonal Nitrate Budget Analysis: Horizontal Vs Vertical Contributions

633 Looking at our previous results, we saw that physical processes drive the nitrate supply in the
 634 Congolese upwelling system, now we will look at the contribution of horizontal and vertical
 635 processes to understand which are the main drivers for this nitrate supply. Fig. 4&e-89 shows that

636 horizontal and vertical processes (Fig. 89a and Fig. 89b respectively) are of great importance for
637 nitrate supply.



638



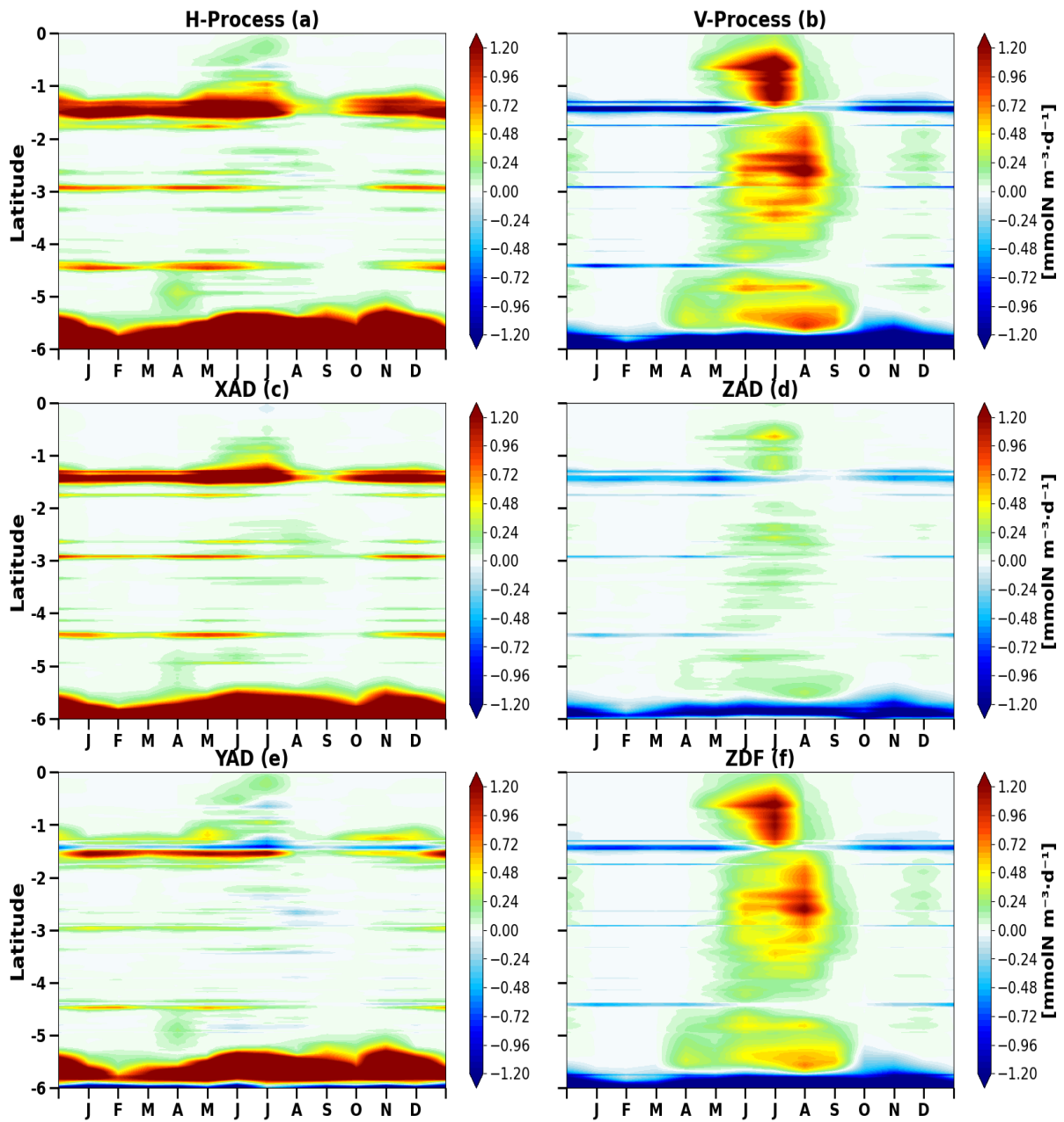
639

640 **Figure 78:** Latitude-time Hovmöller diagram of the model seasonal cycle of Mixed Layer Nitrate (MLN)
 641 budget, a), the rate of the MLN change (b), the physical process contribution (c) and the biological process
 642 contribution (d) along the Congolese coast. Units are mmolN.m^{-3} and $\text{mmolN.m}^{-3}.\text{d}^{-1}$ for Figure 7a and
 643 Figure 7b,c,d, respectively.

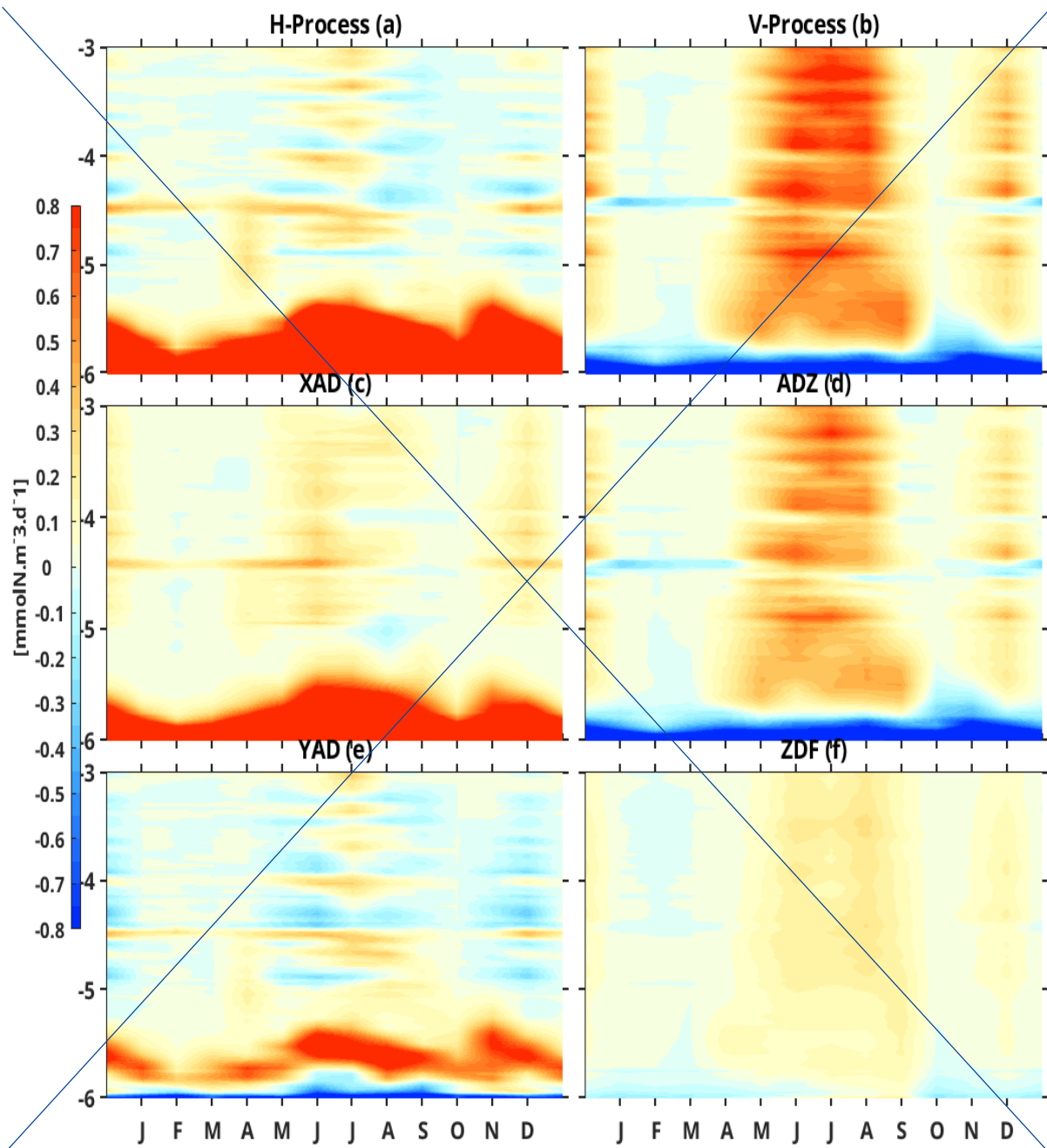
644 In fact, as we can see in the Figure 88, vertical processes (Fig. 89b) are the main driver of nitrate
 645 supply during the upwelling between 0°S and 5.5°S with an input magnitude of around 10.6
 646 $\text{mmol.m}^{-3}.\text{d}^{-1}$ along the coast while the horizontal processes are the main driver at the vicinity of
 647 Congo river mouth ($5.5^{\circ}\text{S} - 6^{\circ}\text{S}$) all year long. The latter seems to be dominated by zonal advection
 648 (fig. 89c) with a very high nitrate input of more than $1.2 - 0.8$ $\text{mmolN.m}^{-3}.\text{d}^{-1}$ nearby 6°S with a
 649 northward extension, largest firstly in November-December and secondly in June-July. This is
 650 consistent with the seasonal maximum of Congo River discharge, which suggests a nitrate input
 651 through the river plume (Hopkins et al 2013). North of 6°S , meridional advection (Fig. 89e) drives
 652 horizontal processes.

653 The nitrate budget analysis reveals also that vertical processes (Fig. 89b) are dominated by vertical
 654 mixing advection (Fig. 89d), while vertical advection mixing has the same seasonality but a smaller
 655 contribution (Fig. 89f). Indeed, the nitrate input by the vertical diffusion advection is about
 656 0.745 $\text{mmolN.m}^{-3}.\text{d}^{-1}$ but only around 0.25 $\text{mmolN.m}^{-3}.\text{d}^{-1}$ by vertical advection diffusion. Both
 657 vertical processes decrease nitrate concentration nearby 6°S , under Congo River plume influence
 658 with the dominant zonal advection contribution. Indeed, as nitrate concentration is greater in the

659 near-surface Congo River plume than in subsurface (between 5 to 10 m, see Fig.34), deeper waters
660 rising at the surface by vertical advection reduce nitrate in the plume area.



661

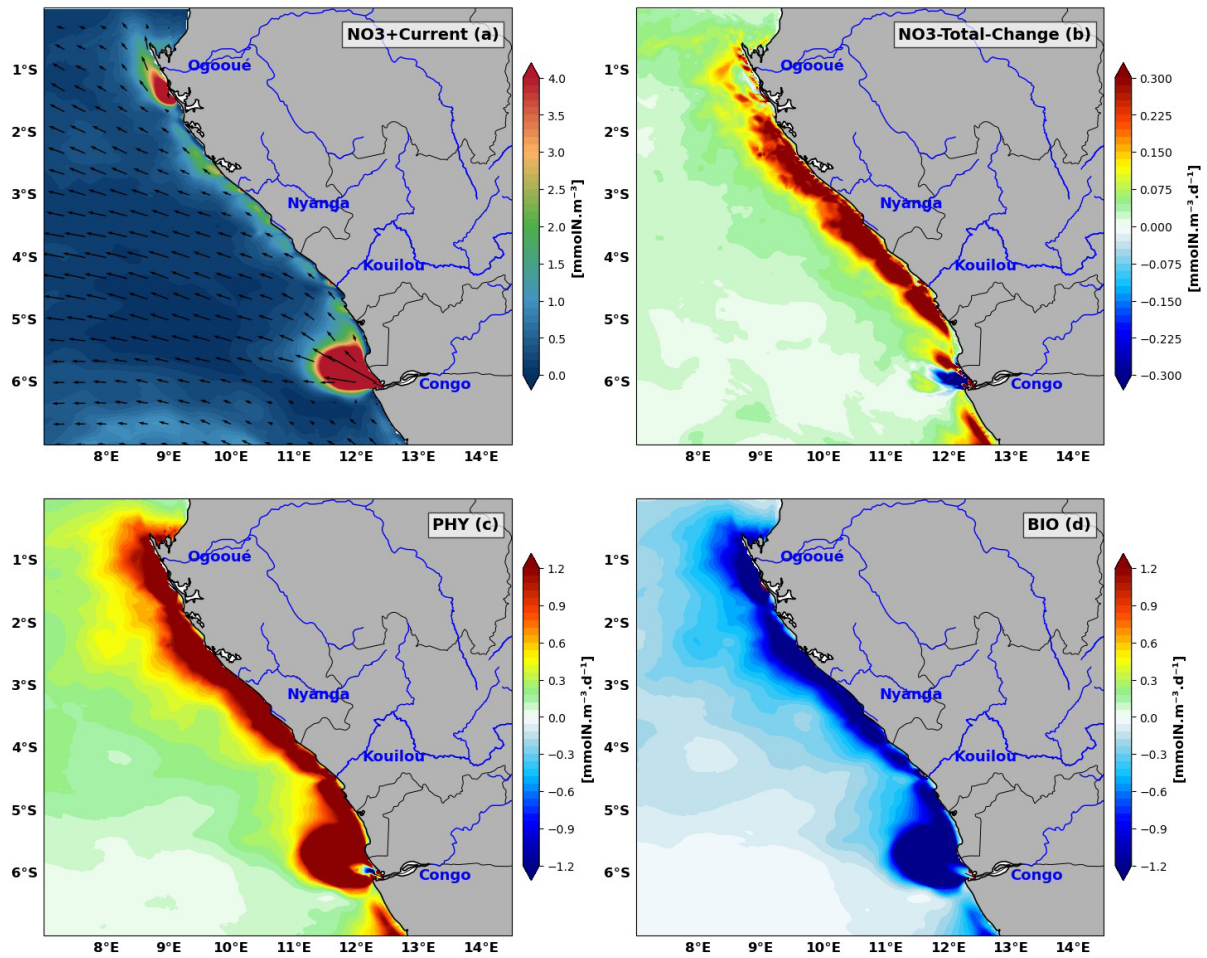


662
 663 **Figure 89:** Latitude-time Hovmöller diagram of the model seasonal cycle of horizontal (a) and vertical (b)
 664 process contributions, zonal (c), meridional (e), vertical (d) advections, vertical diffusion (f) averaged in the
 665 mixed layer along the Congolese coast. Units are $\text{mmolN.m}^{-3}.\text{d}^{-1}$.

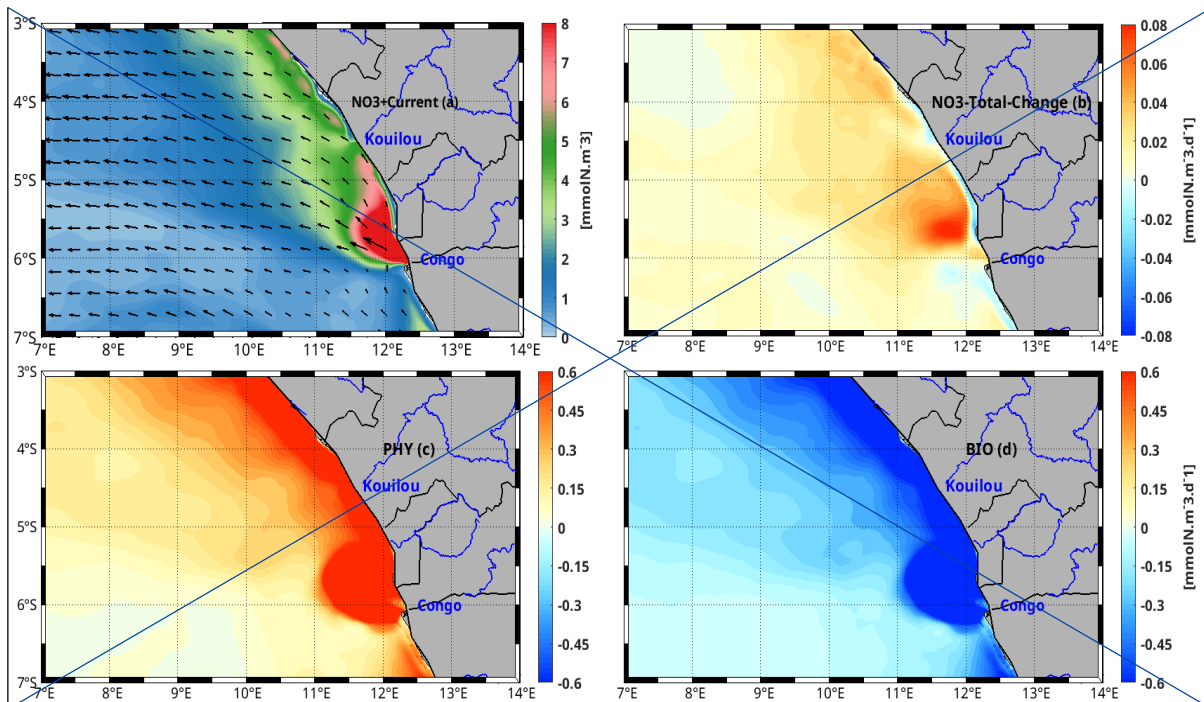
666 Similarly, vertical mixing of subsurface waters with the plume waters decreases nitrate
 667 concentration at the surface, although the strong haline stratification associated with the Congo
 668 River plume limits this effect.

669 It is important to note that, on the one hand, vertical advection (Fig. 8d) and vertical diffusion (Fig. 8f)
 670 have the same seasonality as SLA (Fig. 4a), in opposite phase, northward of 5.5°S . It is important to note
 671 that, on the one hand, vertical advection and vertical diffusion have the same seasonality as SLA, in
 672 opposite phase, northward of 5.5°S . This suggests that the upwelling associated with CTWs
 673 (negative SLA) induce these vertical processes and therefore drive the input of nitrate in the

674 northern part of the Congolese coast. On the other hand, horizontal advection (both zonal and
 675 meridional advectons) has the same seasonality as the Congo River discharge between 5.5°S and
 676 6°S. This suggests that the Congo River supplies nitrate through zonal advection, near its mouth.



677



678

679 **Figure 910: Spatial distribution averaged over the main upwelling period of (a) nitrate, (b) nitrate tendency**
680 **contributed by (c) physical processes and (d) biological processes, all averaged in the mixed layer in Austral**
681 **winter. The mean current in the mixed layer is superimposed in (a). Nitrate concentration units are mmolN.m^{-3}**
682 **and the tendency terms units are $\text{mmolN.m}^{-3}.\text{d}^{-1}$.**

683 **3.2.2 Regional Nitrate Budget Analysis in the main upwelling period: Physical Vs** 684 **Biological Contributions**

685 **The regional distribution of nitrate balance terms averaged over the mixed layer for the austral**
686 **winter (June-July-August), when upwelling reaches its maximum intensity, is presented in**
687 **Figure 910. The nitrate tendency (Fig. 910b) shows that during the upwelling period, nitrate input**
688 **occurs throughout the domain with a high values varying between of -0.3 to $0.308 \text{ mmolN.m}^{-3}.\text{d}^{-1}$ in**
689 **the plume zone and 0.2 to $0.506 \text{ mmolN.m}^{-3}.\text{d}^{-1}$ along the coast in the northern part. In the offshore**
690 **zone, the nitrate tendency is lower, with a magnitude of around $0.052 \text{ mmolN.m}^{-3}.\text{d}^{-1}$. This**
691 **distribution of the nitrate tendency shows that the input of nitrate by physical processes (Fig. 910c)**
692 **is slightly greater than the uptake of nitrate by biological processes (Fig. 910d) throughout the**
693 **area, explaining the positive nitrate change rate, except at the Congo River mouth where we have**
694 **negatives values, explaining the positive nitrate change rate. Fig. 9a shows that nitrate inputs along the**
695 **coast are very high close to river mouth and varies a lot along the coast over a width of about 165 km**
696 **from the coast. Figure 10a shows that nitrate inputs along the coast are very high over a width of about**
697 **1.5° longitude from the coast. During this main period of upwelling, in general, vertical processes**
698 **(Fig. 10b) largely dominate the nitrate supply across the entire continental shelf. A continuous**
699 **coastal band of strong enrichment is observed, with values often exceeding 0.513 to 0.677**
700 **$\text{mmolN.m}^{-2}.\text{d}^{-1}$. Conversely, horizontal processes (Fig. 10a) show a more localized and overall**
701 **lower contribution throughout the domain, with the notable exception of the Congo and Ogooué**
702 **River mouth ($\sim 6^\circ\text{S}$ and 1°S respectively), where a massive positive flux (dark red, > 0.677**
703 **$\text{mmolN.m}^{-2}.\text{d}^{-1}$) is observed. Comparing the spatial structure of the total horizontal process (Fig. 10a)**
704 **with its individual components reveals a striking similarity to zonal advection (Xad, Fig. 10c). The Xad**
705 **signal (Fig. 10c) almost perfectly reproduces the nitrate patch observed at the Congo mouth, indicating**
706 **that zonal transport (east-west) is the main driver of horizontal nitrate injection into the mixed layer,**
707 **associated with the offshore extension of the river plume. Although meridional advection (Yad, Fig.**
708 **10e) exhibits significant dipole structures near the Congo and patches along the coast, its intensity and**
709 **spatial pattern provide a less compelling explanation for the overall horizontal process signal. It can**
710 **therefore be concluded that zonal advection is the dominant term dictating the distribution of horizontal**
711 **fluxes in this region. The study of vertical components shows that the total vertical process (Fig. 10b)**
712 **results from two distinct yet complementary mechanisms. Vertical advection (Zad, Fig. 10d) shows**
713 **very intense ($> 0.677 \text{ mmolN.m}^{-2}.\text{d}^{-1}$) but highly localized supply along the coastline and capes,**
714 **representing the typical signature of coastal upwelling driven by wind and Coastally Trapped Waves**

715 (CTWs). However, vertical diffusion (**Zdf**, Fig. 10f) shows the strongest resemblance to the overall
716 **Vert Process**. It exhibits a broad and homogeneous distribution extending well offshore from the coast,
717 with sustained values between **0.349 and 0.513 mmolN.m⁻².d⁻¹**. Unlike advection, which is highly
718 segmented, vertical diffusion better explains the spatial continuity of nitrate supply across the shelf. This
719 suggests that while advection (upwelling) brings nitrate to the base of the mixed layer, turbulent mixing
720 (diffusion) ensures its effective distribution toward the surface across the entire domain. Vertical
721 processes (Fig.11b) dominate the physical contribution to nitrate supply throughout the domain, except
722 in the fluvial plume region where horizontal processes (Fig.11a) dominate. Vertical advection
723 dominates the nitrate supply along the coast and north of the river mouth (Fig.11d), while vertical
724 diffusion (Fig.11f) appears to be the main driving process for the relatively weak nitrate supply south of
725 the river mouth in the northern part of the Angolan coast (between 6°S and 7°S).

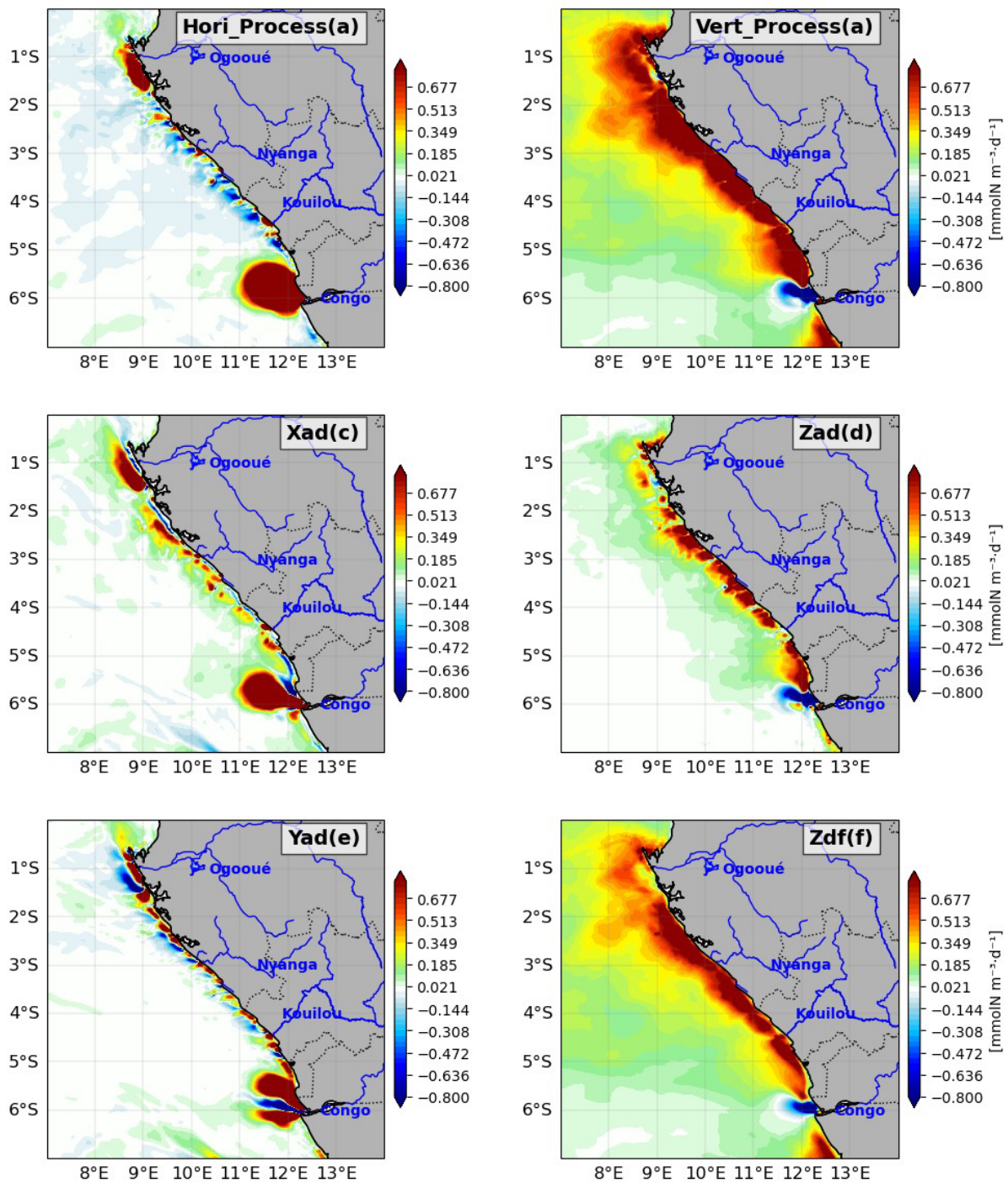
726 **3.3 Nitrate budget in the euphotic layer and along the water column**

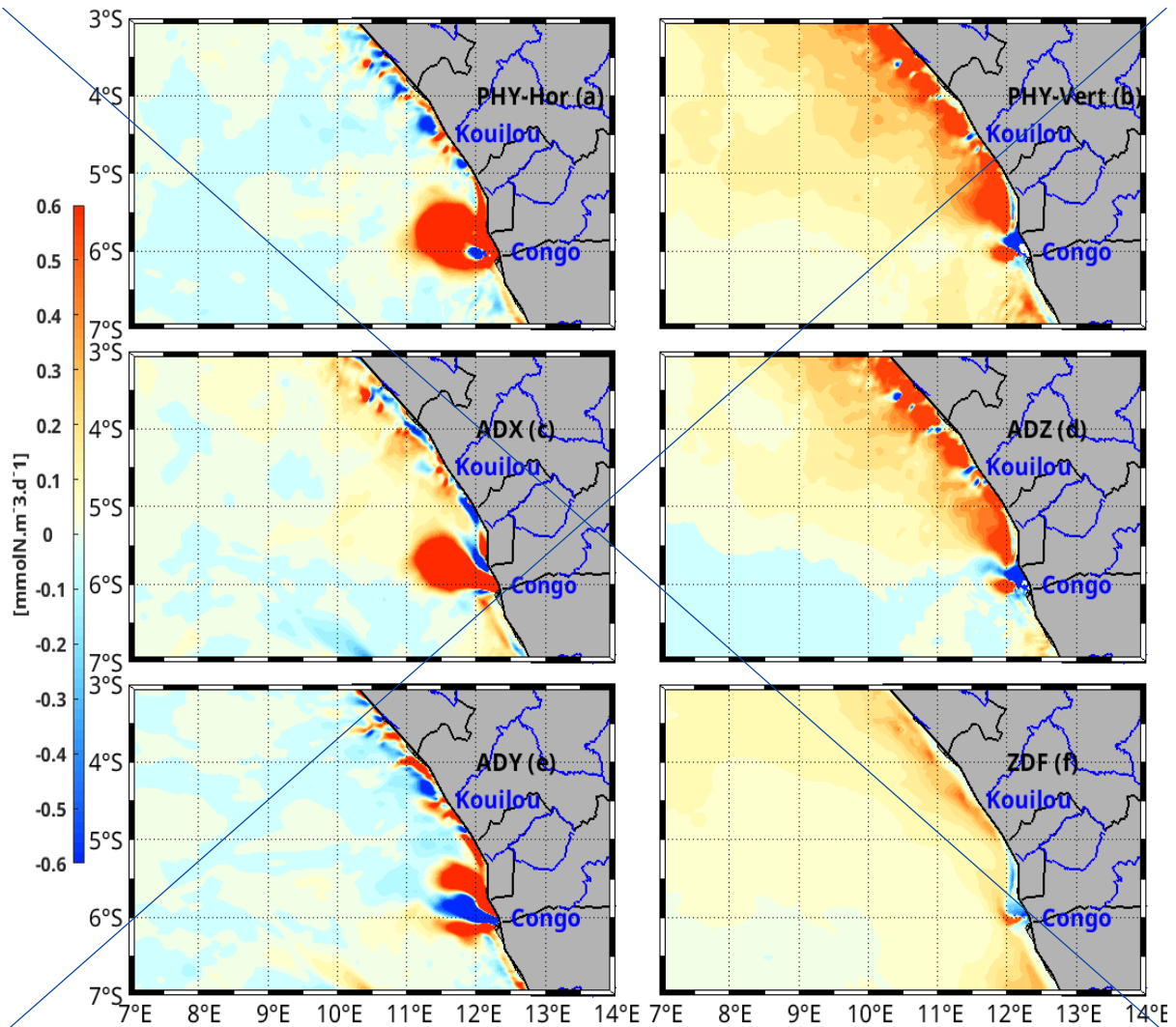
727 Now, in addition to the processes acting in the surface mixed layer, we **investigate** look for other
728 processes involved in the nitrate budget below the mixed layer by analysing the nitrate budget in
729 the euphotic layer, generally defined as the zone where light penetration exceeds 1% of the surface
730 light, allowing for the presence of phytoplankton and other photosynthetic organisms. The
731 seasonal variations of thermocline, mixed layer and euphotic layer depths are compared in
732 Fig.111e-12. In Fig.112a, the thermocline (20°C isotherm) variation is very close to the nitracline
733 as suggested by Radenac et al (2020). The mixed layer euphotic layer is very shallow (~ 10 m)
734 throughout the year probably due to the Congo River plume stratification. The euphotic layer
735 extends deeper than the mixed layer, but is generally shallower than the thermocline, except from
736 June to September. The euphotic layer gets thinner during upwelling through the enhancement of
737 CHLa concentration which reduces light penetration (self-shadowing by CHLa). Overall the
738 nitrate tendency (Fig.112b) has the same semi-annual variation in the euphotic layer than in the
739 mixed layer, although more intense in the euphotic layer with a maximum at the bottom of the
740 euphotic layer. In fact, most nitrate input by physical processes (Fig.112c) happens in the mixed
741 layer, where it is almost balanced by biological nitrate uptake (Fig.112d). In contrast, in the
742 euphotic layer below the mixed layer (between 10m and 40m depth), biological processes are
743 poorly active and the nitrate variability is almost exclusively induced by physical processes. The
744 mean nitrate input in the euphotic layer is about 0.1 mmolN.m⁻³.d⁻¹ during the main upwelling
745 period and the maximum input (0.2 mmolN.m⁻³.d⁻¹) occurs in May at the base of the euphotic layer
746 (Fig.112b).

747 In the euphotic layer, biological activity is dominated by photosynthesis which removes nitrate,
748 whereas below the euphotic layer remineralization supplies nitrate with about 0.05 mmolN.m⁻³.d⁻¹
749 almost all year long (Fig. 112d).

750 | **3.3.1 Euphotic Layer Nitrate Budget Analysis: Horizontal Vs Vertical Contributions**

751 | Fig.12 are 13 shows that, even in the euphotic layer, the physical contribution to nitrate supply
752 | (Fig.112c) is mostly driven by vertical processes (Fig.123b). However, the large decrease in nitrate
753 | (Fig.112b) in October is also caused by horizontal contributions (Fig.123a) in the euphotic layer.
754 | Between the surface and 5m depth, horizontal processes dominate nitrate input (Fig.123e). In the
755 | euphotic layer below, meridional advection is the main driver of nitrate removal almost year-
756 | round, particularly in June and October.





758

759

760

761

762

763

764

765

766

767

768

769

770

771

772

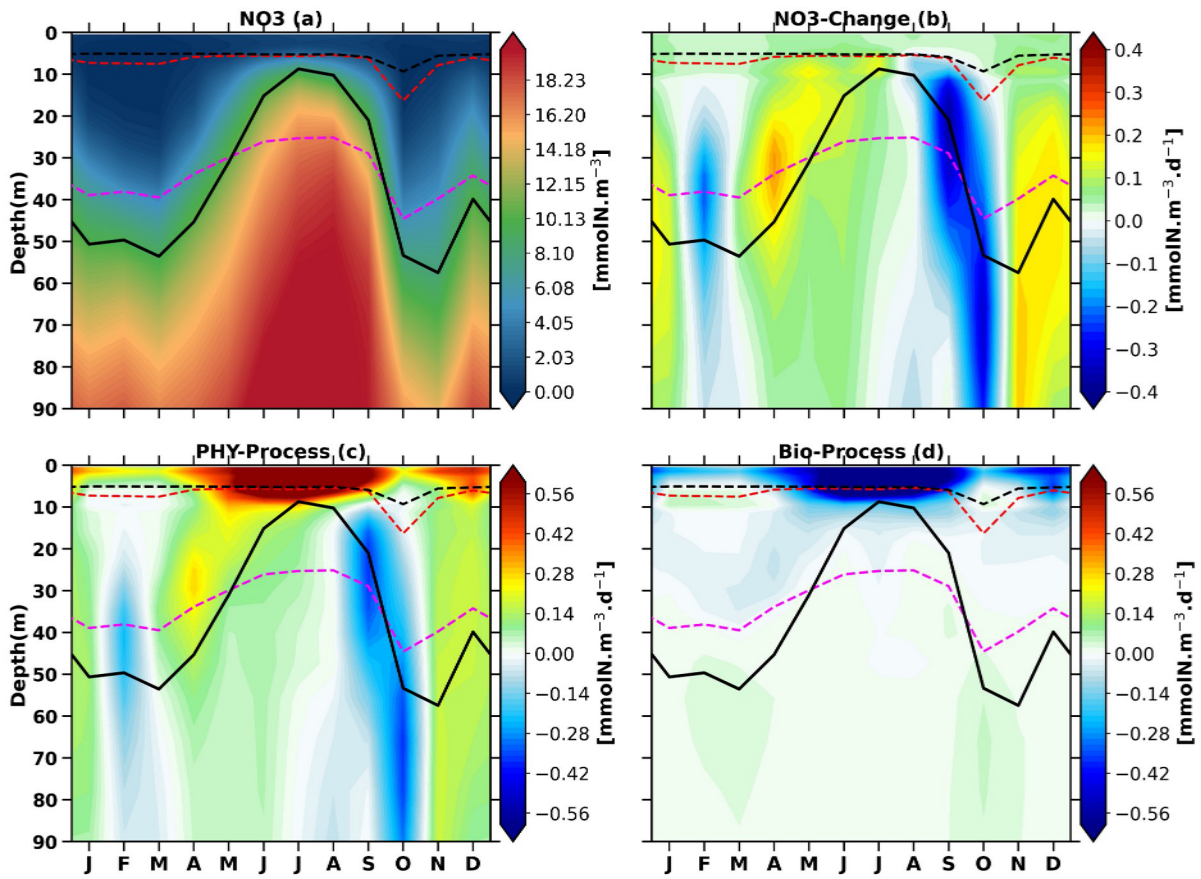
773

774

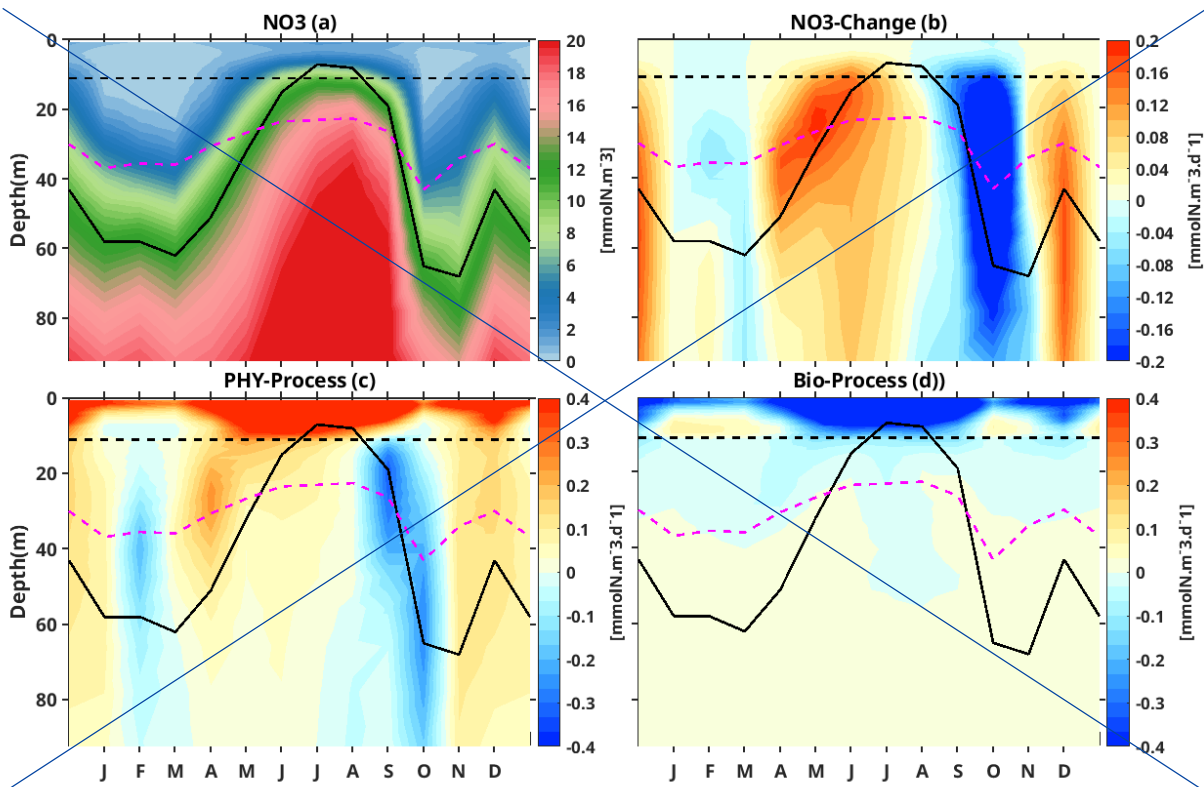
Figure 104: Contribution of (a) the horizontal processes, including (c) zonal advection and (e) meridional advection, and (b) vertical processes, including (d) vertical advection and (f) vertical diffusion, to the nitrate budget averaged in the mixed layer during the austral winter. Units are $\text{mmolN.m}^{-3}.\text{d}^{-1}$.

Zonal advection (Fig.123c) supplies nitrate in the euphotic layer, with a maximum above the mixed layer depth, throughout the year. This nitrate input is more than compensated by nitrate lost by meridional contribution, below the upper 5 m (Fig.123e), except in June, July and August. Vertical advection (Fig.123d) is the dominant vertical process (Fig.123b) in the nitrate budget. Below 30 m depth, it has a semi-annual cycle characteristic of upwelling and downwelling CTWs propagation, associated with nitrate increase when the thermocline shallows and nitrate decrease when the thermocline deepens, with the maximum and minimum values around the thermocline depth. Moreover, vertical advection supplies more nitrate in the mixed layer than in the euphotic layer below during the main upwelling period (June, July and August), but rather the opposite during the second upwelling period (December). Between the mixed layer depth and the euphotic layer depth, vertical diffusion (Fig.123f) tends to partially compensate for the effects of vertical advection on nitrate. However, in the mixed layer it mostly supplies nitrate, particularly during the upwelling seasons.

775



776



777

778

779

Figure 11: Depth-time Hovmöller diagram of the seasonal cycle of the nitrate budget averaged within the Congolese coastal box (0°S–6°S, 1° wide coastal band, as shown in Fig. 1). (a) Nitrate concentration

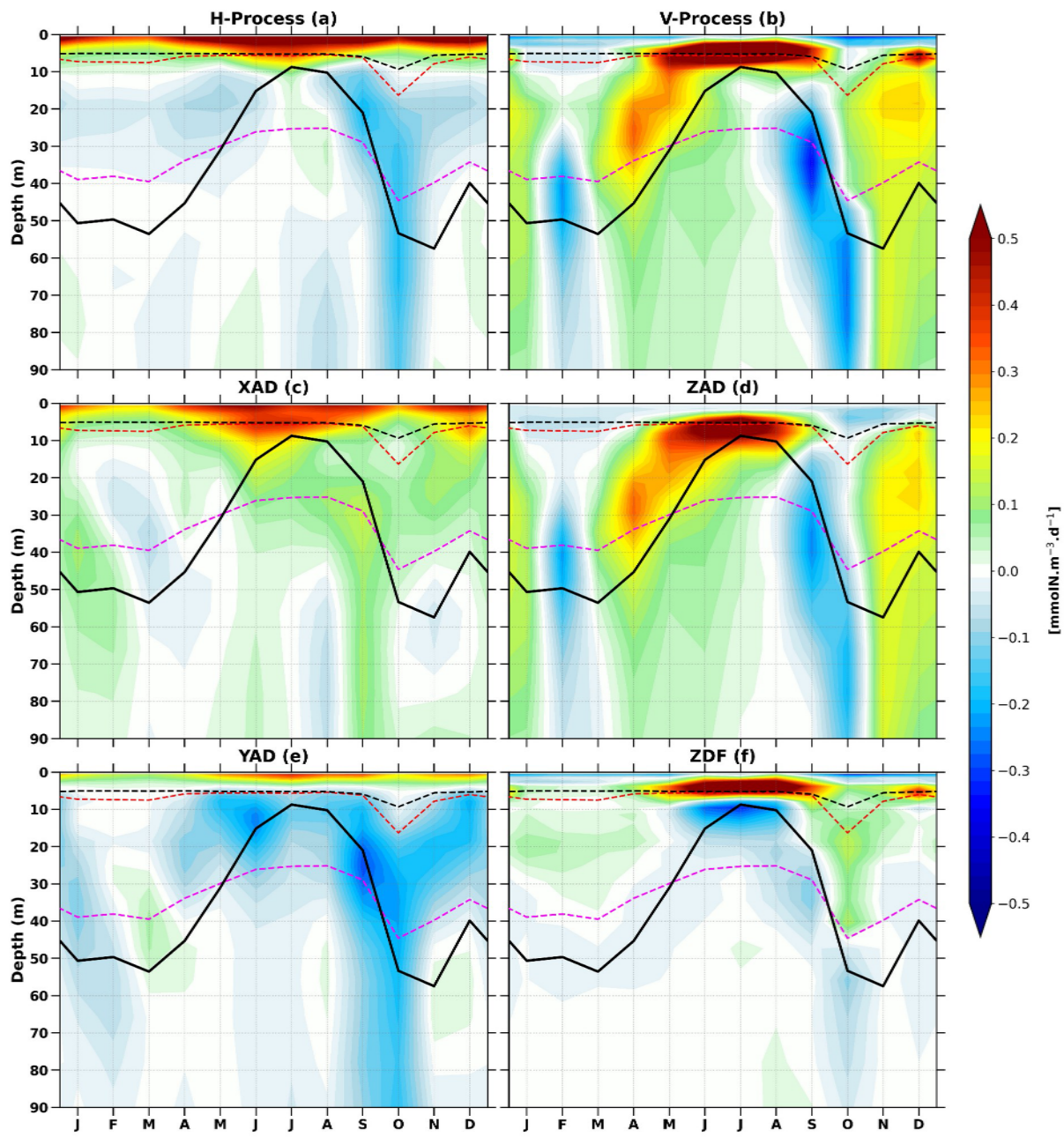
780 | **(mmolN.m⁻³), (b) nitrate rate of change, (c) physical process contribution, and (d) biological process**
781 | **contribution (mmolN.m⁻³.d⁻¹). The black solid line represents the thermocline (20°C isotherm), while dashed**
782 | **magenta, red and black lines indicate the euphotic, isothermal and mixed layer depths, respectively.** ~~Figure 12:~~
783 | ~~Depth-time Hovmöller diagram of the model seasonal cycle of nitrate concentration (a), nitrate tendency in the~~
784 | ~~euphotic layer (b) contributed by physical process (c) and biological processes (d) in the congolese coast coastal box~~
785 | ~~(Fig. 3). The units are in mmolN.m⁻³.d⁻¹ for all plots (b, c, d) except nitrate concentration (a) which is in~~
786 | ~~mmolN.m⁻³. The black line represents the thermocline. The dashed magenta and black lines are the euphotic layer~~
787 | ~~and mixed layer depths respectively.~~

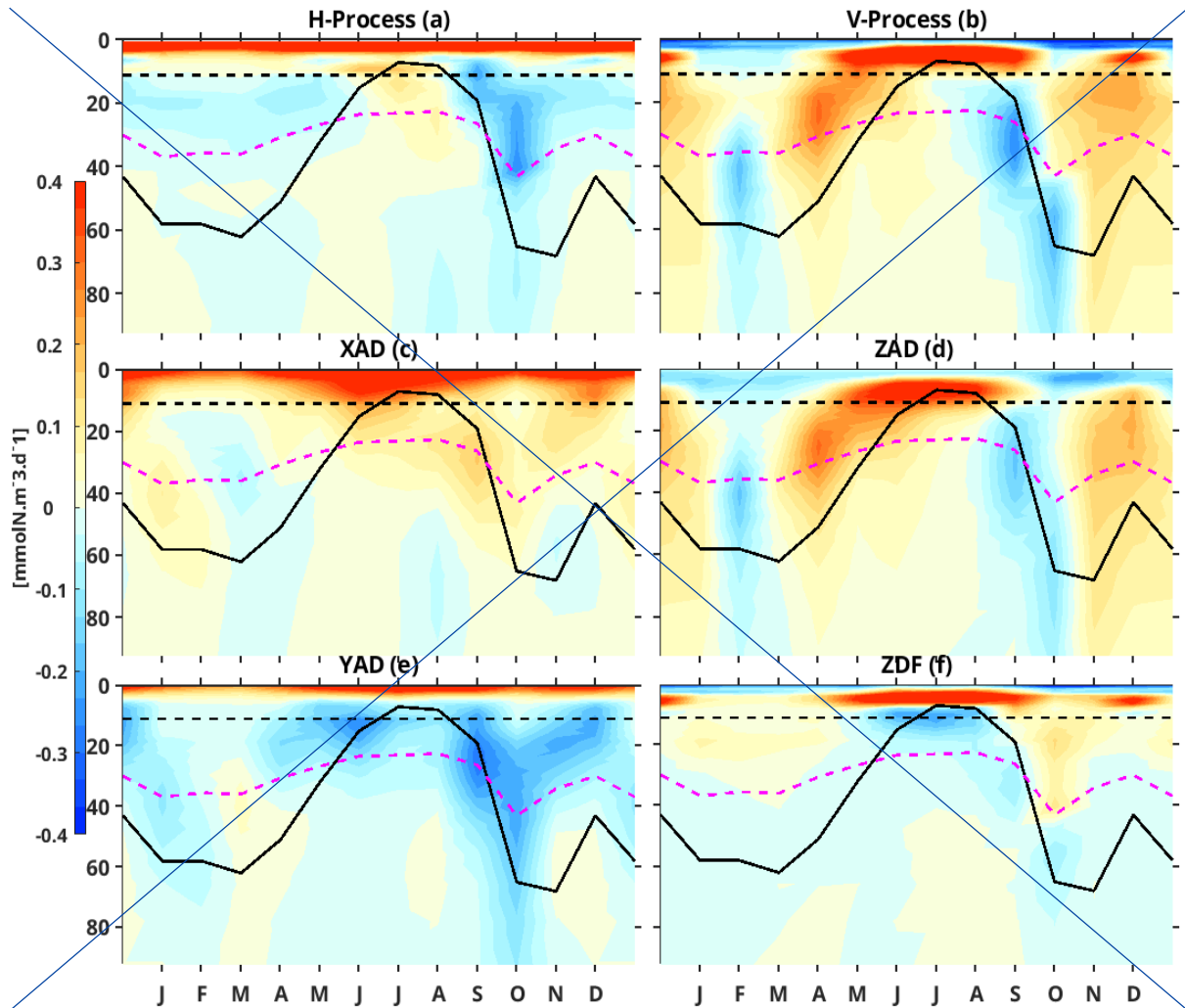
788 | **3.3.2 Nitrate budget analysis: advection components analysis**

789 | **As nitrate advection depends on velocity and on the nitrate gradient, we now evaluate the**
790 | **individual contributions of seasonal variations in velocity and nitrate gradient, as well as their**
791 | **combined effect, to the seasonal variations of nitrate advection (see section 2.3, equation 4).**

792 | **3.3.2.1 Nitrate budget analysis: horizontal advection**

793 | **Fig.13 are 14 allows to visually compare the depth-time structure of the zonal nitrate advection**
794 | **(Fig.13a) with that of its different components, while correlation r is used to quantify the**
795 | **comparison.**





797

798

799

800

801

802

803

804

805

806

807

808

809

810

811

812

Figure 123: Depth-time Hovmöller diagram of the model seasonal cycle of contributions to the nitrate budget of horizontal and vertical processes (a and b respectively), zonal, meridional, vertical advections (c, e and d respectively), vertical diffusion (f) along the Congolese coast (03°S-6°S and 1° width to the coast). Units are mmolN.m^{-3} for all of the plots. The black solid line represents the thermocline (20°C isotherm), while dashed magenta, red and black lines indicate the euphotic, isothermal and mixed layer depths, respectively. The strong black line represents seasonal variation of the thermocline, the dashed magenta line is the euphotic layer and dashed black line is the mixed layer depth.

The seasonal cycle of zonal nitrate advection The zonal nitrate advection seasonal cycle in the 0-100 m

water column (Fig. 134a) is controlled first by the term $\overline{v} \left(\frac{\partial \overline{N}}{\partial x} \right) - \overline{v \frac{\partial N}{\partial x}}$ (Fig.134e, $r=0,77$, $p<0.05$), i.e.

the annual mean zonal current multiplied by the seasonal variations of the nitrate zonal gradient,

second by the term $\overline{v} \left(\frac{\partial \overline{N}}{\partial x} \right) - \overline{v \frac{\partial N}{\partial x}}$, (Fig.134d, $r=0,49$, $p<0.05$), i.e. the seasonal variations of the zonal

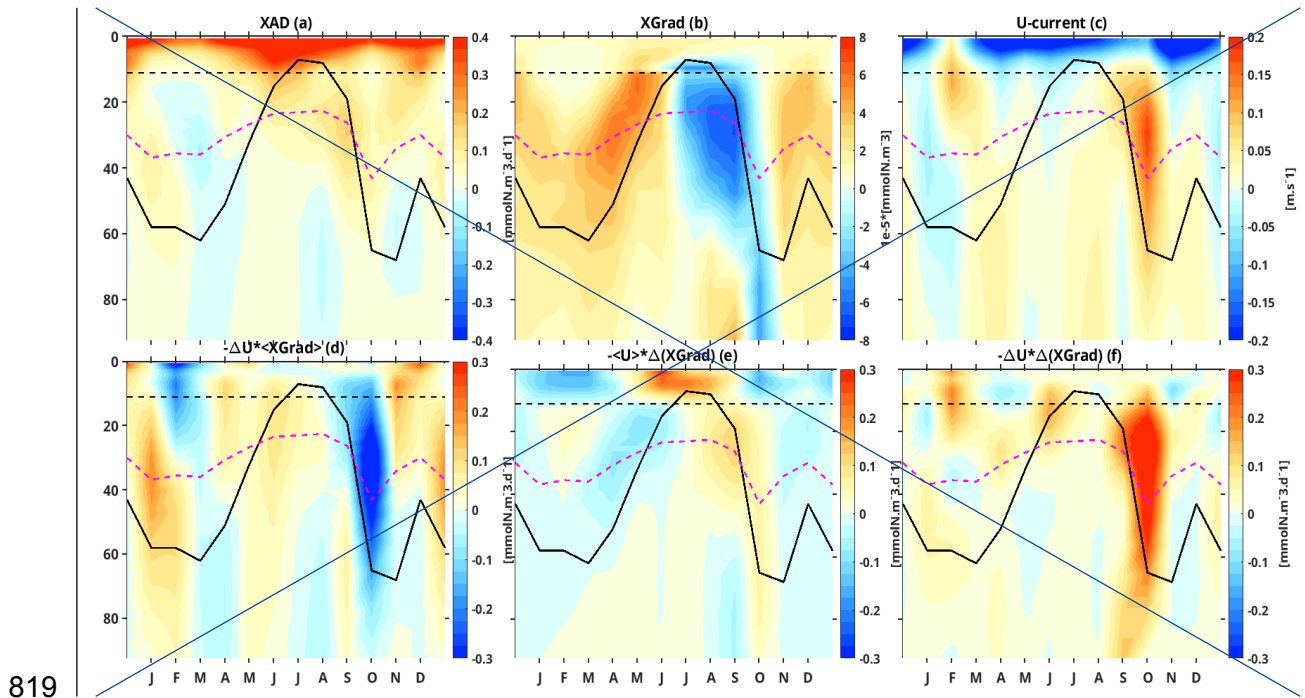
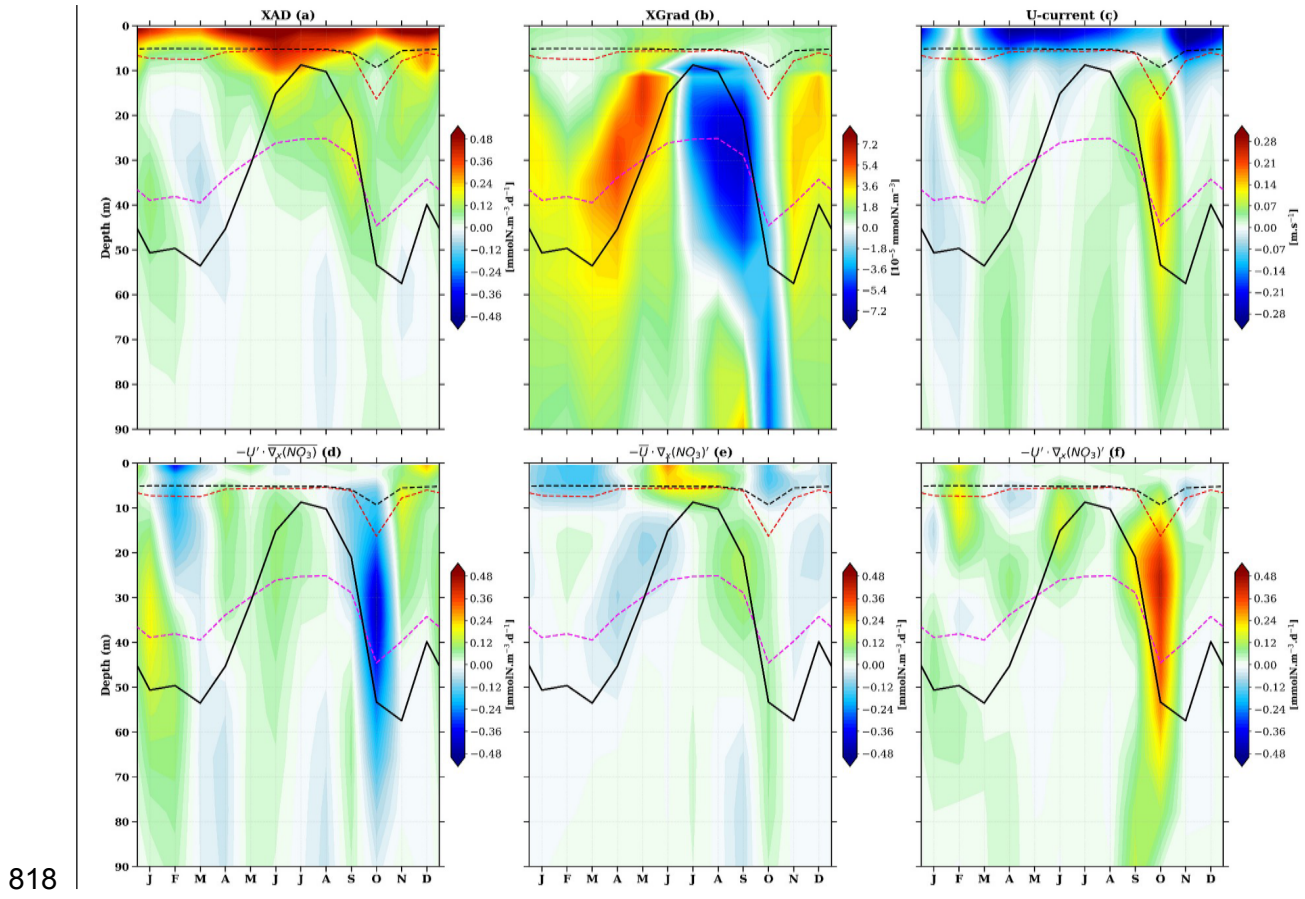
current multiplied by the annual mean nitrate zonal gradient, and third (and much less) by the

term. The third component, which represents the simultaneous variation in zonal current and

nitrate gradient $\overline{v \left(\frac{\partial N}{\partial x} \right) - \left(\frac{\partial \overline{v N}}{\partial x} \right)}$, (Fig.134f, $r=-0,15$, $p<0.05$), i.e. the product of seasonal variations of

both the zonal current and the nitrate zonal gradient. The seasonality of the zonal current (Fig.

813 134c) is influenced by the seasonal cycle of the South Equatorial Undercurrent SEUC, with
 814 maximum values in September-October and February-March (Dorothee et al, 2004) in this zone
 815 (3°S - 6°S , 1° from the coast). Thus we can conclude that the SEUC plays a key role in the nitrate
 816 balance in the Congolese system by bringing nitrate in February-March and in September-
 817 October to the euphotic layer.



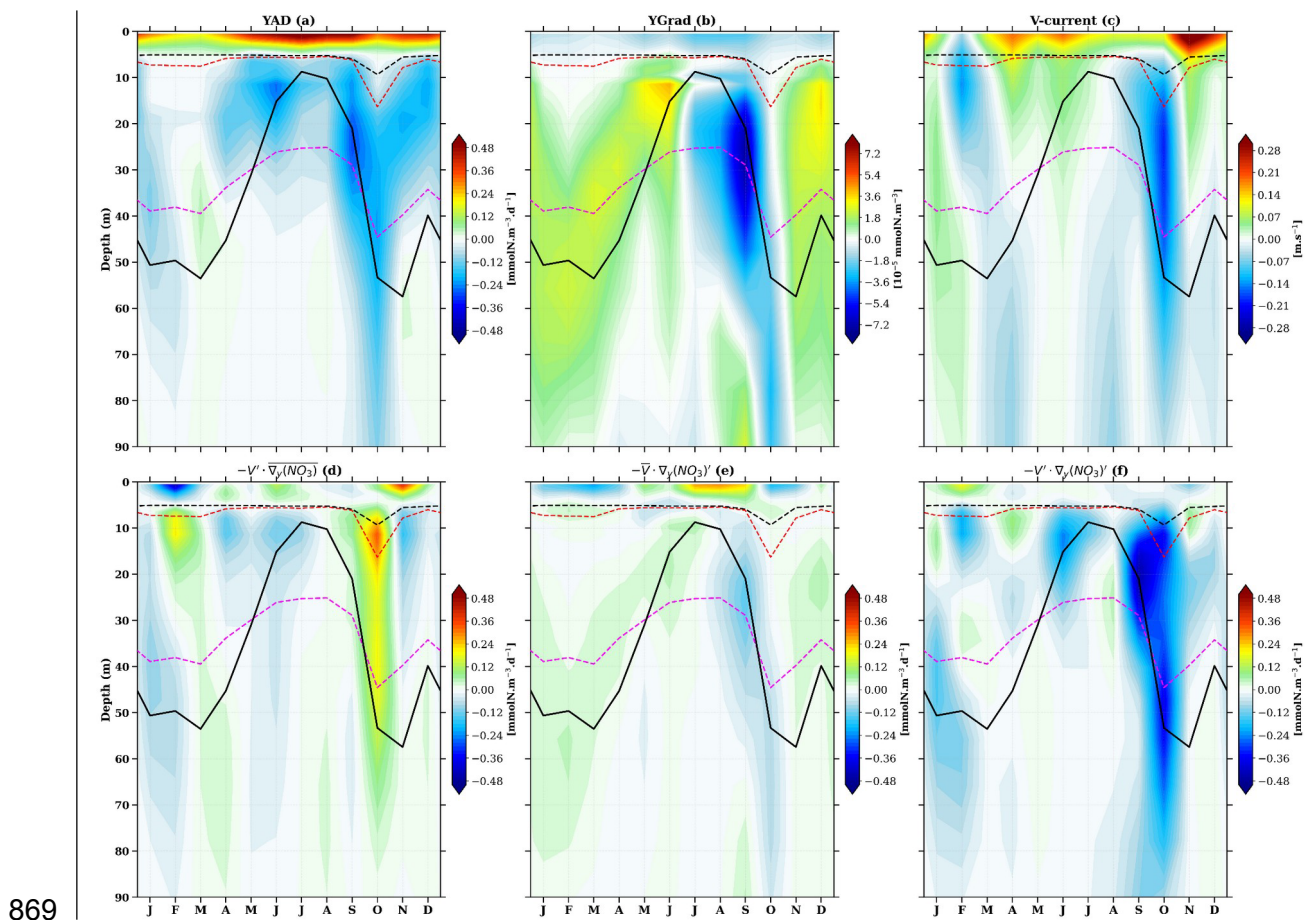
820 Figure 134: Depth-time Hovmöller diagram of the model seasonal cycle of nitrate advection (a), nitrate
 821 gradient (b), zonal current (c), zonal current variation times mean nitrate gradient (d), gradient variation
 822 times mean current (e) and gradient variation times zonal current variation (f), all along the zonal axis in the
 823 congolese coastal box of Fig. 13. Units are milli mol per cubic meter per day for all of the plots except (b)
 824 (milli mol per cubic meter) and (c) (meter per second). The black solid line represents the thermocline (20°C
 825 isotherm), while dashed magenta, red and black lines indicate the euphotic, isothermal and mixed layer
 826 depths, respectively. The full black line represents the thermocline, the dashed magenta line is the euphotic
 827 layer depth and the dashed black line is the mixed layer depth.

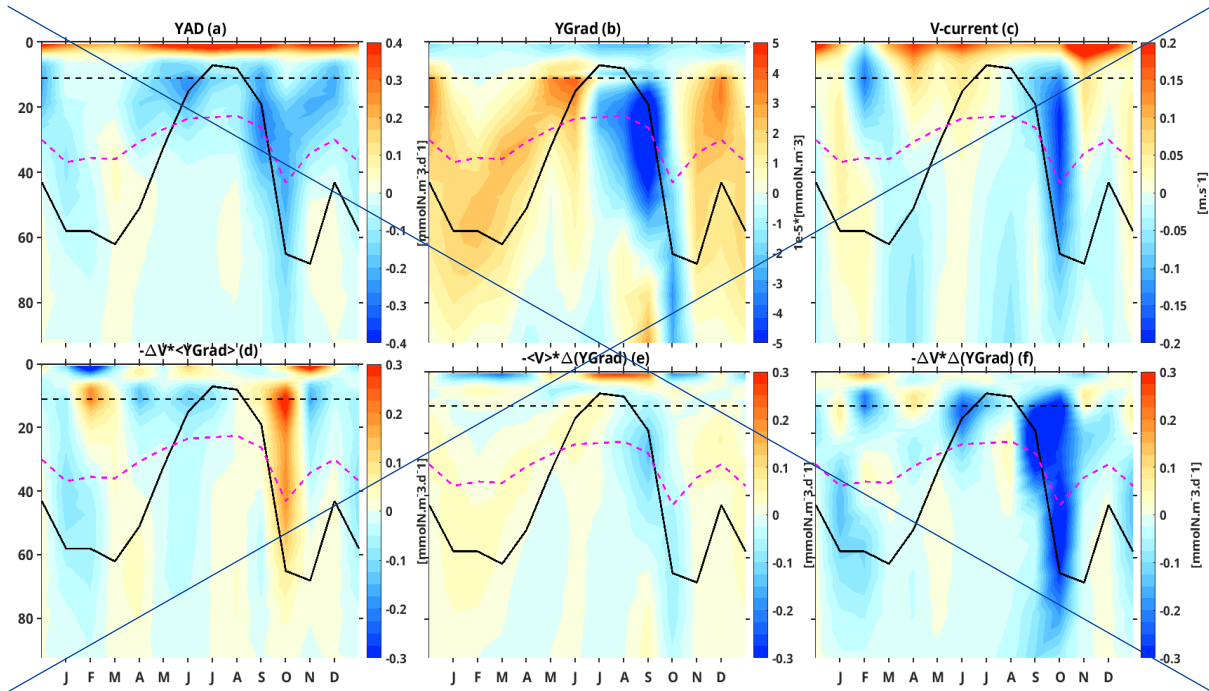
828 In the euphotic layer, we see that, as for the meridional nitrate advection, the meridional current
 829 (Fig.145c) looking at the shape seems to be the main factor in the vertical and temporal variation
 830 shape of the meridional nitrate advection (Fig.145a). The Angola current (AC), is the factor which
 831 modulates nitrate lost by meridional nitrate advection throughout the year, with maximum loss in
 832 September-October and June-July, in and below the euphotic layer, except In the first 5 m-depth.
 833 Our analysis in this section reveals that the simultaneous variation in both the meridional current
 834 and the gradient $(\overline{v} \frac{\partial \sigma}{\partial z})$, Fig.145f) exhibits the highest correlation ($r=0.527$, $p<0.05\%$) with
 835 meridional nitrate advection, thus explaining the major changes in advection. This result
 836 highlights the significant impact of the concurrent variability of both meridional current and
 837 gradient on meridional nitrate advection in the euphotic layer. In contrast, gradient variation ($\frac{\partial \sigma}{\partial z}$, Fig.145e) is poorly correlated ($r=0.97$, $p<0.05\%$) with meridional nitrate advection.
 838 The very low positive correlation with total meridional advection (a) indicates this term,
 839 representing the effect of a mean meridional current acting on a fluctuating nitrate gradient. This
 840 suggests that either the mean meridional current is weak, or its interaction with the fluctuating
 841 gradient does not lead to significant changes in overall advection. The variation in the meridional
 842 current (\overline{v}) , Fig.145d) shows the lowest correlation ($r=0.287$, $p<0.05-28.7\%$). This low,
 843 negative correlation with total meridional advection (Fig.145a) indicates that this term,
 844 representing the effect of fluctuating meridional currents on a relatively stable mean nitrate
 845 gradient, is not a dominant driver of the overall meridional nitrate advection. In fact, a negative
 846 correlation suggests it might weakly oppose the main advection pattern or have an inverse
 847 relationship. This implies that the mean gradient is either small or the meridional current
 848 variations are not aligned to produce significant advection changes via this mechanism.
 849

850 3.3.2.2 Nitrate budget analysis: vertical processes

851 Our analysis reveals that within the euphotic layer, the variation in the vertical gradient
 852 $(\frac{\partial \sigma}{\partial z})$, Fig.156e) appears to better explain the variation in vertical nitrate advection
 853 (Fig.156a), showing a correlation of $r=0.79$ ($p<0.05$)79%. In contrast, vertical velocity variation (v)

854 $\overline{v' \cdot \nabla_y' (NO_3)'}_t$, Fig.156d) plays a secondary role, with a correlation of approximately 0.64-6 ($p < 0.05$)%
 855 with vertical nitrate advection. Looking now at the vertical nitrate advection, we can see strong
 856 similarities in the vertical and temporal variation structure—between vertical advection
 857 seasonality (Fig.156a), vertical nitrate gradient seasonality (Fig.156b) and vertical velocity
 858 seasonality (Fig.156c), both three are very strong in the euphotic layer. We can also see in the semi-
 859 annual vertical velocity that from April to August and November-December, vertical velocities are
 860 upward corresponding to negative values of SLA (Fig.45a, 45b), lowest SST (Fig.45c, 45d) values
 861 and highest nitrate concentration (Fig.45e, 45f). From January to March and September-October,
 862 vertical velocities are downward corresponding to positive values of SLA (Fig.45a, 45b), highest
 863 SST (Fig.45c, 45d) values and lowest nitrate concentration (Fig.45e, 45f). This later observation
 864 confirms that CTWs propagating from April to August and November-December are associated
 865 with upwelling. In contrast, CTWs propagating from January to March and September-October
 866 are associated with downwelling. Note that similar results were found by Ngakala et al. (2025) for
 867 the seasonal heat budget in the Congolese upwelling (from 4°S-6°S and 1° width to the coast) and
 868 also further south in the Angolan upwelling by Korner et al. (2024).





870

871

872

873

874

875

876

877

878

Figure 145: Depth-time Hovmöller diagram of the model seasonal cycle of nitrate advection (a), nitrate gradient (b), meridional current (c), meridional current variation times mean nitrate gradient (d), gradient variation times mean meridional current (e) and gradient variation times current variation (f), all along the meridional axis in the congolese coastal box of Fig. 1b3. Units are milli mol per cubic meter per day for all of the plots except (b) (milli mol per cubic meter) and (c) (meter per second). The black solid line represents the thermocline (20°C isotherm), while dashed magenta, red and black lines indicate the euphotic, isothermal and mixed layer depths, respectively. The full black line represents the thermocline, the dashed magenta line is the euphotic layer depth and the dashed black line is the mixed layer depth.

879

880

881

882

883

884

885

886

887

888

889

890

891

892

However, if we average in consider the first hundred meters, vertical velocity variation has the highest correlation of -0.831 ($p < 0.05$) 83.1% with vertical advection, whereas vertical gradient variation has only 0.63 ($p < 0.05$) 63% of correlation with vertical advection. The third component ($\frac{\Delta V}{\Delta Y} \Delta Y$, Fig.156f) has a lower negative correlation -0.062 ($p < 0.05$) 6.2% with vertical advection. During the upwelling period, the variation in vertical gradient (Fig.156e) at the base of the mixed layer has a much greater influence on nitrate supply than the variation in vertical velocity (Fig.156e). Another observation is that in the same main upwelling period there is a lag between maximum vertical current which happens in May and the maximum vertical gradient indicated by the shallowest thermocline in July. This lag results in a highest input of nitrate by vertical advection (Fig.156a) in the mixed layer in June. It can be seen that the nitrate output by vertical advection during the downwelling period is mostly induced by the vertical nitrate gradient in the mixed layer whereas deeper in the euphotic layer these losses are induced by vertical downward velocities induced by downwelling CTWs propagation.

4 Discussion

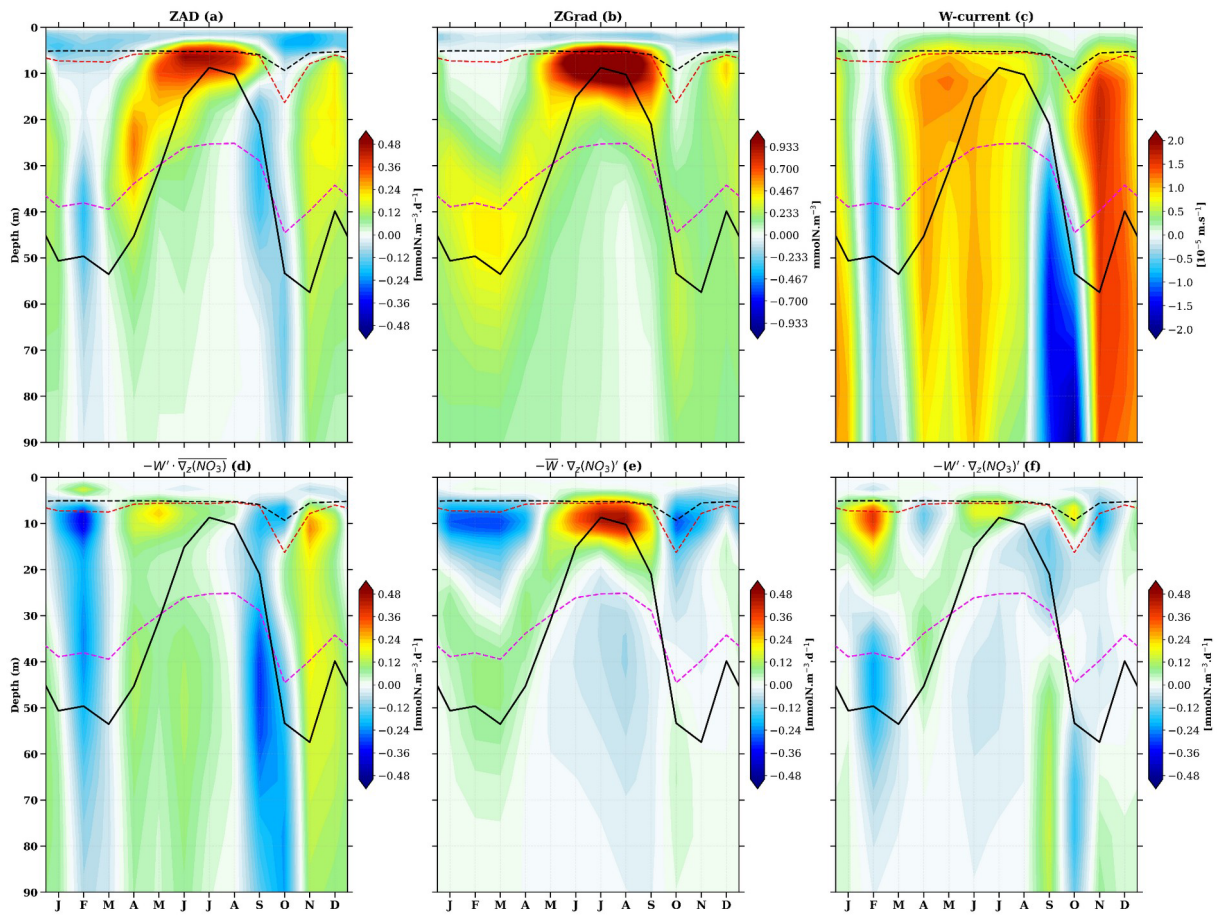
893 In this section, we discuss our results: the model-data comparison, the influence of the mixed layer
894 criteria, the main nitrate budget drivers in the Congolese upwelling system compared to the other tropical
895 Atlantic upwelling systems~~In this section, we discuss our results: the model-data comparison, the~~
896 ~~influence of the mixed layer criteria, the main nitrate budget driver in the Congolese upwelling systems~~
897 ~~compared to the other tropical Atlantic upwelling systems.~~ **Finally, we will explore the factors**
898 **governing seasonal productivity in the Congolese upwelling system, integrating our**
899 **understanding of physical forcing and nutrient availability to characterize its biological response.**
900 **Through this comprehensive discussion, we aim to provide a nuanced understanding of the**
901 **oceanographic processes at play in the coastal Congo region and the capabilities and limitations of**
902 **our modeling approach.**

903 **Throughout this work, we have shown that our model reasonably reproduces the observations in**
904 **terms of temperature, nitrate, CHL_a, SLA and surface currents, although there are a few**
905 **differences that we will discuss in this section. First of all, we saw that temperature in our model is**
906 **warmer**~~greater~~ **than observed by around 1°C in regional distribution (Fig. 2a,b) as well as in seasonal**
907 **cycles (Fig. 4c,d)**~~1°C in regional distribution as well as in seasonal cycles.~~ **This is a common bias in**
908 **ocean and climate models in the Eastern tropical Atlantic (Richter, 2015; Zuidema et al., 2016;**
909 **Voltaire et al., 2019).** ~~Indeed, several studies suggest that this warm bias is multicausal. While it is~~
910 ~~partly attributed to models' deficiency in simulating low-level clouds, resulting in overestimation of~~
911 ~~shortwave radiation (Xu et al., 2014), other factors play a critical role. These include errors in~~
912 ~~atmospheric forcing, specifically the misrepresentation of the coastal low-level jet and wind stress,~~
913 ~~which can weaken coastal upwelling (Cabos et al., 2017; Voltaire et al., 2019). Furthermore, complex~~
914 ~~air-sea feedback mechanisms (Koseki et al., 2018) and difficulties in simulating the vertical thermocline~~
915 ~~structure in the region (Koubanova et al., 2018) are also shared challenges that contribute to this~~
916 **persistent modeling bias.** ~~This is a common bias in ocean and climate models in the Eastern tropical~~
917 ~~Atlantic. Indeed, several studies suggest that this warm bias is due to models' deficiency in simulating~~
918 ~~low-level clouds, resulting in overestimation of shortwave radiation (e.g. Xu et al., 2014).~~

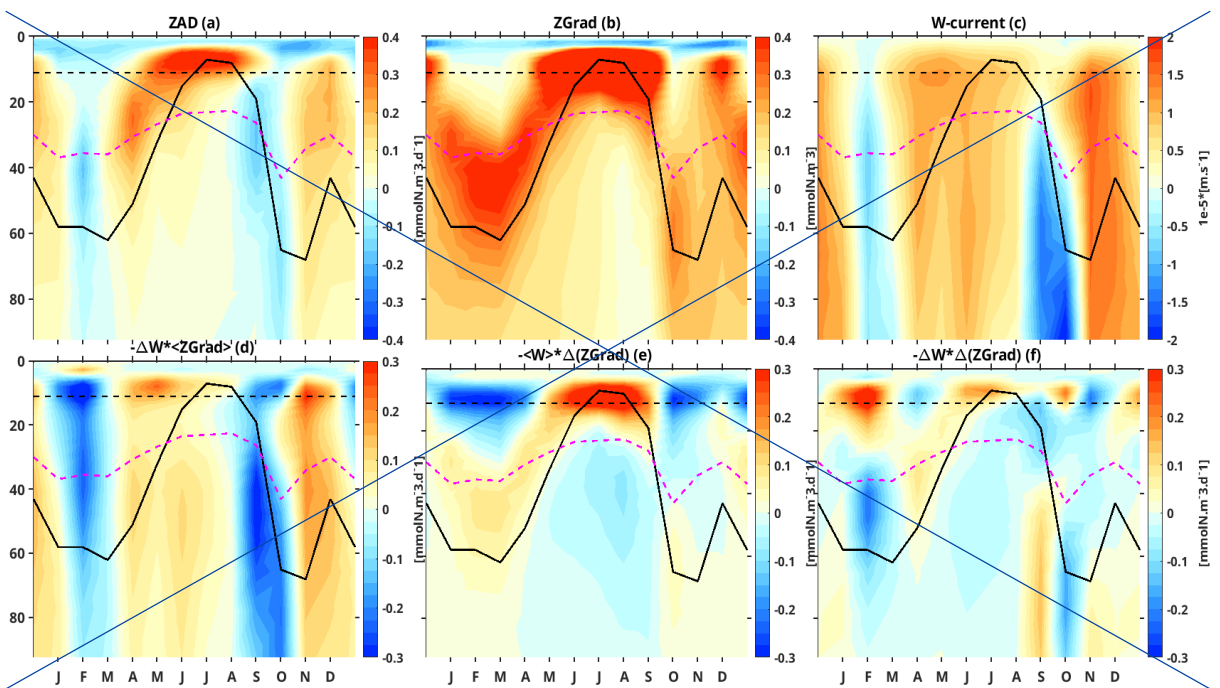
919 |

920 |

921 |



922



923

924 **Figure 156:** Depth-time Hovmöller diagram of the model seasonal cycle of nitrate advection (a), nitrate
 925 **gradient (b), vertical current (c), vertical current variation times mean nitrate gradient (d), gradient**
 926 **variation times mean vertical current (e) and gradient variation times current variation (f), all along the**
 927 **vertical axis in the congolese coastal box of Fig. 1b3. Units are milli mol per cubic meter per day for all of the**
 928 **plots except (b) (milli mol per cubic meter) and (c) (meter per second). The black solid line represents the**

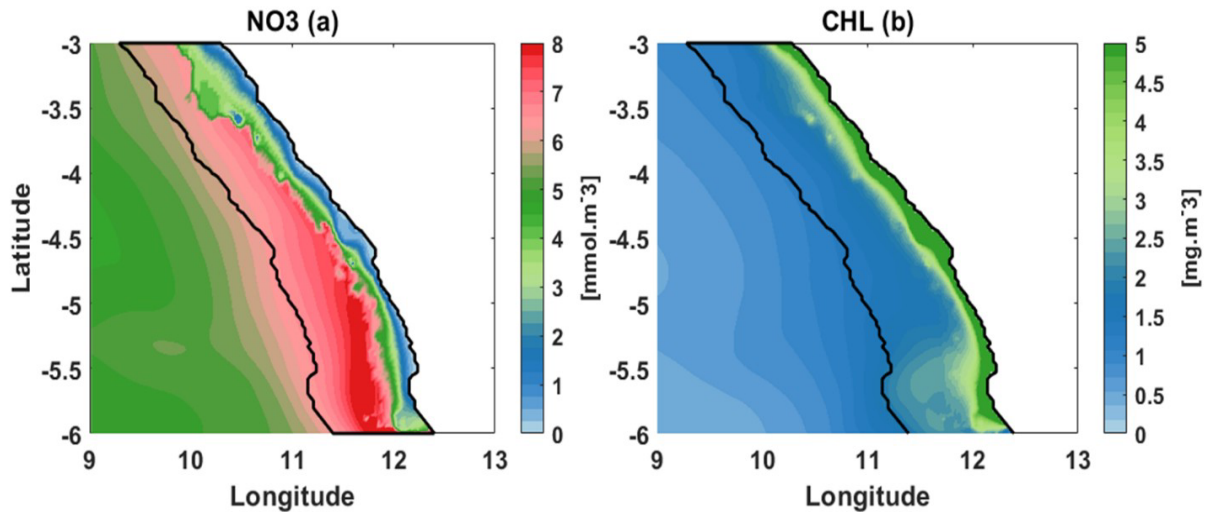
929 | thermocline (20°C isotherm), while dashed magenta, red and black lines indicate the euphotic, isothermal and
930 | mixed layer depths, respectively. The full black line represents the thermocline, the dashed magenta line is the
931 | euphotic layer depth and the dashed black line is the mixed layer depth

932 | With regard to nitrate concentrations, the regional distribution shows that north of the mouth of
933 | the Congo River and near the coast, the model agrees well with CARS climatology (Fig. 2c,d). On
934 | the other hand, offshore and south of the mouth of the Congo River, the model underestimates nitrate
935 | concentrations~~With regard to nitrate concentrations, the regional distribution shows that north of the~~
936 | ~~mouth of the Congo River and near the coast, the model agrees well with CARS climatology. But~~
937 | ~~offshore and south of the mouth of the Congo River, the model underestimates nitrate concentrations.~~
938 | ~~Similarly, in the seasonal cycle, we see that the model captures the seasonal variability, but~~
939 | ~~underestimates the amplitude compared to the data. These biases may be explained by the~~
940 | ~~temporal coverage of the CARS climatology, which covers a long period (from 1940 to 2011) of~~
941 | ~~data (Bachelery et al., 2016) compared to our model which covers only one year (2011). Another~~
942 | ~~bias may be the lack of data in CARS, in our study area. We did not show the comparison of our~~
943 | ~~model with the WOA climatology due to its low resolution (1°) for nutrients and oxygen in our coastal~~
944 | ~~studied area compared to CARS climatology (0.5°). However the biases with WOA are similar as with~~
945 | ~~CARS even if WOA covers a more recent period (from 2005 to 2017). The data coverage and individuals~~
946 | ~~data profiles are also available for WOA, confirming that very few data are available in our studied area.~~
947 | **The differences in the surface CHLa concentration between the model and the satellite**
948 | **observations may be associated with a lack of data for the ocean colour satellite observations,**
949 | **particularly in August, due to the cloud cover which induces atmospheric contaminations**
950 | **(Hardman-Mountford and McGlade., 2002; Estival et al., 2013) of the satellite signal, resulting in**
951 | **a lack of CHLa signal (Nieto et al., 2016). The biases in the surface currents between the model and the**
952 | **observations are mainly due to the underestimation of the currents in the OSCAR product near the**
953 | **coastal zone**~~The biases in the surface currents between the model and the observations are mainly due to~~
954 | ~~the under-estimation of the currents in the OSCAR product near the coastal zone (Sikhakolli et al.,~~
955 | ~~2013), especially in our studied area where very few data are available. Despite these results~~
956 | ~~discussed earlier in this paper, we have to keep in mind that there are also some limitations in our~~
957 | ~~simulation. For example, the model has difficulties reproducing the seasonal cycle of CHLa~~
958 | ~~concentration, in particular the first CHLa blooms occurring in February-March, highlighted by~~
959 | ~~the MODIS ocean colour satellite data. This might be due to the CHLa concentration of the Congo~~
960 | ~~river in our model. Indeed, we take into account the nutrients and dissolved organic matter~~
961 | ~~discharges of the river but not the CHLa concentrations (information not available in the HYBAM~~
962 | ~~database). We can also observe a minimal or slightly reduced concentration of CHLa around the~~
963 | ~~mouth of the Congo River in our model (Fig. 2e). This is explained by the very high speed (greater~~
964 | ~~than 2 m/s) of the Congo River current at its mouth in our model. This has resulted in the transport~~

965 of CHLa chlorophyll produced by phytoplankton photosynthesis away from the mouth of the
966 Congo River.

967 Our analysis shows that, in the Congolese upwelling system, the nitrate budget in the mixed layer is
968 dominated by physical processes during the upwelling period (**Fig. 7c**), particularly vertical diffusion
969 (**Fig. 8f**). Our analysis shows that, in the Congolese upwelling system, the nitrate budget in the mixed
970 layer is dominated by the physical processes during the upwelling period, particularly vertical advection,
971 while zonal advection and vertical mixing play a secondary role. In agreement contrast to these latter
972 results, Ngakala et al. (2025) using a high resolution simulation (1/36°) of NEMO in the Congolese
973 upwelling, have shown through a mixed layer heat budget, that vertical diffusion was the main
974 contributor of cooling during upwelling period in the mixed layer. They found that the vertical
975 advection has a secondary role in cooling of the mixed layer. These differences can be associated with
976 the definition criterion of the mixed layer depth, which is very shallow in their analysis (0.2 °C
977 temperature criterion from 0.5 m depth as reference depth of density variation). They state that, if
978 defining instead the mixed layer depth with the de Boyer-Montégut criterion, as we do, then
979 vertical advection would play a greater role than vertical diffusion, as we find in our nitrate budget.
980 Thus, as mentioned in our study and in agreement with Ngakala et al. (2025), the relative
981 contributions of vertical advection and diffusion depend on the definition of the mixed layer depth.
982 Our analysis reveals that the seasonal variability of CHLa in our region is driven by the seasonal
983 concentration of nitrate, as in other tropical Atlantic upwelling systems (Radenac et al., 2020).
984 However different processes drive the seasonal cycle of nitrate and CHLa in the different tropical
985 Atlantic upwelling systems. In the Equatorial Atlantic upwelling system, the seasonal cycle of
986 nitrate and CHLa are driven by the wind stress and wind stress curl (Caniaux et al., 2011, Radenac
987 et al., 2020). In the Tropical Angola Upwelling system, the main driver of these seasonal cycle are
988 the CTWs as in our area with a main peak in austral winter (May-July) and a second peak in
989 December-January. However vertical mixing plays also a key role in the Tropical Angola
990 Upwelling system (Awo et al., 2022; Ostrowski et al., 2009; Körner et al., 2023) due to onshore
991 propagating internal tide waves interacting with sloping topography (Brandt et al., 2023). In the
992 upwelling systems of the equatorial Atlantic and tropical Angola, vertical mixing is the main
993 driver of nitrate input to the mixed layer. This is due to local mechanisms that occur in these areas
994 (local forcing), such as the intensification of the vertical shear stress between the South Equatorial
995 Current (SEC) and the Equatorial Undercurrent (EUC) at the equator (Jouanno., 2010, Radenac
996 et al., 2020) and the dissipation of internal tide that interact with the continental shelf and produce
997 turbulent mixing at the Angolan coast (Körner et al., 2023, Zeng et al., 2021, Brandt et al.,
998 2023 Brandt et al.). In the Congolese system, we can suggest that the strong stratification induced by
999 the discharge of the Congo River, which is the second largest river in the world, contributes to
1000 thinning the mixed layer, limiting the effect of mixing very close to the surface (Dossa et al., 2019).

1001 In the euphotic layer and below, the nitrate budget is almostly dictated by physical processes,
1002 which are mainly modulated by currents that transport water of different properties. ~~In this~~
1003 ~~section, we will discuss the influence of currents on the nitrate and CHLa balance in the euphotic layer.~~
1004 We noted that vertical and zonal advections were the drivers of nitrate input in the upwelling
1005 period, while vertical mixing and meridional advection were the drivers of nitrate losses in the
1006 lower part of the euphotic layer (just below the mixed layer depth) in this period. However, during
1007 the downwelling period, vertical mixing mostly brings nitrate to the lower part of the euphotic
1008 layer, while vertical and meridional advection always remove nitrate. Meridional advection is
1009 therefore the main factor in nitrate loss in the euphotic layer all year long. This is consistent with
1010 the warming effect of meridional advection shown by Körner et al. (2023) in the Angolan
1011 upwelling. Radenac et al (2020) showed that in the equatorial euphotic layer, zonal advection by
1012 the EUC current was the main driver of nitrate losses, which may explain our previous results
1013 since the southward Angola current dominating the ocean circulation in the Congo-Angola zone is
1014 fed by the EUC current. Indeed, the EUC, whose source waters come from the oligotrophic layers
1015 of the subtropical South Atlantic, has relatively low nitrate concentrations compared to
1016 neighbouring waters (Schott et al., 1998; Johns et al., 2014; Tuchen et al., 2022a). These low
1017 nitrate waters are brought to the Congo-Angola system by the Angola Current (AC) (Fig.16),
1018 reducing nitrate concentration in the euphotic layer. At the same time, the AC brings CHLa into
1019 the euphotic layer by meridional advection, as the EUC has relatively high CHLa concentrations
1020 (Radenac et al., 2020). This low nitrate / high CHLa signature of the AC can be seen in the first
1021 hundred metres and in particular at the base of the euphotic layer along the Congolese coast
1022 (Fig.A1c), where the AC flows (Kopte et al, 2017). Further analyses show that the coastal CHLa
1023 maximum occurs from May to September with a peak in August, which is consistent with the
1024 seasonal cycle of the CHLa concentration in the EUC (Radenac et al, 2020; Brandt et al, 2023). The
1025 simultaneous variation in current and gradient appears to be the main factor contributing to
1026 variations in the meridional advection and nitrate removal, mainly between July and October.
1027 Over the same period, we observe a sign change of the meridional nitrate gradient (Fig.15b),
1028 which is generally positive (indicating that under the mixed layer, waters to the south of the ~~box~~
1029 coastal box (0°N–6°S, 1° width from the coast; see Fig. 1b) are less nitrate-rich than waters to the
1030 north) under the mixed layer from January to June.



1031

1032 **Figure 167: Regional distribution of mean annual nitrate and CHLa concentration (a, b respectively)**
 1033 **averaged on the 0-100 m layer along the Congolese upwelling area, black line represents different**
 1034 **boundaries of our Coastal box with a width of 1° of longitude relative to the coast.**

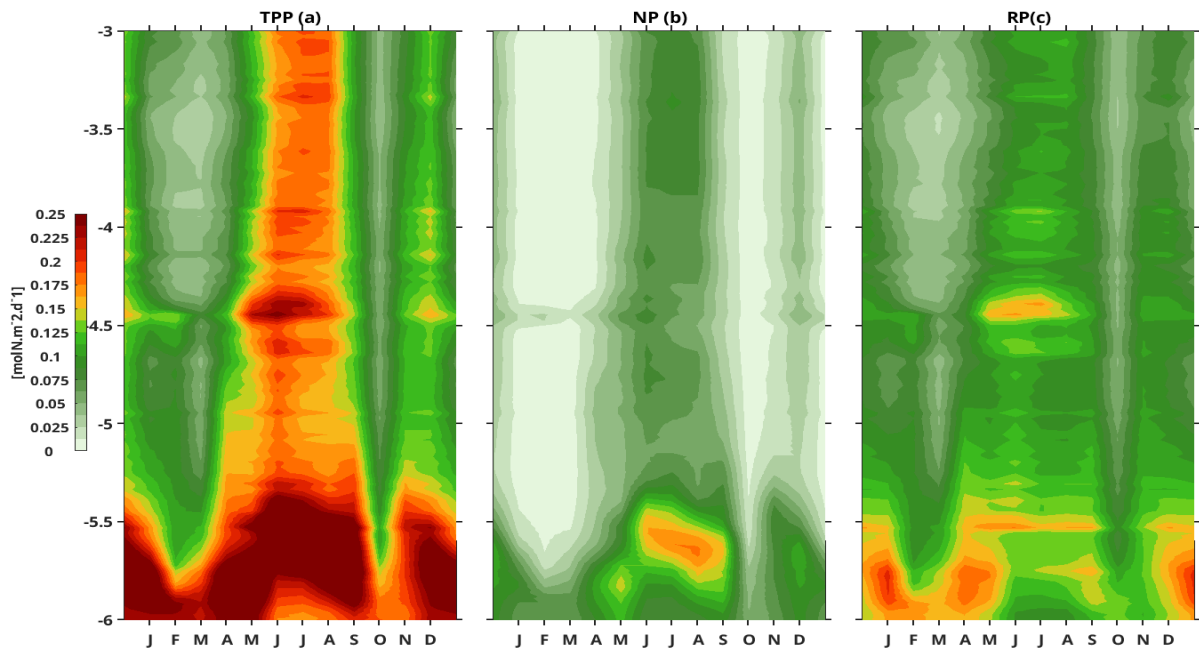
1035 **This observation suggests that for the period from September to October, waters in the southern**
 1036 **part of the box are now richer in nitrate than waters in the northern part of the box under the**
 1037 **mixed layer. Beyond horizontal transport, this frontogenesis is also driven by the meridional**
 1038 **gradient of vertical motion ($\partial w/\partial y$). A stronger upward vertical velocity in the southern section**
 1039 **(near 6°S) compared to the north leads to a higher vertical nitrate supply in the south, establishing**
 1040 **the negative meridional nitrate gradient observed in Fig. 14b. This highlights the important role of**
 1041 **vertical processes in the regional enrichment, as also emphasized by Nubi et al. (2016) for the**
 1042 **equatorial band. This also reflects the passage of low-nitrate waters from the EUC via the Angola**
 1043 **Current to the Congolese coast. However, we find that zonal advection brings nitrate in the**
 1044 **euphotic layer and its decomposition has shown that its variation is mostly influenced by zonal**
 1045 **nitrate gradient variation, with a secondary contribution of zonal current variation. This zonal**
 1046 **current variation is seen to remove nitrate in the euphotic layer during February-March and July-**
 1047 **October. We can also see that in these periods the zonal current flows toward the coast, which**
 1048 **suggests that it brings low nitrate water from offshore toward the coast. This seasonally eastward**
 1049 **current is consistent with the seasonal cycle of SEUC (Siegfried et al., 2019; Assene et al., 2022).**
 1050 **Besides this, we can also see that there is a sign change of the zonal nitrate gradient (Fig.134b)**
 1051 **which occurs simultaneously with the sign change of the meridional nitrate gradient (Fig.145b)**
 1052 **suggesting that this inversion in zonal nitrate gradient is due to Angola C_ecurrent water at the**
 1053 **coast. In fact, this later result highlights that the Angola current waters flowing along the coast are**
 1054 **less rich in nitrate than the water brought from offshore toward ~~to ward~~ the coast by the SEUC. As**
 1055 **nitrate concentration in the coast is lower, SEUC waters act to increase nitrate concentration in**
 1056 **our coastal box, through zonal advection in the euphotic layer from April to December. The CHLa**
 1057 **budget analysis (Appendix A, Fig. A1) shows that the SEUC brings through zonal advection low CHLa**
 1058 **water at the coast ~~The CHLa budget analysis (Appendix A) shows that the SEUC brings through zonal~~**

1059 ~~advection low CHLa water at the coast~~ **thereby reducing the nitrate input during the downwelling**
1060 **period. In the nitrate budget we saw that the main driver of nitrate input was vertical advection**
1061 **associated with CTWs. Körner et al. (2024) have shown, using satellite and mooring data, that**
1062 **CTWs detected in the SLA are of the low vertical mode, while the movement of the isopycnals is**
1063 **rather consistent with the vertical velocity structure of higher modes. This explains why isopycnals**
1064 **reach their seasonal minimum/maximum depth (in phase with the nitracline) after the minimum**
1065 **in SLA (Körner et al, 2024). The spatial distribution of mean annual nitrate and CHLa concentrations**
1066 **(Fig. 16a, b) provides clear evidence of the influence of the Angola Current (AC) on the coastal**
1067 **biogeochemistry of the Congolese system. Physically, the AC is a southward-flowing coastal current**
1068 **that advects warm, equatorial-origin waters along the shelf. Biogeochemically, our model results (Fig.**
1069 **16a) show that while the broader coastal box is enriched in nutrients due to upwelling and riverine inputs,**
1070 **there is a distinct relative decrease in nitrate concentrations strictly along the shoreline, particularly south**
1071 **of 5°S. In this narrow coastal band, NO₃ values are lower than those found in the core of the upwelling**
1072 **plume located slightly further offshore. Conversely, the chlorophyll-a map (Fig. 16b) reveals a robust**
1073 **coastal belt with maximum concentrations exceeding 4.5 mg·m⁻³ right at the coast. This low-nitrate /**
1074 **high-chlorophyll inverse relationship at the immediate coastline is consistent with the known**
1075 **characteristics of the Angola Current. Indeed, the AC transports 'mature' waters originating from the**
1076 Equatorial Undercurrent (EUC).

1077 We assessed the variability of biological productivity using the PISCES component of our coupled
1078 model (Fig. 18). The results show a clear semi-annual cycle of **Net Primary Production (NPP)**, **New**
1079 **Production (NP)**, and **Regenerated Production (RP)**, which is consistent with the seasonal cycle of
1080 nitrate and CHLa concentrations observed in the region (Körner et al., 2024). The highest values of **NPP**
1081 (Fig. 18a) are found near the Congo River mouth (between 5.5°S and 6°S), where average values exceed
1082 **0.20 mol N·m⁻²·d⁻¹**. During the main upwelling period (June–August), the **NPP** reaches its maximum,
1083 with local peaks near 6°S exceeding **0.25 mol N·m⁻²·d⁻¹**. This intensity is comparable to, though slightly
1084 lower than, the average primary production reported for the Benguela and Humboldt systems, which
1085 reach **0.37** and **0.33 mol N·m⁻²·d⁻¹** respectively (converted from Tilstone et al., 2009; Monteiro et al.,
1086 2010).

1087 The secondary upwelling period in December also shows high productivity, with **NPP** values reaching
1088 approximately **0.22 mol N·m⁻²·d⁻¹** near the river mouth. In contrast, during the downwelling periods
1089 (notably in March and October), the system becomes less productive, with **NPP** dropping below **0.075**
1090 **mol N·m⁻²·d⁻¹** in most of the coastal box. The analysis of production components reveals that during the
1091 main upwelling season, the **New Production (NP)** (Fig. 18b) peaks at around **0.15 mol N·m⁻²·d⁻¹**,
1092 representing about 50–60% of the **NPP**. In December, the **NP** contribution is lower, around **0.10 mol**
1093 **N·m⁻²·d⁻¹**. The **Regenerated Production (RP)** (Fig. 18c) remains a significant and stable driver of
1094 productivity throughout the year, particularly near the Congo mouth where it often exceeds **0.125 mol**
1095 **N·m⁻²·d⁻¹**, highlighting the importance of nutrient recycling in this river-influenced system.

1096 We assessed the variability of biological productivity using the PISCES component of our coupled
 1097 model (Fig.18), and the results are similar to the semi-annual cycle of nitrate and CHLa concentration in
 1098 the TAUS (Korner et al., 2024). The highest values of total primary production (TPP) are observed near
 1099 the mouth of the Congo River (between 5-6°S), with more than 0.20 molN.m⁻².d⁻¹ on average. The
 1100 maximum value of NPP occurs during the main upwelling period, with 0.60 molC.m⁻².d⁻¹, which is
 1101 almost four times less than the average primary production in the Benguela and Humbolt upwelling
 1102 systems (2.49 and 2.18 molC.m⁻².d⁻¹ respectively) and three times less than that in the Canary Islands
 1103 upwelling system (Monteiro et al., 2010). In the secondary upwelling period, NPP reaches around 0.26
 1104 molN.m⁻².d⁻¹, which is more than twice lower than in the main upwelling period. In the downwelling
 1105 period, the net primary production is less than 0.20 molN.m⁻².d⁻¹, whereas in the main upwelling period,
 1106 the new production is estimated at around 0.30 molN.m⁻².d⁻¹, which represents around 50% of the net
 1107 **primary production. During the secondary upwelling period, this new production contributes**
 1108 **around 26% of the net primary production with 0.07 molN.m⁻².d⁻¹.**



1109
 1110 **Figure 178: Latitude-Time Hovmöller diagram of biological productivity: Net Primary Production (a), New**
 1111 **Production (b) and regenerated Production (c) in the coastal box (6°S-3°S, 1° wide along the coastline). The**
 1112 **units are milli mol per cubic meter per day.**

1113 High values of **Net Primary Production (NPP)** are also observed around 4.47°S, near the mouth of the
 1114 Kouilou River, following the characteristic semi-annual cycle of the region. A detailed comparison of
 1115 the production components (Fig. 18b, c) reveals that **Regenerated Production (RP)**, fueled by the
 1116 recycling of nutrients within the euphotic layer, is generally higher than **New Production (NP)**. These
 1117 two parameters remain consistent with the seasonal cycle of nitrate concentrations described previously.
 1118 The seasonal cycle of **NPP** in the Congolese system differs from those of the Namibia and Benguela
 1119 upwellings, which are primarily wind-forced systems (Gutknecht et al., 2013). A key distinction lies in
 1120 the efficiency of nitrate utilization: in our study area, the contribution of **New Production** to the total

1121 NPP is notably high. For instance, while the *f-ratio* (NP/NPP) in the Benguela system typically ranges
1122 between 0.2 and 0.4 (Monteiro et al., 2010), it reaches approximately 0.6 in the Congolese coastal box,
1123 indicating that more than half of the primary production is sustained by the upward supply of new
1124 nitrates.

1125 ~~We also have the highest values of TPP (Net primary production) at 4.47°S (mouth of the Kouilou), in~~
1126 ~~line with the semi-annual cycle. We can also see that regenerated primary production (fig.18c) (the~~
1127 ~~difference between Net TPP and NP), due to recycling of nitrate in the euphotic layer, appears to be~~
1128 ~~greater than new production due to nitrate from outside the euphotic layer. The above two parameters are~~
1129 ~~consistent with the seasonal cycle of nitrate concentration. Net primary production in our study area has~~
1130 ~~a different seasonal cycle than in Namibia and Benguela, as these are wind forced upwelling areas~~
1131 ~~(Gutknecht, 2013), unlike our study area. Another important observation is that the contribution of new~~
1132 ~~production to net primary production in our area is larger than in wind upwelling systems. For~~
1133 ~~example, in the Benguela upwelling new production contributes about 30% of net primary~~
1134 ~~production, with the f-Ratio between 0.2 and 0.4 (Monteiro et al., 2010), whereas it is about 0.6 in~~
1135 ~~our study area.~~

1136 Finally, we demonstrate that the conclusions regarding the nitrate budget are highly sensitive to the
1137 definition of the Mixed Layer Depth (MLD). In this study, we adopted a **3 m reference depth** for the
1138 MLD calculation, following the criterion proposed by Aroucha et al. (2025). This shallower definition is
1139 more appropriate for the Congolese system, as it accurately captures the intense surface stratification
1140 induced by the river's freshwater plume. With this refined MLD criterion, our results show a significant
1141 shift in the balance of vertical processes: **vertical diffusion (mixing)** now emerges as the dominant
1142 mechanism supplying nitrate to the mixed layer, outweighing the contribution of vertical advection. This
1143 finding aligns with recent observations in the Angolan upwelling (Brandt et al., 2023; Körner et al.,
1144 2023, 2024) and the Congolese plume region (Scannell and McPhaden, 2018; Ngakala et al., 2025),
1145 which highlight turbulent mixing—often fueled by internal tides and shear—as a major driver of vertical
1146 nutrient and heat fluxes. This shift emphasizes the critical role of the 'Barrier Layer' and the strong
1147 surface halocline in trapping nutrients and modulating their upward transfer through small-scale mixing
1148 processes rather than mean vertical motion.

1149 ~~We also note that conclusions about the nitrate budget in the mixed layer can vary depending on the~~
1150 ~~definition of the mixed layer, particularly when we look at the main process driving nitrate input to the~~
1151 ~~mixed layer. As mentioned earlier in this study, the main driving process of nitrate input to the mixed~~
1152 ~~layer is vertical advection when we take a mixed layer close to 10 m depth (de Boyer Montégut criteria).~~
1153 ~~But in the Angolan upwelling system, several recent studies (Zang et al., 2023, Körner et al., 2023,2024,~~
1154 ~~Brandt et al., 2023) mention that due to vertical mixing induced by the internal tides, turbulent mixing is~~
1155 ~~the main driver of coastal cooling in this zone and that this conclusion is probably the same in the~~
1156 ~~Congolese coastal zone. Thus, in our analysis, if we consider a very shallow mixed layer using the same~~
1157 ~~definition of mixed layer as Ngakala et al. (2025) and Scannel and Mc Phaden (2018) in the Congolese~~

1158 | ~~zone, we arrive at the same conclusion as previously found in the Angolan coastal zone (Zang et al.,~~
1159 | ~~2023, Körner et al., 2023, 2024, Brandt et al., 2023) with the dominance of vertical diffusion in the~~
1160 | ~~nitrate budget.~~

1161 |

1162 | **5 Conclusion**

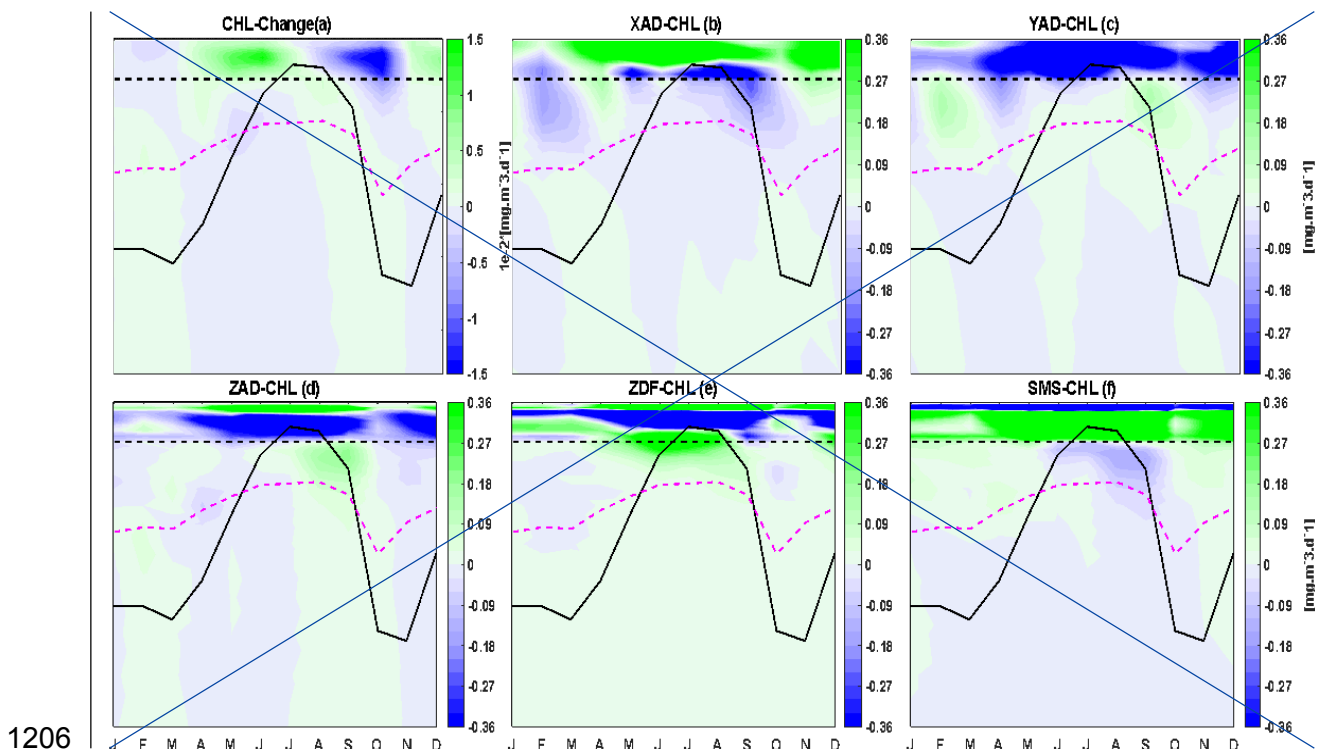
1163 | **Throughout this work we have described and analysed the seasonal cycles in nitrate and CHLa**
1164 | **concentrations, as well as the physical and biological processes that modulate nitrate supply and**
1165 | **biological productivity in the mixed layer and in the euphotic layer in the Congolese upwelling**
1166 | **system. We began by validating a regional high-resolution (1/36°) simulation of the coupled**
1167 | **physical-biogeochemical model NEMO-PISCES in this area for the studied year 2011. Surface and**
1168 | **subsurface validation of the simulation using observations (satellite, in situ, climatology) shows**
1169 | **that the model reasonably reproduces the main physical and biogeochemical characteristics of the**
1170 | **study area. Subsequently, the seasonal cycle of nitrate shows that there are two periods of upwelling and**
1171 | **two periods of downwelling (Fig. 4e,f and Fig. 11a)**~~Subsequently, the seasonal cycle of nitrate shows~~
1172 | ~~that there are two periods of upwelling (May–August and December) and two periods of downwelling~~
1173 | ~~(January–April and October–November). These upwelling and downwelling are associated with~~
1174 | ~~remote forcing : Kelvin waves that propagate along the equator and the coastal waveguide force~~
1175 | ~~the vertical migrations of the thermocline, which is also a proxy for the nitracline. The seasonal~~
1176 | ~~cycle of CHLa is explained by that of nitrate. The assessment of the nitrate balance in the mixed~~
1177 | ~~layer shows that the main nitrate is mainly supplied in the mixed layer by vertical diffusion (Fig.~~
1178 | ~~10f), vertical advection (Fig. 10d) and zonal advection (Fig. 10c), which is mainly modulated by~~
1179 | ~~nitrate inputs from the Congo River at 6°S. The vertical advection induced by CTWs and vertical~~
1180 | ~~diffusion play also a role in the nitrate supply, while nitrate losses are linked to meridional~~
1181 | ~~advection and the biological activity (photosynthesis). In the lower part of the euphotic layer, on~~
1182 | ~~the other hand, nitrate is supplied by zonal advection and vertical advection. Vertical diffusion~~
1183 | ~~contributes to nitrate losses, except in downwelling periods where it represents one of the main~~
1184 | ~~drivers of nitrate supply. We have also seen that meridional advection via the Angola Current,~~
1185 | ~~which transports the low-nitrate warm waters of the Equatorial undercurrent, is the main driver~~
1186 | ~~of nitrate loss below the mixed layer throughout the year. We find that vertical advection is~~
1187 | ~~controlled by the vertical nitrate gradient and nitrate input(Fig. 15), rather than vertical velocity,~~
1188 | ~~when it brings nitrate into the mixed layer during the main upwelling period. However, in the~~
1189 | ~~secondary upwelling in December, vertical advection also brings nitrate, but is then mostly~~
1190 | ~~controlled by vertical velocity.~~

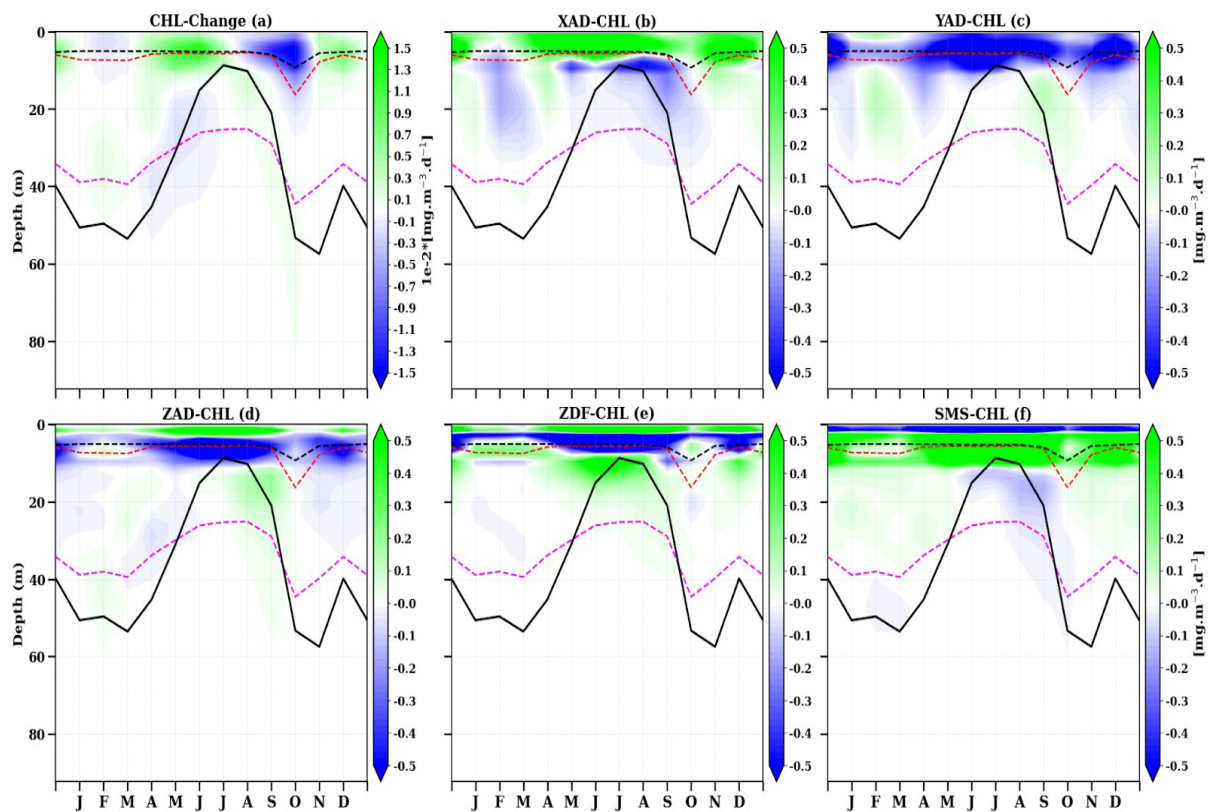
1191 | **In future works, the interannual variability will be study especially associated with the**
1192 | **interannual variability of the Congo river discharges (Scannell and McPhaden (2018), Körner et**
1193 | **al., 2023, 2024; Brandt et al., 2023) and of the CTWs forced by the Equatorial Kelvin waves (e.g.**
1194 | **Bachèlery et al., 2015, 2016). Understanding the seasonal and interannual variability of**

1195 productivity is of primary interest to ensure the sustainability of ecosystems and fisheries in the
1196 Congolese upwelling system.

1197 Appendix A : Euphotic Layer CHLa Budget Analysis

1198 In the lower part of the euphotic zone, the CHLa budget (Fig. A1) is primarily governed by the
1199 interaction between coastal and offshore water masses. During the downwelling period, the zonal
1200 advection term (XAD_CHL) shows a net loss of CHLa near the base of the euphotic layer. This is
1201 explained by the passage of the South Equatorial Undercurrent (SEUC). As described by Nubi et al.
1202 (2016), undercurrent waters (EUC/SEUC) are relatively nitrate-poor and carry less CHLa than the highly
1203 productive coastal waters. The eastward transport of these offshore waters towards the Congolese coast
1204 leads to a dilution of the local CHLa concentration, a process captured by the negative values in the zonal
1205 advection budget.





1208

1209

1210

1211

1212

1213

1214

1215

1216

1217

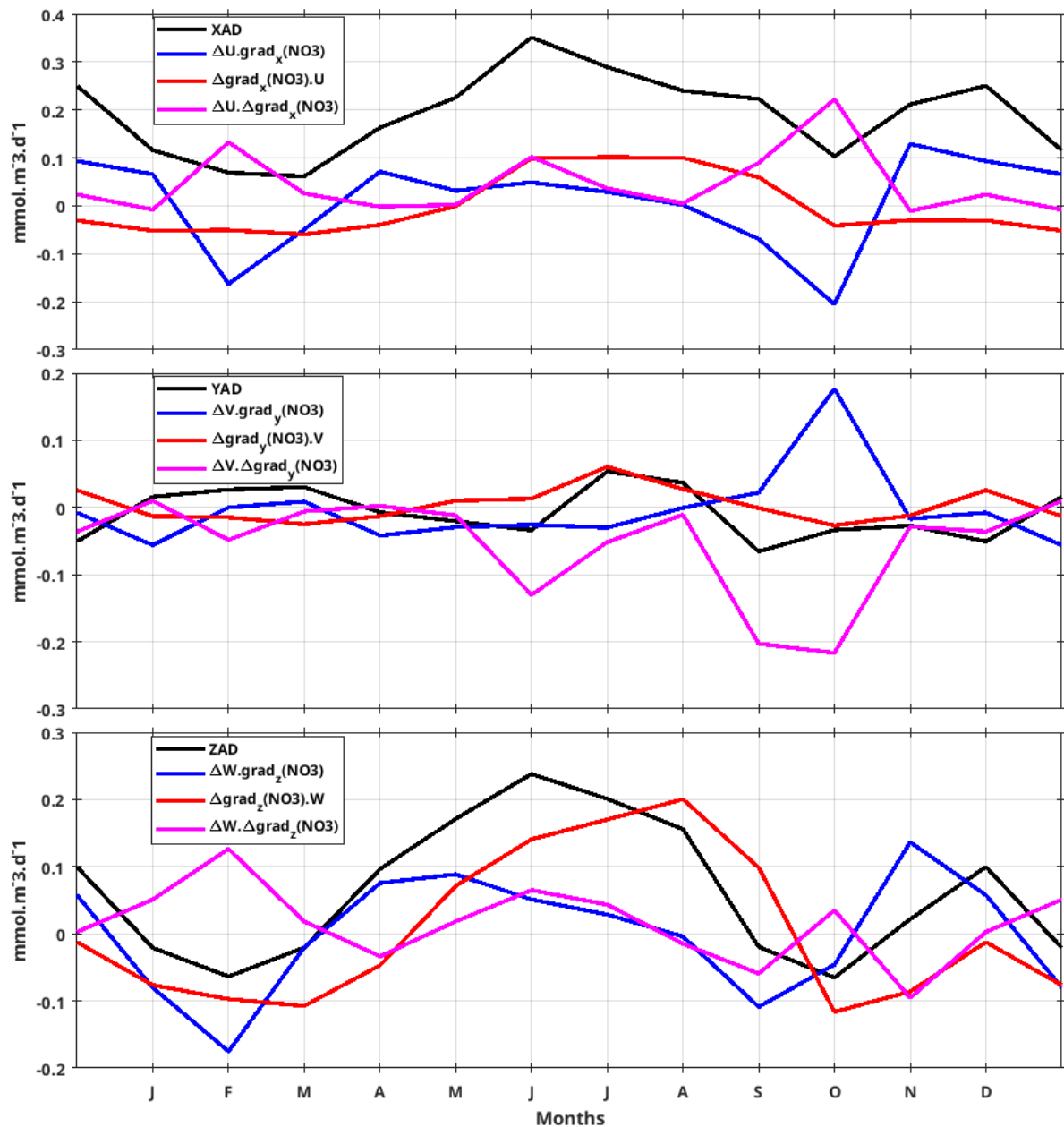
1218

Figure A1: Depth-time Hovmöller diagram of the seasonal chlorophyll-a budget along the Congolese coast (6°S–0°N, 1° coastal strip) for: (a) total rate of change (CHL-change), (b) zonal advection (XAD-CHL), (c) meridional advection (YAD-CHL), (d) vertical advection (ZAD-CHL), (e) vertical diffusion (ZDF-CHL), and (f) biological source-minus-sink term (SMS-CHL). Units for all panels are $\text{mg m}^{-3} \text{d}^{-1}$. The black solid line represents the thermocline (20°C isotherm), while dashed magenta, red and black lines indicate the euphotic, isothermal and mixed layer depths, respectively.

1219

Appendix B : Euphotic Layer Nitrate Advections Components Analysis

1220



1221

1222 **Figure B1: Seasonal variation of advection components averaged in the euphotic layer, black line represent**
 1223 **zonal, meridional and vertical advection in (a), (b) and (c) respectively. The red line in both three figures**
 1224 **represents gradient variation, blue line is current variation and magenta line represents the simultaneous**
 1225 **variation of gradient and current.**

1226

1227 **Code and data availability. Publicly available datasets were used for this study. Chlorophyll data**
 1228 **(1998–2020) are from the Copernicus-GlobColour dataset (<https://doi.org/10.48670/moi-00281>,**
 1229 **Copernicus, 2023a). The sea level anomaly data (1998–2020) were accessed via the Copernicus**
 1230 **Server (<https://doi.org/10.48670/moi-00148>, Copernicus, 2023b). The MUR SST product created**
 1231 **by the JPL MUR MEaSURES program as part of the GHRSSST (Group for High-Resolution Sea**
 1232 **Surface Temperature) project is obtained from**

1233 [L4-GLOB-v4.1](#) (Chin et al., 2017) and ASCAT wind data
1234 <https://podaac.jpl.nasa.gov/dataset/ASCATB-L2-25km>. The nutrient fields were assessed using
1235 the CSIRO Atlas of Regional Seas climatology (Dunn and Ridgway, 2002) ,
1236 [https://thredds.aodn.org.au/thredds/catalog/CSIRO/Climatology/CARS/2009/AODN-product/
1237 catalog.html?dataset=CSIRO/Climatology/CARS/2009/AODN-product/](https://thredds.aodn.org.au/thredds/catalog/CSIRO/Climatology/CARS/2009/AODN-product/catalog.html?dataset=CSIRO/Climatology/CARS/2009/AODN-product/). Near surface currents
1238 from the Ocean Surface Current Analysis Real-time (OSCAR, Johnson et al. 2007),
1239 https://podaac.jpl.nasa.gov/dataset/OSCAR_L4_OC_INTERIM_V2.0. Model outputs are
1240 available from the authors, especially GA, ID, GM, and JJ.

1241
1242 **Author contributions.** LJME outlined and wrote the paper. LJME and RDG produced the figures.
1243 GM has run the NEMO-PISCES model. GA, ID, CYD the co-authors contributed to define
1244 methodology and reviewed the paper.

1245 **Conflict of Interest.** The authors declare that they have no conflict of interest.

1246 **Acknowledgments.** Research is sponsored by the CNES SWOT-ETAO project (Surface Water
1247 and Ocean Topography, Study of Ocean Topography and Altimetry by the National Centre for
1248 Space Studies France). GENCI GEN7298 project (National High-Performance Computing
1249 Equipment) for computing hours for simulations.

1250 **Thanks go to** (<https://www.esr.org/research/oscar/oscar-surface-currents/>) to provide OSCAR
1251 current data.

1252 **Also thanks to** <https://podaac.jpl.nasa.gov/> for providing MUR SST data.

1253 **Financial Support.** This project is funded by IRD-ARTS (Research Grant for a Thesis in the South
1254 provided by Institute of Research for Development France) for my Phd scholarship.

1255 **References**

1256
1257 [Assene, F., Morel, Y., Delpech, A., Aguedjou, M., Jouanno, J., Cravatte, S., Marin, F., Ménesguen, C.,
1258 Chaigneau, A., Dadou, I., Alory, G., Holmes, R., Bourlès, B., & Koch-larrouy, A. \(2020\). **From Mixing
1259 to the Large Scale Circulation : How the Inverse Cascade Is Involved in the Formation of the
1260 Subsurface Currents in the Gulf of Guinea.** 1-36. <https://doi.org/10.3390/fluids5030147>.](#)

1261 [Aumont, O. and Bopp, L.: Globalizing results from ocean insitu iron fertilization experiments,
1262 *Global Biogeochem. Cy.*, 20, GB2017, <https://doi.org/10.1029/2005GB002591>, 2006.](#)

1263 [Aumont, O., Belviso, S., and Monfray, P.: Dimethylsulfide \(DMS\) cycle with a 3-D ocean-
1264 biogeochemical model, *Oceanogr. Lit. Rev.*, 11, 1637, <https://doi.org/10.1029/98GB02757>, 1998.](#)

1265 [Aumont, O., Ethé, C., Tagliabue, A., Bopp, L., and Gehlen, M.: PISCES-v2: an ocean
1266 biogeochemical model for carbon and ecosystem studies, *Geosci. Model Dev.*, 8, 2465–2513,
1267 <https://doi.org/10.5194/gmd-8-2465-2015>.](#)

- 1268 | [Awo, F. M., Alory, G., Da-Allada, C. Y., Delcroix, T., Jouanno, J., Kestenare, E., and Baloitcha, E.: On](#)
1269 | [the seasonal and interannual variability of the sea surface salinity in the Gulf of Guinea, *Clim. Dynam.*,](#)
1270 | [60, 2121–2140, <https://doi.org/10.1007/s00382-022-06443-4>, 2023.](#)
- 1271 | [Awo, F. M., Rouault, M., Ostrowski, M., Tomety, F. S., Da-Allada, C. Y., and Jouanno, J.: Seasonal](#)
1272 | [cycle of sea surface salinity in the Angola Upwelling System, *J. Geophys. Res.-Oceans*, 127,](#)
1273 | [e2022JC018518, <https://doi.org/10.1029/2022JC018518>, 2022.](#)
- 1274 | [Bachèlery, M. L. \(2016\). **Variabilité côtière physique et biogéochimique en Atlantique Sud-Est:**](#)
1275 | [**rôle du forçage atmosphérique local versus téléconnexion océanique \(Doctoral dissertation, Ph. D.**](#)
1276 | [**thesis, Toulouse: Laboratoire d'Etude en Géophysique et Océanographie Spatiale \(LEGOS\),**](#)
1277 | [**University of Paul Sabatier, 215\).**](#)
- 1278 | [Bachèlery, M.-L., Illig, S., and Dadou, I.: Interannual variability in the South-East Atlantic Ocean,](#)
1279 | [focusing on the Benguela Upwelling System: Remote versus local forcing, *J. Geophys. Res. Oceans*,](#)
1280 | [121, 284–310, <https://doi.org/10.1002/2015JC011168>, 2015.](#)
- 1281 | [Bourlès, B., Molinari, R. L., Johns, W. E., Gouriou, Y., and Carder, K. L.: The South Equatorial](#)
1282 | [Undercurrent in the Atlantic Ocean, *Geophys. Res. Lett.*, 31, L14301,](#)
1283 | [<https://doi.org/10.1029/2004GL020020>, 2004.](#)
- 1284 | [Brandt, P., Alory, G., Awo, F. M., Dengler, M., Djakouré, S., Imbol Koungue, R. A., Jouanno, J.,](#)
1285 | [Körner, M., Roch, M., and Rouault, M. \(2023\). **Physical processes and biological productivity in**](#)
1286 | [**the upwelling regions of the tropical Atlantic. *Ocean Science*, 19\(3\):581–601,**](#)
1287 | [<https://doi.org/10.5194/os-19-581-2023>](#)
- 1288 | [Caniaux, G., Giordani, H., Redelsperger, J. L., Guichard, F., Key, E., and Wade, M.: Coupling between](#)
1289 | [the Atlantic cold tongue and the West African monsoon in boreal spring and summer, *J. Geophys. Res.-*](#)
1290 | [*Oceans*, 116, C04003, <https://doi.org/10.1029/2010jc006570>, 2011.](#)
- 1291 | [Carr, M.-E. \(2002\). **Estimation of potential productivity in Eastern Boundary Currents using**](#)
1292 | [**remote sensing. *Deep Sea Research Part II: Topical Studies in Oceanography*, 49\(1–3\):59–80.**](#)
- 1293 | [Chavez, F. P., & Messié, M. \(2009\). A comparison of eastern boundary upwelling ecosystems. *Progress*](#)
1294 | [in *Oceanography*, 83\(1-4\), 80-96.](#)
- 1295 | [Chin, T.M, J Vazquez-Cuervo et E Armstrong \(2017\). “A multi-scale high-resolution analysis of](#)
1296 | [global sea surface temperature”. In : *Remote sensing of environment* 200, p. 154-169.](#)
- 1297 | [de Boyer Montégut, C., Madec, G., Fischer, A. S., Lazar, A., and Iudicone, D.: Mixed layer depth over](#)
1298 | [the global ocean: An examination of profile data and a profile-based climatology, *J. Geophys. Res.*](#)
1299 | [*Oceans*, 109, C12003, <https://doi.org/10.1029/2004JC002378>, 2004.](#)
- 1300 | [Dorothee Bonhoure, Elizabeth Rowe, Arthur J. Mariano, Edward H. Ryan. "The South Equatorial](#)
1301 | [Sys Current." *Ocean Surface Currents*.\(2004\). \[https://oceancurrents.rsmas.miami.edu/atlantic/south-\]\(https://oceancurrents.rsmas.miami.edu/atlantic/south-equatorial.html\)](#)
1302 | [equatorial.html](#)
- 1303 | [Dossa, A., Da-Allada, C., Herbert, G., & Bourlès, B. \(2019\). **Seasonal cycle of the salinity barrier**](#)
1304 | [**layer revealed in the northeastern Gulf of Guinea. *African Journal of Marine Science*, 41\(2\), 163–**](#)
1305 | [**175. <https://doi.org/10.2989/1814232X.2019.1616612>**](#)
- 1306 | [Ducet, N., Le Traon, P.-Y., & Reverdun, G. \(2000\). **Global high-resolution mapping of ocean**](#)
1307 | [**circulation from TOPEX/Poseidon and ERS-1 and -2. *Journal of Geophysical Research*,**](#)
1308 | [**105\(C819\), 19477–19498. <https://doi.org/10.1029/2000jc900063>**](#)

- 1309 | [Dunn, J. R. and Ridgway, K. R.: Mapping ocean properties in regions of complex topography, *Deep Sea*](#)
1310 | [Res. *Part I*, 49, 591–604, \[https://doi.org/10.1016/S0967-0637\\(01\\)00069-3\]\(https://doi.org/10.1016/S0967-0637\(01\)00069-3\), 2002.](#)
- 1311 | [Estival, R., Quiniou, V., Messenger, C., 2013. Real-time network of weather and ocean stations: public-](#)
1312 | [private partnership on in-situ measurements in the Gulf of Guinea. *Sea Technol.* 54 \(3\), 34–38.](#)
- 1313 | [FAO: Fishery and Aquaculture Country Profiles, Angola, 2020, Country Profile Fact Sheets,](#)
1314 | [Fisheries and Aquaculture Division \[online\], Rome, \[https://www.fao.org/fishery/en/facp/ago?\]\(https://www.fao.org/fishery/en/facp/ago?lang=en\)](#)
1315 | [lang= en \(last access: 11 April 2023\), updated 7 February 2022.](#)
- 1316 | [Fréon, P., Barange, M., & Arístegui, J. \(2009\). Eastern boundary upwelling ecosystems: integrative](#)
1317 | [and comparative approaches. *Progress in Oceanography*, 83\(1-4\), 1-14.](#)
- 1318 | [Gutknecht, E., Dadou, I., Marchesiello, P., Cambon, G., Le Vu, B., Sudre, J., Garçon, V., Machu, E.,](#)
1319 | [Rixen, T., Kock, A., Flohr, A., Paulmier, A., and Lavik, G. \(2013\). Nitrogen transfers off Walvis Bay:](#)
1320 | [a 3-D coupled physical/biogeochemical modeling approach in the Namibian upwelling system.](#)
1321 | [*Biogeosciences*, 10\(6\):4117–4135.](#)
- 1322 | [Hardman-Mountford, N. J. and McGlade, J. S.: Retrieval of phytoplankton biomass from ocean colour in](#)
1323 | [the Benguela ecosystem, *Remote Sens. Environ.*, 79, 11–23, <https://doi.org/10.1016/S0034->](#)
1324 | [4257\(01\)00236-0, 2002.](#)
- 1325 | [Hopkins, J., Lucas, M., Dufau, C., Sutton, M., Stum, J., Lauret, O., & Channelliere, C. \(2013\).](#)
1326 | [Detection and variability of the Congo River plume from satellite derived sea surface temperature,](#)
1327 | [salinity, ocean colour and sea level. *Remote Sensing of Environment*, 139, 365–385.](#)
1328 | [https://doi.org/10.1016/j.rse.2013.08.015](#)
- 1329 | [Hutchings, L., van der Lingen, C. D., Shannon, L. J., Crawford, R. J. M., Verheye, H. M. S.,](#)
1330 | [Bartholomae, C. H., van der Plas, A. K., Louw, D., Kreiner, A., Ostrowski, M., Fidel, Q., Barlow,](#)
1331 | [R. G., Lamont, T., Coetzee, J., Shillington, F., Veitch, J., Currie, J. C., and Monteiro, P. M. S.: The](#)
1332 | [Benguela Current: An ecosystem of four components, *Prog. Oceanogr.*, 83, 15–32,](#)
1333 | [https://doi.org/10.1016/j.pocean.2009.07.046, 2009.](#)
- 1334 | [Johns, W. E., Brandt, P., Lumpkin, R., Fischer, J., Hormann, V., Pirani, A., Schmid, C., and Bourlès, B.:](#)
1335 | [Variation of upper ocean seasonal and interannual velocity structure in the eastern equatorial Atlantic. *J.*](#)
1336 | [Phys. *Oceanogr.*, 44, 1201–1212, <https://doi.org/10.1175/JPO-D-13-0132.1>, 2014.](#)
- 1337 | [Johnson, E. S., Bonjean, F., Lagerloef, G. S., Gunn, J. T., & Mitchum, G. T. \(2007\). Validation and](#)
1338 | [error analysis of OSCAR sea surface currents. *Journal of Atmospheric and Oceanic Technology*,](#)
1339 | [24\(4\), 688-701.](#)
- 1340 | [Jouanno, J.: Influence de la dynamique de l’Atlantique équatorial sur la variabilité de la langue froide,](#)
1341 | [PhD thesis, Université de Toulouse III, <http://thesesups.ups-tlse.fr/1154/>, 2010.](#)
- 1342 | [Kobayashi, S., Ota, Y., Harada, Y., Ebita, A., Moriya, M., Onoda, H., Onogi, K., Kamiguchi, H.,](#)
1343 | [Kobayashi, C., Endo, H., Miyaoka, K., and Takahashi, K.: The JRA-55 Reanalysis: General](#)
1344 | [specifications and basic characteristics, *J. Meteorol. Soc. Jpn.*, 93, 5–48,](#)
1345 | [https://doi.org/10.2151/jmsj.2015-001, 2015.](#)
- 1346 | [Kopte, R. \(2017\). The Angola Current in a Tropical Seasonal Upwelling System: Seasonal Variability in](#)
1347 | [Response to Remote Equatorial and Local Forcing \(Doctoral dissertation, Christian-Albrechts](#)
1348 | [Universität Kiel\).](#)

- 1349 [Körner, M., Brandt, P., and Dengler, M.: Seasonal cycle of sea surface temperature in the tropical](#)
1350 [Angolan Upwelling System, *Ocean Sci.*, 19, 121–139, <https://doi.org/10.5194/os-19-121-2023>, 2023.](#)
1351 [Körner, M., Brandt, P., and Dengler, M.: Seasonal cycle of sea surface temperature in the tropical](#)
1352 [Angolan upwelling system, *Ocean Sci.*, 19, 121–139, <https://doi.org/10.5194/os-19-121-2023>, 2023.](#)
- 1353 [Körner, M., Brandt, P., Illig, S., Dengler, M., Subramaniam, A., Bachèlery, M. Lou, and](#)
1354 [Krahmann, G.: Coastal trapped waves and tidal mixing control primary production in the](#)
1355 [tropical Angolan upwelling system, *Sci. Adv.*, 10, 29–31, <https://doi.org/10.1126/sciadv.adj6686>,](#)
1356 [2024.](#)
- 1357 [Locarnini, M. M., Mishonov, A. V., Baranova, O. K., Boyer, T. P., Zweng, M. M., Garcia, H. E., ... &](#)
1358 [Smolyar, I. \(2018\). *World ocean atlas 2018, volume 1: Temperature.*](#)
- 1359 [Loukos, H. and Mémerly, L.: Simulation of the nitrate seasonal cycle in the equatorial **Atlantic ocean**](#)
1360 [during 1983 and 1984, *J. Geophys. Res.*, 104, 15549–15573, 1999.](#)
- 1361 [Madec, G. and the NEMO System Team, 2024. *NEMO Ocean Engine Reference Manual*, Zenodo,](#)
1362 <https://doi.org/10.5281/zenodo.1464816>
- 1363 [Messié, M., & Chavez, F. P. \(2015\). Seasonal regulation of primary production in eastern boundary](#)
1364 [upwelling systems. *Progress in Oceanography*, 134, 1-18.](#)
- 1365 [Monteiro, P., Dewitte, B., Scranton, M., Paulmier, A., and Van der Plas, A. \(2011\). The role of open](#)
1366 [ocean boundary forcing on seasonal to decadal-scale variability and long-term change of natural](#)
1367 [shelf hypoxia. *Environmental Research Letters*, \(6\):1–14.](#)
- 1368 [Ngakala, R. D., Alory, G., Da-Allada, C. Y., Dadou, I., Cardot, C., Morvan, G., ... & Baloitcha, E.](#)
1369 [\(2025\). Seasonal mixed layer temperature in the Congolese upwelling system. *Journal of*](#)
1370 [Geophysical Research: Oceans](#), 130(1), e2023JC020528.
- 1371 [Nieto, K., & Mélin, F. \(2017\). Variability of chlorophyll-a concentration in the Gulf of Guinea and](#)
1372 [its relation to physical oceanographic variables. *Progress in oceanography*, 151, 97-115.](#)
- 1373 [Nubi, O., Bourles, B., & Edokpayi, C. \(2016\). On the Nutrient distribution and phytoplankton](#)
1374 [biomass in the Gulf of Guinea equatorial band as inferred from In-situ measurements. *Journal of*](#)
1375 [Oceanography and Marine Science](#), 7(1), 1-11.
- 1376 [Ostrowski, M., da Silva, J. C. B., and Bazik-Sangolay, B.: The response of sound scatterers to El](#)
1377 [Niño- and La Niña-like oceanographic regimes in the southeastern Atlantic, *ICES J. Mar. Sci.*, 66,](#)
1378 [1063–1072, <https://doi.org/10.1093/icesjms/fsp102>, 2009.](#)
- 1379 [Radenac, M.-H., Jouanno, J., Tchamabi, C. C., Awo, M., Bourlès, B., Arnault, S., and Aumont, O.:](#)
1380 [Physical drivers of the nitrate seasonal variability in the Atlantic cold tongue, *Biogeosciences*, 17, 529–](#)
1381 [545, <https://doi.org/10.5194/bg-17-529-2020>, 2020.](#)
- 1382 [Ridgway, K. R., J. R. Dunn, and J. L. Wilkin \(2002\), Ocean interpolation by four-dimensional least](#)
1383 [squares—Application to the waters around Australia, *J. Atmos. Oceanic Technol.*, 19, 1357–1375.](#)
- 1384 [Rouault, M.: Bi-annual intrusion of tropical water in the northern Benguela upwelling, *Geophys.*](#)
1385 [Res. Lett.](#), 39, L12606, <https://doi.org/10.1029/2012gl052099>, 2012.
- 1386 [Scannell, H. A. and McPhaden, M. J.: Seasonal mixed layer temperature balance in the southeastern](#)
1387 [tropical Atlantic, *J. Geophys. Res. Oceans*, 123, 5557–5570, <https://doi.org/10.1029/2018JC014099>,](#)
1388 [2018.](#)

- 1389 | [Schott, F. A., Fischer, J., and Stramma, L.: Transports and pathways of the upper-layer circulation](#)
1390 | [in the western tropical Atlantic, *J. Phys. Oceanogr.*, 28, 1904–1928, \[https://doi.org/10.1175/1520-\]\(https://doi.org/10.1175/1520-0485\(1998\)028<1904:TAPOTU>2.0.CO;2\)](#)
1391 | [0485\(1998\)028<1904:TAPOTU>2.0.CO;2, 1998.](#)
- 1392 | [Siegfried, L., Schmidt, M., Mohrholz, V., Pogrzeba, H., Nardini, P., Böttinger, M., and](#)
1393 | [Scheuermann, G.: The tropical-subtropical coupling in the Southeast Atlantic from the](#)
1394 | [perspective of the northern Benguela upwelling system, *Plos One*, 14, e0210083,](#)
1395 | [https://doi.org/10.1371/journal.pone.0210083, 2019.](#)
- 1396 | [Sikhakolli, R., Sharma, R., Basu, S., Gohil, B. S., Sarkar, A., & Prasad, K. V. S. R. \(2013\). Evaluation of](#)
1397 | [OSCAR ocean surface current product in the tropical Indian Ocean using in situ data. *Journal of earth*](#)
1398 | [system science, 122\(1\), 187-199](#)
- 1399 | [Sowman, M. and Cardoso, P.: Small-scale fisheries and food security strategies in countries in the](#)
1400 | [Benguela Current Large Marine Ecosystem \(BCLME\) region: Angola, Namibia and South Africa, *Mar.*](#)
1401 | [Policy, 34, 1163–1170, <https://doi.org/10.1016/j.marpol.2010.03.016>, 2010.](#)
- 1402 | [Tchupalanga, P., Dengler, M., Brandt, P., Kopte, R., Macueria, M., Coelho, P., Ostrowski, M., and](#)
1403 | [Keenlyside, N. S.: Eastern Boundary Circulation and Hydrography Off Angola: Building Angolan](#)
1404 | [Oceanographic Capacities, *B. Am. Meteorol. Soc.*, 99, 1589– 1605, \[https://doi.org/10.1175/Bams-\]\(https://doi.org/10.1175/Bams-D-17-0197.1\)](#)
1405 | [D-17-0197.1, 2018a.](#)
- 1406 | [Thiam, A., Alory, G., Jouanno, J., Da-Allada, C. Y., and Morvan, G.: Coastal upwelling in the Northern](#)
1407 | [Gulf of Guinea: Seasonal cycle and mesoscale interactions, *Ocean Modelling*, 188, 102300,](#)
1408 | [https://doi.org/10.1016/j.ocemod.2024.102300, 2024.](#)
- 1409 | [Tilstone, G., Smyth, T., Poulton, A., and Hutson, R. \(2009\). Measured and remotely sensed estimates of](#)
1410 | [primary production in the Atlantic Ocean from 1998 to 2005. *Deep Sea Research Part II: Topical Studies*](#)
1411 | [in Oceanography, 56\(15\):918–930.](#)
- 1412 | [Topé, G. D. A., Alory, G., Djakouré, S., Da-Allada, C. Y., Jouanno, J., & Morvan, G. \(2023\). How](#)
1413 | [does the Niger River warm coastal waters in the Northern Gulf of Guinea? *Frontiers in Marine Science*,](#)
1414 | [10, 1187202. <https://doi.org/10.3389/fmars.2023.1187202>.](#)
- 1415 | [Tuchen, F. P., Brandt, P., Lübbecke, J. F., and Hummels, R.: Transports and pathways of the tropical](#)
1416 | [AMOC return flow from Argo data and shipboard velocity measurements, *J. Geophys. Res.-Oceans*,](#)
1417 | [127, e2021JC018115, <https://doi.org/10.1029/2021JC018115>, 2022a.](#)
- 1418 | [Xu, Z., M. Li, C. M. Patricola, and P. Chang, 2014: Oceanic origin of southeast tropical Atlantic](#)
1419 | [biases. *Climate Dyn.*, 43, 2915–2930, <https://doi.org/10.1007/s00382-013-1901-y>.](#)
- 1420 | [Zeng, Z., Brandt, P., Lamb, K. G., Greatbatch, R. J., Dengler, M., Claus, M., and Chen, X.: Three-](#)
1421 | [dimensional numerical simulations of internal tides in the Angolan upwelling region, *J. Geophys.*](#)
1422 | [Res.-Oceans, 126, e2020JC016460, <https://doi.org/10.1029/2020JC016460>, 2021.](#)
- 1423 | [Zweng, M. M., Seidov, D., Boyer, T. P., Locarnini, M., Garcia, H. E., Mishonov, A. V., ... & Smolyar,](#)
1424 | [I. \(2019\). *World ocean atlas 2018, volume 2: Salinity*.](#)
- 1425 | [Assene, F., Morel, Y., Delpech, A., Aguedjou, M., Jouanno, J., Cravatte, S., Marin, F., Ménesguen,](#)
1426 | [C., Chaigneau, A., Dadou, I., Alory, G., Holmes, R., Bourlès, B., & Koch-Iarrouy, A. \(2020\). From](#)
1427 | [Mixing to the Large Scale Circulation : How the Inverse Cascade Is Involved in the Formation of](#)
1428 | [the Subsurface Currents in the Gulf of Guinea. 1-36. <https://doi.org/10.3390/fluids5030147>.](#)
- 1429 | [Aumont, O. and Bopp, L.: Globalizing results from ocean insitu iron fertilization experiments,](#)
1430 | [*Global Biogeochem. Cy.*, 20, GB2017, <https://doi.org/10.1029/2005GB002591>, 2006.](#)

- 1431 | Aumont, O., Ethé, C., Tagliabue, A., Bopp, L., and Gehlen, M.: PISCES-v2: an ocean
1432 | biogeochemical model for carbon and ecosystem studies, *Geosci. Model Dev.*, 8, 2465–2513,
1433 | <https://doi.org/10.5194/gmd-8-2465-2015>, 2015.
- 1434 | Awo, F. M., Rouault, M., Ostrowski, M., Tomety, F. S., Da-Allada, C. Y., and Jouanno, J.:
1435 | Seasonal cycle of sea surface salinity in the Angola Upwelling System, *J. Geophys. Res.-Oceans*,
1436 | 127, e2022JC018518, <https://doi.org/10.1029/2022JC018518>, 2022.
- 1437 | ~~Bachèlery, M. L. (2016). Variabilité côtière physique et biogéochimique en Atlantique Sud-Est: rôle du~~
1438 | ~~forçage atmosphérique local versus téléconnexion océanique (Doctoral dissertation, Ph. D. thesis,~~
1439 | ~~Toulouse: Laboratoire d'Etude en Géophysique et Océanographie Spatiale (LEGOS), University of Paul~~
1440 | ~~Sabatier, 215).~~
- 1441 | Brandt, P., Alory, G., Awo, F. M., Dengler, M., Djakouré, S., Imbol Koungue, R. A., Jouanno, J.,
1442 | Körner, M., Roch, M., and Rouault, M. (2023). Physical processes and biological productivity in
1443 | the upwelling regions of the tropical Atlantic. *Ocean Science*, 19(3):581–601,
1444 | <https://doi.org/10.5194/os-19-581-2023>
- 1445 | Caniaux, G., Giordani, H., Redelsperger, J. L., Guichard, F., Key, E., and Wade, M.: Coupling
1446 | between the Atlantic cold tongue and the West African monsoon in boreal spring and summer, *J.*
1447 | *Geophys. Res.-Oceans*, 116, C04003, <https://doi.org/10.1029/2010jc006570>, 2011.
- 1448 | Carr, M.-E. (2002). Estimation of potential productivity in Eastern Boundary Currents using
1449 | remote sensing. *Deep Sea Research Part II: Topical Studies in Oceanography*, 49(1–3):59–80.
- 1450 | Chavez, F. P., & Messié, M. (2009). A comparison of eastern boundary upwelling ecosystems.
1451 | *Progress in Oceanography*, 83(1-4), 80-96.
- 1452 | Chin, T.M, J Vazquez-Cuervo et E Armstrong (2017). “A multi-scale high-resolution analysis of
1453 | global sea surface temperature”. In : Remote sensing of environment 200, p. 154-169.
- 1454 | De Boyer Montégut, C., Mignot, J., Lazar, A., & Cravatte, S. (2007). Control of salinity on the mixed
1455 | layer depth in the world ocean: 1. General description. *Journal of Geophysical Research: Oceans*,
1456 | 112(C6).
- 1457 | Dorothee Bonhoure, Elizabeth Rowe, Arthur J. Mariano, Edward H. Ryan. "The South Equatorial Sys
1458 | Current." *Ocean Surface Currents*.(2004).[https://oceancurrents.rsmas.miami.edu/atlantic/south-](https://oceancurrents.rsmas.miami.edu/atlantic/south-equatorial.html)
1459 | [equatorial.html](https://oceancurrents.rsmas.miami.edu/atlantic/south-equatorial.html)
- 1460 | Dossa, A., Da-Allada, C., Herbert, G., & Bourlès, B. (2019). Seasonal cycle of the salinity barrier
1461 | layer revealed in the northeastern Gulf of Guinea. *African Journal of Marine Science*, 41(2), 163–
1462 | 175. <https://doi.org/10.2989/1814232X.2019.1616612>
- 1463 | Ducet, N., Le Traon, P.-Y., & Reverdun, G. (2000). Global high-resolution mapping of ocean
1464 | circulation from TOPEX/Poseidon and ERS 1 and 2. *Journal of Geophysical Research*,
1465 | 105(C819), 19477–19498. <https://doi.org/10.1029/2000jc900063>
- 1466 | Estival, R., Quiniou, V., Messenger, C., 2013. Real-time network of weather and ocean stations:
1467 | public-private partnership on in-situ measurements in the Gulf of Guinea. *Sea Technol.* 54 (3), 34–
1468 | 38.
- 1469 | FAO: Fishery and Aquaculture Country Profiles, Angola, 2020, Country Profile Fact Sheets,
1470 | Fisheries and Aquaculture Division [online], Rome, [https://www.fao.org/fishery/en/facp/ago?](https://www.fao.org/fishery/en/facp/ago?lang=en)
1471 | [lang=en](https://www.fao.org/fishery/en/facp/ago?lang=en) (last access: 11 April 2023), updated 7 February 2022.
- 1472 | Fréon, P., Barange, M., & Arístegui, J. (2009). Eastern boundary upwelling ecosystems:
1473 | integrative and comparative approaches. *Progress in Oceanography*, 83(1-4), 1-14.

- 1474 | [Gent, P. R. and McWilliams, J. C.: Isopycnal mixing in ocean circulation models, *J. Phys. Oceanogr.*, 20,](#)
1475 | [150–155, 1990.](#)
- 1476 | [Gutknecht, E., Dadou, I., Marchesiello, P., Cambon, G., Le Vu, B., Sudre, J., Garçon, V., Machu, E.,](#)
1477 | [Rixen, T., Koek, A., Flohr, A., Paulmier, A., and Lavik, G. \(2013\). Nitrogen transfers off Walvis Bay:](#)
1478 | [a 3-D coupled physical/biogeochemical modeling approach in the Namibian upwelling system.](#)
1479 | [Biogeosciences, 10\(6\):4117–4135.](#)
- 1480 | [Hopkins, J., Lucas, M., Dufau, C., Sutton, M., Stum, J., Lauret, O., & Channelliere, C. \(2013\).](#)
1481 | [Detection and variability of the Congo River plume from satellite derived sea surface temperature,](#)
1482 | [salinity, ocean colour and sea level. *Remote Sensing of Environment*, 139, 365–385.](#)
1483 | <https://doi.org/10.1016/j.rse.2013.08.015>
- 1484 | [Hutchings, L., van der Lingen, C. D., Shannon, L. J., Crawford, R. J. M., Verheye, H. M. S.,](#)
1485 | [Bartholomae, C. H., van der Plas, A. K., Louw, D., Kreiner, A., Ostrowski, M., Fidel, Q., Barlow,](#)
1486 | [R. G., Lamont, T., Coetzee, J., Shillington, F., Veitch, J., Currie, J. C., and Monteiro, P. M. S.: The](#)
1487 | [Benguela Current: An ecosystem of four components, *Prog. Oceanogr.*, 83, 15–32,](#)
1488 | <https://doi.org/10.1016/j.pocean.2009.07.046>, 2009.
- 1489 | [Johnson, E. S., Bonjean, F., Lagerloef, G. S., Gunn, J. T., & Mitchum, G. T. \(2007\). Validation and](#)
1490 | [error analysis of OSCAR sea surface currents. *Journal of Atmospheric and Oceanic Technology*,](#)
1491 | [24\(4\), 688–701.](#)
- 1492 | [Kopte, R. \(2017\). The Angola Current in a Tropical Seasonal Upwelling System: Seasonal](#)
1493 | [Variability in Response to Remote Equatorial and Local Forcing \(Doctoral dissertation,](#)
1494 | [Christian-Albrechts Universität Kiel\).](#)
- 1495 | [Körner, M., Brandt, P., and Dengler, M.: Seasonal cycle of sea surface temperature in the tropical](#)
1496 | [Angolan Upwelling System, *Ocean Sci.*, 19, 121–139, <https://doi.org/10.5194/os-19-121-2023>, 2023.](#)
- 1497 | [Körner, M., Brandt, P., Illig, S., Dengler, M., Subramaniam, A., Bachelery, M. Lou, and](#)
1498 | [Krahmann, G.: Coastal trapped waves and tidal mixing control primary production in the](#)
1499 | [tropical Angolan upwelling system, *Sci. Adv.*, 10, 29–31, <https://doi.org/10.1126/sciadv.adj6686>,](#)
1500 | [2024.](#)
- 1501 |
- 1502 | [Locarnini, M. M., Mishonov, A. V., Baranova, O. K., Boyer, T. P., Zweng, M. M., Garcia, H. E., ...](#)
1503 | [& Smolyar, I. \(2018\). World ocean atlas 2018, volume 1: Temperature.](#)
- 1504 | [Loukos, H. and Mémery, L.: Simulation of the nitrate seasonal cycle in the equatorial Atlantic](#)
1505 | [ocean during 1983 and 1984, *J. Geophys. Res.*, 104, 15549–15573, 1999.](#)
- 1506 | [Madec, G. and the NEMO System Team, 2024. *NEMO Ocean Engine Reference Manual*, \[Zenodo.\]\(#\)](#)
1507 | <https://doi.org/10.5281/zenodo.1464816>
- 1508 | [Messié, M., & Chavez, F. P. \(2015\). Seasonal regulation of primary production in eastern](#)
1509 | [boundary upwelling systems. *Progress in Oceanography*, 134, 1–18.](#)
- 1510 | [Monod, J.: Recherches sur la Croissance des Cultures Bactériennes, Hermann, Paris, 1942.](#)
- 1511 | [Monteiro, P., Dewitte, B., Scranton, M., Paulmier, A., and Van der Plas, A. \(2011\). The role of open](#)
1512 | [ocean boundary forcing on seasonal to decadal-scale variability and long-term change of natural shelf](#)
1513 | [hypoxia. *Environmental Research Letters*, \(6\):1–14.](#)

- 1514 | ~~Ngakala, R. D., Alory, G., Da-Allada, C. Y., Dadou, I., Cardot, C., Morvan, G., ... & Baloïtcha, E.~~
1515 | ~~(2025). Seasonal mixed layer temperature in the Congolese upwelling system. *Journal of*
1516 | *Geophysical Research: Oceans*, 130(1), e2023JC020528.~~
- 1517 | ~~Nieto, K., & Mélin, F. (2017). Variability of chlorophyll-a concentration in the Gulf of Guinea and~~
1518 | ~~its relation to physical oceanographic variables. *Progress in oceanography*, 151, 97-115.~~
- 1519 | ~~Nubi, O., Bourles, B., & Edokpayi, C. (2016). On the Nutrient distribution and phytoplankton~~
1520 | ~~biomass in the Gulf of Guinea equatorial band as inferred from In-situ measurements. *Journal of*
1521 | *Oceanography and Marine Science*, 7(1), 1-11.~~
- 1522 | ~~Ostrowski, M., da Silva, J. C. B., and Bazik-Sangolay, B.: The response of sound scatterers to El~~
1523 | ~~Niño- and La Niña-like oceanographic regimes in the southeastern Atlantic, *ICES J. Mar. Sci.*, 66,~~
1524 | ~~1063–1072, <https://doi.org/10.1093/icesjms/fsp102>, 2009.~~
- 1525 | ~~Radenac, M.-H., Jouanno, J., Tchamabi, C. C., Awo, M., Bourlès, B., Arnault, S., and Aumont, O.:~~
1526 | ~~Physical drivers of the nitrate seasonal variability in the Atlantic cold tongue, *Biogeosciences*, 17,~~
1527 | ~~529–545, <https://doi.org/10.5194/bg-17-529-2020>, 2020.~~
- 1528 | ~~Ridgway, K. R., J. R. Dunn, and J. L. Wilkin (2002), Ocean interpolation by four-dimensional least~~
1529 | ~~squares—Application to the waters around Australia, *J. Atmos. Oceanic Technol.*, 19, 1357–1375.~~
- 1530 | ~~Rouault, M.: Bi-annual intrusion of tropical water in the northern Benguela upwelling, *Geophys.*
1531 | *Res. Lett.*, 39, L12606, <https://doi.org/10.1029/2012gl052099>, 2012.~~
- 1532 | ~~Schott, F. A., Fischer, J., and Stramma, L.: Transports and pathways of the upper-layer~~
1533 | ~~circulation in the western tropical Atlantic, *J. Phys. Oceanogr.*, 28, 1904–1928,~~
1534 | ~~[https://doi.org/10.1175/1520-0485\(1998\)028<1904:TAPOTU>2.0.CO;2](https://doi.org/10.1175/1520-0485(1998)028<1904:TAPOTU>2.0.CO;2), 1998.~~
- 1535 | ~~Siegfried, L., Schmidt, M., Mohrholz, V., Pogrzeba, H., Nardini, P., Böttinger, M., and~~
1536 | ~~Scheuermann, G.: The tropical-subtropical coupling in the Southeast Atlantic from the~~
1537 | ~~perspective of the northern Benguela upwelling system, *Plos One*, 14, e0210083,~~
1538 | ~~<https://doi.org/10.1371/journal.pone.0210083>, 2019.~~
- 1539 | ~~Sikhakolli, R., Sharma, R., Basu, S., Gohil, B. S., Sarkar, A., & Prasad, K. V. S. R. (2013).~~
1540 | ~~Evaluation of OSCAR ocean surface current product in the tropical Indian Ocean using in situ~~
1541 | ~~data. *Journal of earth system science*, 122(1), 187-199~~
- 1542 | ~~Sowman, M. and Cardoso, P.: Small-scale fisheries and food security strategies in countries in the~~
1543 | ~~Benguela Current Large Marine Ecosystem (BCLME) region: Angola, Namibia and South Africa,~~
1544 | ~~*Mar. Policy*, 34, 1163–1170, <https://doi.org/10.1016/j.marpol.2010.03.016>, 2010.~~
- 1545 | ~~Tchipalanga, P., Dengler, M., Brandt, P., Kopte, R., Macueria, M., Coelho, P., Ostrowski, M., and~~
1546 | ~~Keenlyside, N. S.: Eastern Boundary Circulation and Hydrography Off Angola: Building Angolan~~
1547 | ~~Oceanographic Capacities, *B. Am. Meteorol. Soc.*, 99, 1589– 1605, [https://doi.org/10.1175/Bams-](https://doi.org/10.1175/Bams-D-17-0197.1)
1548 | ~~D-17-0197.1, 2018a.~~~~
- 1549 | ~~Tilstone, G., Smyth, T., Poulton, A., and Hutson, R. (2009). Measured and remotely sensed~~
1550 | ~~estimates of primary production in the Atlantic Ocean from 1998 to 2005. *Deep Sea Research Part*
1551 | *II: Topical Studies in Oceanography*, 56(15):918–930.~~
- 1552 | ~~Topé, G. D. A., Alory, G., Djakouré, S., Da-Allada, C. Y., Jouanno, J., & Morvan, G. (2023). How~~
1553 | ~~does the Niger River warm coastal waters in the Northern Gulf of Guinea? *Frontiers in Marine*
1554 | *Science*, 10, 1187202. <https://doi.org/10.3389/fmars.2023.1187202>.~~

- 1555 | Tuchen, F. P., Brandt, P., Lübbecke, J. F., and Hummels, R.: Transports and pathways of the
1556 | tropical AMOC return flow from Argo data and shipboard velocity measurements, *J. Geophys.*
1557 | *Res.-Oceans*, 127, e2021JC018115, <https://doi.org/10.1029/2021JC018115>, 2022a.
- 1558 | Xu, Z., M. Li, C. M. Patricola, and P. Chang, 2014: Oceanic origin of southeast tropical Atlantic
1559 | biases. *Climate Dyn.*, 43, 2915–2930, <https://doi.org/10.1007/s00382-013-1901-y>.
- 1560 | Zeng, Z., Brandt, P., Lamb, K. G., Greatbatch, R. J., Dengler, M., Claus, M., and Chen, X.: Three-
1561 | dimensional numerical simulations of internal tides in the Angolan upwelling region, *J. Geophys.*
1562 | *Res.-Oceans*, 126, e2020JC016460, <https://doi.org/10.1029/2020JC016460>, 2021.
- 1563 | ~~Zweng, M. M., Seidov, D., Boyer, T. P., Locarnini, M., Garcia, H. E., Mishonov, A. V., ... &
1564 | Smolyar, I. (2019). World ocean atlas 2018, volume 2: Salinity.~~
- 1565 |